CARDIAC REPAIR USING FIBRIN PATCH-BASED ENHANCED DELIVERY OF STEM CELLS AND NOVEL STRATEGIES FOR FAST EXAMINATION OF MYOCARIDAL ENERGETICS IN VIVO USING 31P MAGNETIC RESONANCE SPECTROSCOPY

A DISSERTATION
SUBMITTED TO THE FACULTY OF THE GRADUATE SCHOOL
OF THE UNIVERSITY OF MINNESOTA
BY

QIANG XIONG

IN PARTIAL FULFILLMENT OF THE REQUIREMENTS
FOR THE DEGREE OF
DOCTOR OF PHILOSOPHY

Advisor: JIANYI (JAY) ZHANG

March 2011

ACKNOWLEDGEMENTS

First and foremost, I would like to thank my advisor and mentor, Dr. Jianyi Zhang for his guidance, support and encouragement throughout my Ph.D training. I also would like to express my appreciation from the bottom of my heart to all my committee members, Drs. Wei Chen, Chun Wang, Tommy Vaughan and T. Andrew Taton for their constructive suggestions on my research.

I am very grateful to all my lab colleagues: Qinglu, Pengyuan, Cory, Xiaohong, Lei, Nur, Abdul and Piradeep. I couldn't accomplish my research if without their supports and help.

I also want to thank Dr. Dan Kaufman's group. The collaboration in the stem cell research has been such a joyful experience.

I am very fortunate to be a member of the big CMRR family, where I received countless help and supports from my friends: Djaudat, Ivan, Pierre-Francois, Xiaoping, Jinfeng, Devashish, Denish, Gregor, Peter, etc.

Last but not least, I like to thank my father Xinping Xiong, my mother Xiufang Fan and my wife Wei Zheng, for their love, endless care and sustained encouragement.

It is impossible for me to finish this dissertation without any of these people.

ABSTRACT

The dissertation is related to heart disease in both basic scientific and pre-clinic respects.

Cardiovascular disease is a leading cause of death in the developed countries even with optimal medical treatment. Recently, the emerging stem cell biology has shown great potentials for cardiac repair. Using both large (swine) and small (rodent) animal models with ischemic heart disease, we examined the functional improvement of enhanced delivery of combined human embryonic stem cell-derived endothelial cells and smooth muscle cells via a fibrin 3D porous scaffold biomatrix. The integration of stem cell biology and tissue engineering has resulted in significant improvement of both regional and global left ventricle function as compared to untreated animals, demonstrating a promising therapeutic strategy of using this cell type and the novel mode of delivery.

As a most energy demanding organ, the heart energetic status is tightly associated with the organ's physiological and pathological conditions. Based on the ultra-high-field magnetic resonance imaging/spectroscopy techniques, we developed a noninvasive modality for rapid examination of cardiac energetics in vivo. The new platform will offer unprecedented understanding into the relationship between the cardiac energetic status and the organ's physiological/pathological conditions, and thus it is of great potential in both basic scientific research and clinical diagnosis.

TABLE OF CONTENTS

LIST OF TABLES

LIST OF FIGURES

Chapter 1

INTRODUCTION AND BACKGROUND

1.1 Significance

Intrinsically a lethal disease, cardiovascular disease (CVD) accounted for more death than any other major cause of death in the United States, killed 2400 Americans each day in year 2004 and cost approximately one fourth of the total cost of hospital care in the United States in year 2005. Of about 80.7 million American adults who have at least one type of CVD, 16 million people suffer from coronary heart disease (CHD) and 5.3 million from heart failure (HF) [1].

Considered an irreversible clinical condition, patients with myocardial (MI) and subsequent heart failure (HF) showed only modestly prolonged life even with optimal medical management. Moreover, current therapeutic approaches to end-stage cardiac failure are very limited. Heart transplantation remains the last treatment option with good long-term results, whereas greatly limited by the

shortage of donors as well as immunosuppressive complications [2]. Therefore, it imperative to develop new efficient treatments for ischemic heart disease as well as more powerful tools to understand the mechanism underlying the irreversible negative remodeling upon cardiac damage.

1.2 Overview of Stem Cell Therapy for Cardiac Repair

In the development of CHF, it is known that the quantity of myocardium loss during MI is inversely related to post-MI left ventricular (LV) function and patient prognosis. Although current treatments for CHF, such as coronary care units, reperfusion therapy and medical therapy, all showed significant reduction in morbidity and mortality [3], it is still very difficult to regenerate new viable myocardium and new blood vessels. Recent studies, however, have suggested that stem cell transplantation results in evident myocardial regeneration as well as neo-angiogenesis, thus making it a potential therapy for limiting postinfarction LV remodeling and subsequent CHF.

1.2.1 Stem Cells for Cardiac Repair

Stem cells are defined by their ability of self-renewal, i.e. stem cells can undergo symmetric or asymmetric divisions to give rise to identical stem cells and progenitor cells that continue to differentiate into specific tissue cell phenotypes [4]. Based on this concept, several types of mammalian cells derived from different sources have been shown to fulfill the definition of stem cells (Table 1.1).

Table 1.1 Mammalian stem cells: sources and properties

Stem cell type	Source and Properties
Fertilized oocyte and morula [5]	Day 1~4 up to the 8 cell stadium. Totipotent, i.e. can originate in complete organism when implanted into a uterus
Embryonic stem cells [5]	Inner cell mass of blastocyst Pluripotent, i.e. can develop into any cell type of adult organism, but cannot generate a complete organism after transplantation into a uterus.
Adult stem cells	Most tissues of body Multipotent, i.e. can differentiate into a limited number of cell types.
Induced pluripotent stem (iPS) cells	Artificially derived from a non-pluripotent cell, typically an adult somatic cell Pluripotent.

Among those stem cell types listed in Table 1.1, embryonic stem cells, adult stem cells (including hematopoietic stem cells, mesenchymal stem cells, cardiac stem cells, etc.) and most recently, induced pluripotent stem cells have received most attentions for their therapeutic potential in ischemic heart disease, and will be briefly reviewed individually.

Embryonic Stem (ES) Cells

Embryonic stem (ES) cells are the most versatile stem cells in that they have the ability to undergo an undetermined number of cell doublings and can differentiate into all three embryonic layers [6-8]. Therefore, they hold great promise

for overcoming many diseases by providing a potential source for many slow-slow-growing cell types, for example, the lost cardiomyocytes during MI. ES cells have been derived from mouse and more recently from non-human primates as well as humans [9-11]. It has been shown that when transplanted into post-natal animals, mouse and human ES (hES) cells generate teratomas consisting of different types of tissues, such as neural cells, guts structures, skin, muscles, etc The presence of cells from all three germ layers in these tumors proves their pluripotency, however, it also places great challenges to the applications using cells transplantation in regenerative therapies. Therefore, great efforts have been made to direct specific differentiation as well as to eliminate undifferentiated ES cells before transplantation [13, 14].

A pioneering study of ES cells transplantation into myocardium was performed by Klug et al [15]. A pure culture of cardiomyogenic cells from murine ES cells was generated in vitro, and subsequently transplanted into the myocardium of dystrophic mice. The transplanted cells integrated and survived in the myocardium for 7 weeks, demonstrating great potential in myocardial regeneration. Following studies have focused on directing cardiac differentiation of ES cells with high yield as well as enrichment methods after differentiation [16-19]. In a more recent study, using a post-infarction rodent heart model, functional improvements including smaller infarct size, less severe cardiac remodeling and improved LV fractional shortening have been observed following the transplantation of hESC-derived cardiomyocytes [20]. Nevertheless, the actual widespread clinical applications using ES cells have been limited by ethical and political issues.

Adult Stem Cells: Bone Marrow-derived Stem Cells

Bone marrow (BM)-derived stem cells are another potential cell reservoir for myocardial regeneration [21]. Hematopoietic stem cells (HSCs, the common ancestor of all types of blood cells) isolated from BM have long been studied and are now routinely used in clinic to treat patients with cancers and other disorders blood and immune systems [22]. Later studies have documented a subset of non-non-HSCs isolated from BM that could give rise to osteoblasts and adipocytes. These cells are termed as mesenchymal stem cells (MSC), which have the potential to differentiate into any tissue of mesenchymal origin [23]. Surprisingly, recent studies even indicated that MSCs can differentiate into cardiomyocytes both in vitro and in vivo [24, 25]. These findings initiated intensive studies of using MSCs for cardiac repair. Based on animal models of infarction, several groups have shown that MSC injected into ischemic myocardium are able to engraft and acquire the characteristics of cardiomyocytes, more importantly, they contribute improved cardiac functions [24, 26-29]. Encouraged by the initial positive results on animal models, a couple of clinical trials of MSCs transplantation were performed on patients with acute myocardial infarction. A randomized clinical trial done by Chen and his colleagues demonstrated significant improvement of LV function after intracoronary injection of autologous BM-derived MSCs on 69 patients who underwent primary percutaneous coronary intervention within 12 hr after onset of acute MI [29]. Currently, larger randomized multi-center Phase I trials using allogeneic MSCs are being conducted in the United States by Osirs Therapeutics in patients with acute MI. In spite of improved cardiac functions, a close look of

some studies with MSCs transplantation showed little, if any, cardiomyocytes transdifferentiation [30, 31]. The lack of large number of neo-myocytes from transplanted stem cells ruled out the beneficial effect contributed from direct myocardial regeneration. However, cell based therapy is a very complex process, and the observed beneficial effects of MSC transplantation could still be by angiogenesis and trophic factors of transplanted cells (paracrine effects).

Adult Stem Cells: Cardiac Stem/Progenitor Cells (CSCs/CPCs)

Till the end of last century the whole society still believed that the heart is a post-mitotic organ and that myocytes are terminally differentiated which lack the ability to replicate. However, this belief was challenged by recent studies that documented activation of the cell cycle machinery, karyokinesis and cytokinesis in a subpopulation of myocytes [32-34], which led to search for cardiac stem cells in adult hearts. So far, studies have demonstrated existence of four types of stem cell-like populations in adult hearts, termed as cardiac stem/progenitor cells (CSCs/CPCs). These cells are characterized by expressing different combinations of stem cell-related antigens such as c-kit [35], Sca-1 [36], MDR-1 [37, 38], etc, all of which have been shown to be capable of self-renewing as well as differentiating into functional cardiomyocytes.

Although both the origin of these cells and their phenotype signature remain be elucidated, nevertheless, several animal studies have been initiated using CSCs/CPCs transplantation for myocardial regeneration purpose. Anversa's group showed that the direct intramyocardial injection of c-kit+ cells into an ischemic rat heart reconstituted well-differentiated myocardium comprising of

blood-carrying new vessels and cardiomyocytes with the characteristics of young cells [35]. More recently Wang et al. reported that sca-1^+/$CD31^-$ derived from hearts possessed stem cell characteristics, and when transplanted into a murine model of MI, they led to functional preservation as well as improved myocardial bioenergetics [39]. Besides the potential therapeutic applications of direct transplantation, the research of CSCs/CPCs also illustrated the mechanism of cardiac remodeling upon damage, cardiac aging and myocardial regeneration [40,] There has been little evidence of significant cardiomyocyte transdifferentiation of transplanted adult stem cells [30, 31], yet functional improvements including decreased scar size have been observed. The underlying mechanism of beneficial effects may be due to activation/recruitment of endogenous cardiac stem/progenitor cells upon transplantation.

Induced Pluripotent Stem (iPS) Cells

It is probably a most exciting scientific breakthrough that, lineage-restricted cells can be **reprogrammed** to a pluripotent state through overexpression of defined transcription factors (Oct3/4, Sox2, c-Myc, and Klf4) [42]. Recent studies have successfully driven mouse [43-45] and human [42, 46, 47] fibroblasts into induced pluripotent stem cells (iPSCs) which functionally and phenotypically resemble embryonic stem cells (ESCs). The induced pluripotency property (vs multipotency of adult stem cells) of iPSCs suggests the potential therapeutic applications such as neural [42] and cardiac [48-50] regeneration without worrying about the ethical issues (such as using ESCs) since the patients' own cells can be reprogrammed and used.

The in vivo applications of using iPSCs for cardiac repair have been initiated very recently. Nelson and colleagues demonstrated that an intramyocardial injection of iPSCs into infarcted murine heart resulted in improved ejection fraction and attenuated adverse remodeling in a one-month follow up. Absence of teratoma formation was observed if immuno-competent animals were used [51]. However, the clinical applications using iPSCs are also subject to a number of limitations. The commonly used factors Oct4, c-Myc and Klf4 to drive the pluripotency are known oncogenes, and the genome-integrating viral vectors used for reprogramming the cells are generally prohibited in human applications. Nevertheless, alternative methods of virus-free cell reprogramming are now available such as direct plasmids, minicircle DNA, micro RNA or protein delivery [52-56].

1.2.2 Enhancing the Efficacy of Stem Cell Therapy

In spite of consistently observed improvement of LV contractile function after stem cell therapy in numerous studies, the cell engraftment rate a few weeks after cell transplantation is usually very low [39, 57-60]. Furthermore, those that do engraft mostly remain as spindle-shaped stem cells and do not fully differentiate into host cardiac cell phenotypes [59-62]. Therefore, in order to enhance the efficacy of stem cell therapy, techniques that could increase engraftment rate, promote proliferation of engrafted cells, and direct transdifferentiation into cardiomyocytes are urgently needed. In this section a few state-of-the-art techniques in stem cell therapy are to be reviewed.

Versatile Delivery Methods

An appropriate delivery method is critical to the success of clinical application of stem cell therapy for ischemic heart disease. Currently a most widely used delivery method is to direct inject stem cells into myocardium through epicardium (intramyocardial injection) [27, 63, 64]. The advantage of this method is easy control of injection sites, with a preference of viable zones surrounding ischemic area (border zone, BZ). However, usually an invasive thoracotomy or sternotomy is required, which is associated with intraoperative and postoperative risks. A less invasive method of delivering stem cells is transendocardial injection, i.e. cells are injected through the endocardium into the myocardium [65-67]. Access may be gained from the arterial vasculature, however, it requires identifying the ischemic area (usually by magnetic resonance imaging (MRI) perfusion studies and/or electromechanical mapping) before injection. Both intramyocardial and transendocardial injections have been shown to cause microscopic scarring around the needle tracks, which may isolate the injected cells and prevent integrating into the native myocardium. Moreover, Multi injections are required for covering a major area of BZ, usually resulting in a random and patchy pattern of repair. The stem cell transplantation via direct intramyocardial injection is associated with significant cell loss (>50% in a few hours) because of the active pulsate intramyocardial pressure that squeezed out the transplanted cells [68].

Intracoronary [59, 69-71] and intravenous [72] injections are two alternative methods with smaller risks compared to direct injection into myocardium and thus are especially suitable for clinical applications. Intracoronary delivery is accessed

arterial vasculature. Stem cells are injected into the lumen of coronary artery, with an inflated balloon to prevent proximal washout. Intracoronary administration allows stem cells to be evenly distributed in BZ and ischemic area through systems, in great contrast to “islands” like patterns in direct myocardial injections. Intravenous delivery is the easiest and safest access of stem cell to the without the need for cardiac surgery or cardiac catheterization. This method is based on some homing mechanism of stem cells to localize in the infracted myocardium. However, the pulmonary first pass diminishes the effectiveness of this approach. The schematic view of these delivery methods are shown in 1.1.

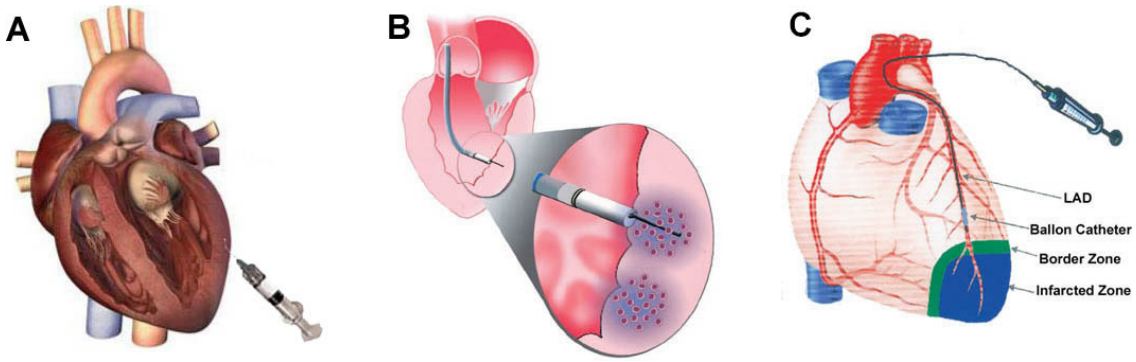

Figure 1.1 Different delivery methods of stem cell therapy in ischemic heart disease.
A, intramyocardial injection; B, transendocardial injection[73]; C, transcoronary injection[74].

Various Cytokines

It has been hypothesized that the beneficial effects associated with stem cell (especially adult stem cells) therapy for ischemic heart disease is largely attributed to the paracrine mechanism, i.e. the transplanted stem cells release soluble factors that contribute to cardiac repair and regeneration [75]. Therefore, a

rationale approach for enhancing the efficacy of stem cell therapy would be to engineer the transplanted stem cells to overexpress those trophic factors, especially the cytokines capable of regulating cell differentiation, proliferation, survival and functioning.

One important criteria of stem cell therapy is the cell survival and functioning. Recently, numerous studies suggest that constitutive expression of Akt (a serine threonine kinase) can decrease cell apoptosis after transplantation [76]. Therefore, more studies were initiated to test the effect of Akt on therapeutic transplantation of stem cells in ischemic heart disease. Rat MSCs with overexpressed Akt1 were transplanted into ischemic myocardium and were found to reduce inflammation and myocyte hypertrophy in a dose-dependent fashion, and thus prevent negative cardiac remodeling secondary to infraction [77]. Another study on ischemic porcine model also showed encouraging results, with higher ejection fraction (EF) observed in Akt-transduced MSCs group compared to non-transduced MSCs group [78]. Other factors with prosuvival effects have also been extensively studied, including insulin-like growth factor 1 (IGF-1) [79], cardiotrophin 1 (CT-1) [80], heme oxygenase 1 (HO-1) [81] and so on. More recently, Dr. Sussman and colleagues have demonstrated the cardio- and mitochondrial protective property of serine-threonine kinase (Pim-1) [82, 83]. Later on, the same group genetically modified cardiac progenitor cells (CPCs) to overexpress Pim-1 and transplanted the engineered CPCs for cardiac therapy. The transplantation of Pim-1 overexpressed CPCs resulted in significantly enhanced efficacy in terms of cellular survival, proliferation and regeneration [84].

Another possible mechanism of beneficial effect from stem cell therapy might be increased angiogenesis since neo-capillaries instead of neo-cardiomyocytes were observed after stem cell transplantation. Therefore, a straightforward strategy of enhancing efficacy of stem cell therapy would be to direct increase vasculogenesis function of stem cell by overexpressing certain growth factor, e.g. vascular endothelial growth factor (VEGF). Numerous studies were carried out to examine the effect of VEGF transfected stem cells, with encouraging results showing increased neovascularization and improved LV function [58, 85, 86]. Hepatocyte growth factor (HGF) is another growth factor known to regulate both proliferation and migration of endothelial cells, thus promoting angiogenesis. Studies on a rat model of myocardial infarction showed increased engraftment of cardiac stem cells and subsequent enhanced regeneration of entire coronary vasculature due to IGF-1 and HGF [87].

Engineered Biomaterials

Engineered biomaterials have provided promising modalities to facilitate the cardiac repair for ischemic heart disease, including polymeric LV restraint devices, in vitro engineered cardiac tissue and in situ engineered cardiac tissue. An illustrative view of these approaches using engineered biomaterials is given in Figure 1.2.

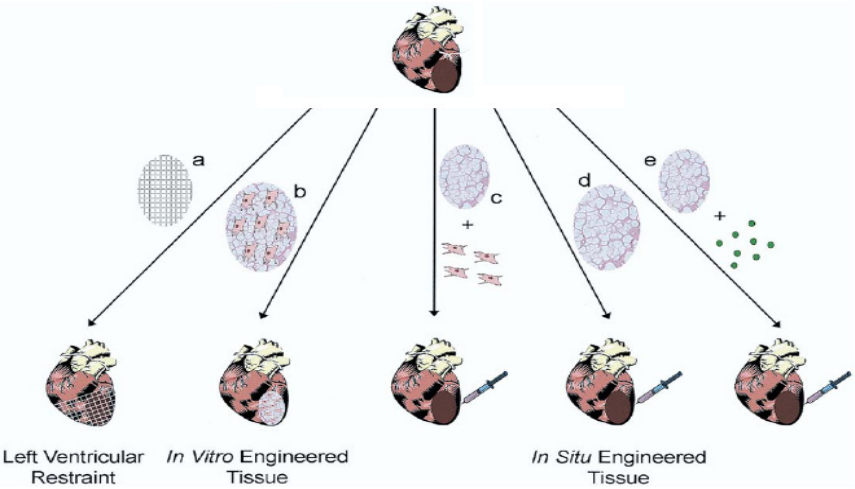

Figure 1.2 Strategies of cardiac repair using engineered biomaterials. [88] a, LV restraint; b, tissue equivalent (cells cultured in biomaterials in vitro) is transplanted; c, biomaterials together with stem cells are transplanted in situ for repair; d. injectable biomaterial alone is transplanted; e, biomaterials pre-loaded with growth factors are transplanted.

LV restraints have long been studied and showed beneficial effects on slowing LV remodeling after MI both on animal models and patients [89, 90]. The mechanism of the beneficial effects is probably restoring the LV to a more normal geometry and alleviating the stress of infracted area. However, this therapy does not provide a final solution for ischemic heart disease, since the pathophysiology of remodeling after myocardial infarction is a very complex process including molecular, cellular, and interstitial changes, and it is unlikely one could rely solely on LV restraints to solve this problem.

Tissue engineering approaches aim at restoring, maintaining, or enhancing tissue and organ function through cellular transplantation and biomaterial Numerous studies have been dedicated to this field and different scaffolds as as various culture conditions for creating in vitro engineered myocardial tissue have been developed [91-94]. In one study, a monolayer sheet of MSCs was applied

to the surface of ischemic myocardium, with improved cardiac function observed However, several issues will have to be addressed to improve the complexity and function of engineered myocardium: the high numbers of cardiac myocytes need be made available, the survival rate of cardiac myocytes in a three-dimensional environment needs to be improved, the size of three-dimensional myocardium needs to be increased, and the engineered myocardium must withstand appreciable force. Besides, as seen with other in vitro tissue engineering approaches, the majority of external myocardial tissue constructs are limited to a thickness of 100 μm or approximately 6 cardiomyocytes, which is unlikely to produce noticeable changes in human myocardium [88].

In situ tissue engineering is a recently emergent field aiming at providing a tailored microenvironment for transplanted cells. By elaborately designing the biomaterials, quantitative adhesion, growth or migration signals for transplanted cells could be delivered in a spatially and temporarily controlled fashion [96]. Some widely used biomaterials in this regard include natural and modified fibrinogen/fibrin, Matrigel and alginate, together with other synthetic polymers. Fibrin has many advantages as a cell delivery vehicle in terms of biocompatibility, biodegradability and hemostasis [97]. Several studies indicated that both fibrin glue alone and fibrin based biomatrix for stem cell therapy showed beneficial effects to infracted hearts [30, 98, 99]. A more recent report utilized PEGylated fibrin to deliver both MSCs and SDF-1 to infracted hearts. The results showed increased stem cells homing to the infracted area as well as improved LV function [100]. In another study, cardiomyocytes derived from hES cells were delivered to infracted mouse

hearts using a Matrigel based injectable biomatrix, within which a cocktail of pro-pro-survival factors was also provided. The results showed significant increase in engraftment rate as well as improved LV function [20]. Lee et al. recently designed self-assembling peptide nanofibers for prolonged delivery of IGF-1, a cardiomyocyte growth and differentiation factor to the myocardium in a “biotin sandwich” fashion [79]. Biotinylated IGF-1 was complexed with tetravalent streptavidin which in turn bound to biotinylated self-assembling peptides. The self-assembled nanofibers could provide sustained localized delivery of IGF-1 for 28 days. And when combined with cardiomyocytes transplantation to infracted myocardium, significantly improvement of systolic function was observed.

1.3 Background of Nuclear Magnetic Resonance Technology

Nuclear Magnetic Resonance (NMR) refers to the absorption/emission of electromagnetic radiation by nuclei in a strong external magnetic field. NMR was simultaneously discovered by Bloch and Purcell in 1945, who later shared the Nobel Prize for physics in 1952. Right now, NMR technology, including magnetic resonance spectroscopy (MRS) and magnetic resonance imaging (MRI), has already developed into a most powerful tool for many fields, such as chemistry, medicine, biology and so on. In this section, we review the basic principles in NMR technology as well as some techniques widely utilized in various in vivo NMR studies.

1.3.1 Fundamental of NMR

Larmor Frenquency: Classical and Quantum Mechanical View of NMR Phenomena

NMR phenomena can be described using both classical and quantum mechanism. Quantum mechanism gives a more accurate description of NMR, whereas, classical gives a more tangible interpretation, especially for the effect of radiofrequency (RF) pulses on the bulk magnetization vector. Nevertheless, both mechanisms result in the same equation characterized by Larmor frequency [101].

In classical view a nucleus is considered under spinning motion, i.e. rotating about itself. Since nucleus carries net charges, the spinning creates a magnetic moment μ given by:

$$\mu = iA = \frac{ev}{2\pi r}\pi r^2 = \frac{e}{2M}Mrv = \gamma P \qquad [1.1]$$

where i is the electric current from rotating objects carrying charges, r and A are the radius and area of the current loop, e, M, v, P are the charge, mass, velocity and angular momentum of the nucleus respectively, and finally γ is the gyromagnetic ratio. Equation [1.1] dictates that when an external magnetic field B_0 is present, a torque would be generated, resulting a precession motion of nuclear magnetization about B_0:

$$\frac{d\vec{\mu}}{dt} = \gamma\vec{\mu}\times\overrightarrow{B_0} \;\Rightarrow\; \nu_0 = (\gamma/2\pi)B_0 \qquad [1.2]$$

where v_0 is the frequency of nucleus precessing about B_0 (Larmor frequency).

In contract, quantum mechanism describes spin as an intrinsic character of nucleus governed by spin quantum number. The magnitude and orientation of

angular momentum associated with nuclear spin are quantized. Another quantum number called magnetic quantum number is introduced to describe the projection of the angular momentum for any given direction (L_z) as:

$$L_Z = (h/2\pi)m \qquad [1.3]$$

where h is the Plank's constant, and m is the magnetic quantum number. For nucleus with a spin quantum number of 1/2, m can only be ±1/2. a magnetic moment along z direction is given by:

$$\mu_z = \lambda(h/2\pi)m \qquad [1.4]$$

When an external magnetic field B_0 is applied, nuclei with 1/2 spin quantum number can develop into two different energy levels given by:

$$E_{\pm} = -\mu_z B_0 = (\pm 1/2)(h/2\pi)\gamma B_0 \qquad [1.5]$$

The energy gap enables the nucleus to make resonant exchange of energy from applied electromagnetic field when the following condition is fulfilled:

$$\Delta E = h\nu_0 \Rightarrow \nu_0 = (\gamma/2\pi)B_0 \qquad [1.6]$$

where v_0 is the frequency of the resonant electromagnetic field and called Larmor frequency.

Macroscopic Magnetization and Bloch Equations

So far we have been discussing individual nucleus, however, in practice NMR technology always deals with macroscopic magnetization resulting from bulk matter. The two energy states of nucleus in an external magnetic field (for those with 1/2 spin quantum number) dictate that there are two possible directions of each μ_z, i.e. parallel or anti-parallel to the external field. In equilibrium there will

a small preponderance for those aligning parallel to the field. This preponderance is governed by Boltzmann factor:

$$n_\alpha / n_\beta = \exp\left(h\nu / kT\right) \qquad [1.7]$$

where n_α/n_β is the ratio of parallel to anti-parallel nuclear spins, h is Plank's constant, v is the frequency of precession, k is the Boltzmann constant and T is absolute temperature. Summation of individual nuclear magnetization results in a net macroscopic magnetization (M_0) lying parallel to external field as:

$$M_0 = \left(\gamma h / 2\pi\right)^2 \left(nB_0 / 4kT\right) \qquad [1.8]$$

where $n=n_\alpha+n_\beta$.

The Bloch equation describes the motion over time of the bulk magnetization vector M following a RF pulse excitation, when viewed under rotating frame it has the form as:

$$\begin{cases} \dfrac{dM'_x}{dt} = (\omega_0 - \omega)M'_y - \dfrac{M'_x}{T_2} \\ \dfrac{dM'_y}{dt} = -(\omega_0 - \omega)M'_x + \gamma B_1 M'_z - \dfrac{M'_y}{T_2} \\ \dfrac{dM'_z}{dt} = -\gamma B_1 M'_y - \dfrac{M'_z - M_0}{T_1} \end{cases} \qquad [1.9]$$

where ω_0 is the angular velocity of Larmor precession, ω is the angular velocity applied RF pulse, T_1 is the longitudinal relaxation time (spin-lattice relaxation T_2 is the transverse relaxation time (spin-spin relaxation time) and B_1 is the RF pulse. Here the rotating frame refers to Cartesian axes x', y', and z', with z' along the direction of B_0 and rotating with a frequency the same as applied RF pulse. Figure 1.3 gives a schematic view of motion of bulk magnetization vector

following excitation of 90° pulse.

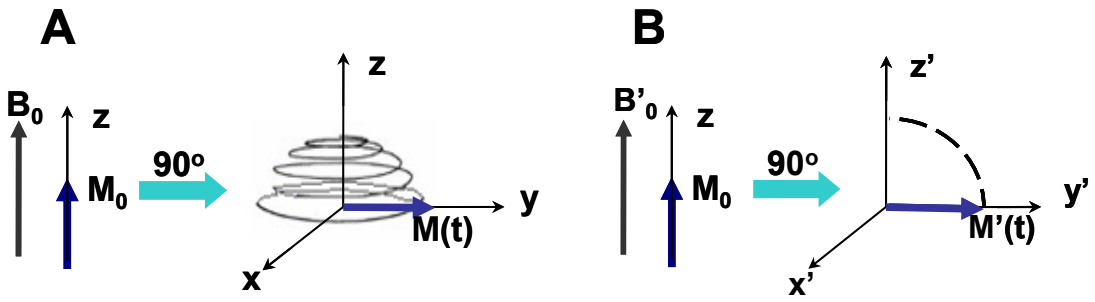

Figure 1.3 Motion of bulk magnetization vector following 90° pulse. (A) viewed in laboratory frame; (B) viewed in rotating frame.

Fourier Transform NMR and Chemical Shift

Following an RF pulse which is designed to rotate M_0 by 90° onto transverse plane, the bulk magnetization vector would precess about B_0 at the Larmor frequency. This motion would induce an electromotive force (emf) in a receiving coil and recorded by computer. Because of T_2 relaxation as well as B_0 inhomogeneities, the emf would decay exponentially as spins precess about B_0, which is call free induction decay (FID).

FID holds all information about the nuclear spins of interest, however, they seldom used directly. Instead, this time-domain data (i.e. FID) is transformed into frequency-domain data (i.e. spectra) by a Fourier Transformation (FT) which performs according to:

$$F(\omega) = \int_{-\infty}^{+\infty} f(t) \exp(-i\omega t) dt \qquad [1.10]$$

where f(t) refers to the time-domain signal and F(ω) refers to the frequency-time spectra.

So far little has been discussed that enables NMR for various applications. As a matter of fact, it is the highly sensitive dependence of Larmor frequency on chemical environment that makes NMR a powerful analysis tool. The subtle chemical environment where the nucleus resides will place a shielding effect to the external magnetic field B_0, reducing the actually external magnetic field sensed by the nucleus. This effect can be expressed as:

$$B = B_0(1-\sigma) \qquad [2.11]$$

where σ the shielding constant, usually expressed in parts per million (ppm). Therefore, the actual precession frequency of nucleus under certain chemical environment is:

$$\nu = (\gamma/2\pi)B = (\gamma/2\pi)B_0(1-\sigma) = \nu_0(1-\sigma) \qquad [1.12]$$

Equation [1.12] indicates that v depends on external magnetic field. In order to make comparisons of data from different spectrometers much easier, a new term, chemical shift, is introduced as:

$$\delta = \frac{\nu_s - \nu_{ref}}{\nu_{ref}} \times 10^6 \qquad [1.13]$$

where v_s and v_{ref} are frequencies of the sample and a reference compound, respectively. The reference compound should ideally be chemically inert and its chemical shift should be insensitive to external environments such as temperature, ionic strength, etc. A widely accepted reference compound for ^1H and ^{13}C NMR is tetramethylsilane (TMS) to which δ=0 is assigned. As to *in vivo* ^{31}P MRS study, Phosphocreatine (PCr) resonance is employed as reference.

1.3.2 Spatial Localization of in vivo MRS

Restricting signal from a well-defined region of interest (ROI) is crucial for meaningful in vivo MRS. For example, heart failure due to ischemic heart disease is very heterogeneous, both from infarct zone to remote zone and from epicardium to endocardium. A non-localized MRS would be meaningless because the signal obtained is an ill-defined mix of pathologic region and healthy region 2. So far numerous localization techniques have been described in the literature and a few have achieved widespread use. These techniques may be crudely divided into three broad classes: Surface coil and pulses localization; static field gradients localization, and MR spectroscopic imaging [102].

Spatial Localization Based on Coil and Pulse Sequence

Localization techniques based primarily on properties of RF coil and pulses dominated the early years of localized MRS. A first in vivo localized NMR experiment was carried out by Ackerman et al, who collected localized spectra from rats simply by placing a small tuned coil on the surface of the animal and relying on the B_1 field profile of the coil for localization [103]. It is common to assume that the surface coil acquisition is localized to an approximately hemispherical region, however, sensitivity is non-uniform within this region and signal outside of this region is not negligible. Nevertheless, such surface coils have subsequently found many applications in imaging and spectroscopy due to its simplicity in implementation [104, 105].

As an amendment to surface coil localization, depth pulse technique aims at improving depth selection by suppressing signal from regions in which the flip

angle (θ) differs from 90^o. This concept was initially introduced by Bendall and his colleagues [106, 107]. It can be shown that the signal produced by depth pulse sequence is proportional to $B_1\sin^3(\theta)$, which has a tendency to eliminate signal from areas where $\theta \neq 90^o$.

A further development in localization pulse sequence is rotating frame spectroscopy introduced by Hoult [108]. The mechanism works similar as in conventional MRI phase encoding: if a constant linear B_1 gradient is achieved by clever coil design, an application of such B_1 field along x'-axis in rotating frame would cause z magnetization to nutate towards y'-axis through an angle (θ) varying linearly with distance from the coil along x direction. The spatial information can be incorporated into an FID by applying a 90^o detection pulse along y', and further retrieved by two-dimension Fourier transformation of repetitive experiments with different nutation angles. This technique suffers from time and SNR inefficiency (two-dimensional Fourier Transformation) and complex instrumentation (sophisticated coil for generating linear B_1 gradient). The first drawback was overcome by Fourier Series Window (FSW) approach, introduced by Dr. Garwoood and associates, which eliminated redundant scans as well as maximized SNR from region of interest [109]. The second drawback was largely overcome by adiabatic pulse-based techniques such as FLAX-ISIS [110] and RAPP-ISIS [111, 112], developed by Drs. Ugurbil, Garwood and their colleagues.

Spatial Localization Based on Static Field Gradient

All B_0 gradient-based spatial localization methods rely on the selection of a spatial splice by the application of a frequency-selective RF pulse in the presence

of a B_0 gradient. When B_0 gradient is present, nuclear spins at different locations along the gradient would precess at different Larmor frequency which direct depends on the location. Then a frequency-selective RF pulse becomes a spatial-selective pulse, giving a spatial selectivity as:

$$\Delta L_i = \frac{\Delta \omega_i}{\gamma G_i} \times 10^{-2} \qquad [1.14]$$

where subscript i defines the gradient orientation and can be x, y, or z; $\Delta\omega_i$ (in unit of Hz) is the bandwidth of the frequency-selective pulse, G_i (in unit of Gauss/cm) is the B_0 gradient along i direction, and ΔL is the thickness of the slab selected by the RF pulse.

Typically, a cuboidal region is defined by applying slice selective pulse clusters to prepare spins along each of three orthogonal axes in turn. The volume of interest (VOI) is formed at the intersection of the prepared slices. Of course, one or two-dimensional localization can be easily achieved by applying fewer clusters. Representative spatial localization techniques in this category includes: Image Selected In vivo Spectroscopy (ISIS) [113], STimulated Echo Acquisition Mode (STEAM) [114, 115] and Point RESolved Spectroscopy (PRESS) [116-118]. The STEAM and PRESS techniques generate signals from VOI directly, and thus no post-acquisition subtraction/adding is required to suppress signals from outside of VOI (such as ISIS). However, both STEAM and PRESS rely on multiple echo signals to achieve localization, thus incompatible with nuclei with short T_2 (such as ^{31}P).

Unlike the above mentioned techniques, which achieve single voxel localization, another technique termed as chemical shift imaging (CSI, also

as MR spectroscopic imaging, MRSI), is capable of collecting spectra with one-, two- or even three- dimensional array of voxels simultaneously [119]. Chemical shift imaging could be regarded as a special case of MRI, where spatial differentiation achieved by phase encoding steps. With CSI technique, it is feasible to map metabolites levels within an organ (such as brain, breast and heart). The spatial information of metabolites level can then be co-registered with anatomic information from MRI, thus providing biochemical insight into the organs' pathophysiologic condition, such as lesion, infarct, etc.

1.4 Myocardial Bioenergetics Studied by in vivo ^{31}P MRS

As a most energy intensive organ, the heart has to precisely couple and continuously balance the energy production, transport and utilization. When left ventricle undergoes remodeling upon pathophysiologic condition, alternations of both thermodynamic high energy phosphate (HEP) levels and adenosine triphosphate (ATP) production flux rate through creatine kinase (CK) are observed. Also, when treatments were applied, normalization of myocardial energetics is observed corresponding to cardiac functional improvement. Therefore, not only is myocardial energetics critical to understanding cardiac function in both normal and pathophysiologic states, but also it serves as a criterion for determining the efficacy of therapeutic treatments and even help elucidate the mechanism of observed beneficial effects.

Traditionally myocardial energetics has been assessed via invasive measurements, however, its application in clinical practice is greatly limited. In

recent years, the development of in vivo ^{31}P MRS has provided a non-invasive alternative to assess myocardial energetics and resulted in numerous new findings.

1.4.1 Myocardial Energetics in Normal Hearts

Myocardial energy metabolism consists of four components, (1) substrate utilization, (2) energy production and (3) energy transport and (4) energy utilization.

Substrate utilization refers to uptake of fuel molecules by cardiomyocytes and subsequent biochemical decomposition for energy production. The cardio-myocytes have a preference for fatty acids (60~90%) to glucose/lactate (10~40%) as energy substrates, which undergo beta-oxidation or glycolysis to enter citric acid cycle, respectively. The citric acid cycle occurs in the mitochondrial matrix and can be briefly described as:

$$\text{Acetyl-CoA} + 3\text{NAD}^+ + \text{FAD} + \text{GDP} + \text{Pi} + 2\text{H}_2\text{O} \rightarrow 2\text{CO}_2 + 3\text{NADH} + \text{FADH}_2 + \text{GTP} + 2\text{H}^+ + \text{CoA}$$

where NAD^+/NADH is nicotinamide adenine dinucleotide in oxidized and reduced forms, FAD/$FADH_2$ is flavin adenine dinucleotide in oxidized and reduced forms, GDP/GTP is guanine diphosphate and triphosphate, Pi is inorganic phosphate.

The NADH and FDH_2 produced in citric acid cycle provide electrons that flow through a system of large protein complexes and finally to oxygen, thus generating a proton gradient across the inner membrane of mitochondrial. F_0F_1-F_0F_1-ATPase (also termed ATP synthase or H^+-ATPase) utilizes this proton gradient for substrate level phosphorylation of adenosine diphosphate (ADP) to

synthesize ATP via the following reaction:

$$\text{Acetyl-CoA} + 3\text{ADP} + 3\text{Pi} + \text{NADH} + \text{H}^+ + 1/2\,\text{O}_2 \rightarrow 2\text{ATP} + 4\text{H}_2\text{O} + \text{NAD}^+ + \text{GTP}$$

Therefore, oxidation and phosphorylation are coupled by a proton gradient spanning the inner membrane of mitochondrial. This is the main means of ATP production in cardiomyocytes.

ATP produced in such a way must be transported from mitochondrial to the site of energy utilization, i.e. myofibrils in cytosol. This transportation is greatly facilitated by a mechanism called creatine kinase/phosphocreatine (CK/PCr) shuttle [120] in addition to the free diffusion of ATP itself. The mechanism is characterized by fast-equilibrium reactions catalyzed by creatine kinase:

$$\text{Cr} + \text{ATP} \overset{CK}{\Leftrightarrow} \text{PCr} + \text{ADP} + \text{H}^+$$

Different types of CK isozymes are present at both mitochondria and cytoplasm, catalyzing fast exchange between ATP and PCr with a reaction rate exceeding that of ATP synthesis by about an order of magnitude [121-124]. Since phosphocreatine has a greater intracellular diffusivity compared to ATP, by establishing fast equilibrium between ATP and PCr, free energy transportation is greatly accelerated.

In addition to facilitating free energy transport, two other functions are also ascribed to CK system: (1) to provide temporal ATP buffering and (2) to ensure local ATP buffering. The first function is pronounced during periods of excessive cellular activity when ATP demand temporarily exceeds ATP delivery. And the latter one is based on the observation of low local ADP/ATP ratio near ATPase whereas high ADP/ATP ratio near ATP synthase [125-127].

Energy utilization occurs when ATP is hydrolyzed by cytosolic ATPase to generate contractile force (other cellular process also consumes ATP, however contracting work is the major way of energy utilization in cardiomyocytes).

Using in vivo ^{31}P MRS technique, the dynamics of high energy phosphate (HEP) levels, such as ATP, PCr and inorganic Pi can be readily measured. Moreover, a unique method termed saturation transfer (ST) of ^{31}P MRS can be utilized to interrogate the in vivo chemical flux of the two important enzymes regulating the ATP metabolism, namely, Creatine kinase and ATP synthase.

1.4.2 Impaired Myocardial Energetics upon Pathophysiologic Conditions

Abnormal myocardial energy metabolism is a consistently observed both on animal models and clinical practices with various cardiac pathologies [128, 129], including myocardial infarction [130, 131], left ventricular hypertrophy [132], dilated cardiomyopathy [132, 133], hypertension [134] and valvular disease [135].

One most prominent abnormality of myocardial energetics in diseased hearts is decreased phosphocreatine-to-ATP (PCr/ATP) ratio as well as reduced HEP levels. In fact, PCr/ATP has already been considered an important predictor of mortality in patients with heart failure [132]. Worthy of notice here is a series of studied on large animal models carried out by Dr. Zhang's group, with the emphasis on abnormal myocardial energetics upon various pathophysiologic conditions. For example, they have created a porcine model of postinfarction LV remodeling (LVR) by acute coronary occlusion [105, 136, 137]. In the study remarkable remodeling of non-infarcted myocardium with LV chamber dilation, reduced systolic performance, increased wall stress and reduced PCr/ATP were observed

and correlated well with the size of the initial infarct. In another study also carried out by the same group, concentric LV hypertrophy was created by severe aortic band on a porcine model. The following LV remodeling resulted in reduction of HEP levels as well as a decrease of PCr/ATP ratio. Furthermore, these abnormalities are in linear correlation to the degree of hypertrophy [104].

Another important issue of reduced PCr/ATP upon disease condition would be how this alteration contributes to LV dysfunction. A reduction in PCr/ATP would direct result in an increase of myocardial free ADP level, which in turn would activate adenylate kinase (myokinase) to catalyze two ADP to form one adenosine monophosphate (AMP) and one ATP [138, 139]. The increased AMP would induce conversion of AMP to adenosine, which can cross the cell membrane into interstitial space, where it is further degraded to inosine, hypoxanthine and leaves the heart via myocardial blood flow [140]. The whole process causes loss of total adenine nucleotide pool (TAN), which would result in a reduction of ATP level (up to 30% decrease in failing heart). As a result of the combined effects of increased ADP and reduced ATP level, myocardial ATP/ADP ratio would be significantly decreased, which in turn reduce myocardial free energy release per unit ATP hydrolysis [141].

A third alteration in myocardial energetics upon pathophysiologic condition is the reduced ATP synthesis flux rate through CK [137, 142]. The impaired CK system associated with a decrease of CK-MM isozyme and an elevation of B-containing CK isozyme [143, 144]. This observation led to a hypothesis that failing myocardium energy starving. One approach to test this hypothesis is to impair CK system

independent of heart failure/hypertrophy. This has been done by targeting the CK enzyme (CK inhibitor [141] or CK knock out [145-148]) or creatine substrate (β-(β-Guanidinopropionate feeding [149, 150]). It was shown that contractile reserve decreased in line with decreasing CK activity and an inverse linear relationship between contractile performance and ΔG_{ATP} was demonstrated [151]. Interestingly, this is consistent with the previous findings that failing hearts have a decreased energy reserve which became pronounced under high-work state [136, 152].

In a word, abnormalities in myocardial energetics are prominent in various heart diseases with obvious correlation with severity of pathophysiologic conditions. Furthermore, in studies aiming at therapies to heart diseases, normalization of myocardial energetics is also observed together with improved cardiac function. For example, standard medical therapies including ACE inhibitors, digitalis, diuretics and beta-blockers were given to patients with dilated cardiomyopathy. The results showed cardiac function improvement, together with a normalization of PCr/ATP ratio from 1.51±0.32 to 2.15±0.27138. More interestingly, a number of studies aiming at applying stem cell therapy for ischemic heart disease also observed normalization of PCr/ATP in cell treated group compared to control group, which further supported the feasibility of myocardial energetics as a useful criterion for judging the therapy effect [58, 60].

Chapter 2

CARDIAC REAPIR USING A FIBRIN PATCH-BASED TRANSPLANTATION OF HUMEN EMBRYONIC STEM CELL-DERIVED VASCULAR CELLS

2.1 Introduction

Myocardial infarction (MI) often induces a period of left ventricular (LV) remodeling. When LV remodeling occurs, an initial period of hemodynamic stability is followed by the development of LV dysfunction that may eventuate in congestive heart failure (CHF). The mechanisms that contribute to the transition from the compensated state to CHF remain unclear, but may be related to progressive contractile dysfunction of the border zone (BZ) region of viable myocardium that surrounds the infarct [153, 154].

Both experimental and clinical evidence demonstrate that cellular transplantation can improve the LV contractile performance of failing hearts [27, 62, 69, 155 30]. The underlying mechanisms remain unclear. Transplanted cells may

regenerate myocytes and new vessels, and they may also release cytokines that exert trophic effects on host cardiac cells. We hypothesize that the beneficial effects of BZ stem cell engraftment result in increased neovascularization in the ischemic zone (IZ) and possibly BZ, and paracrine effects on stressed native cardiomyocytes in the BZ. This leads to stabilization of BZ bioenergetic and contractile function, which in turn is associated with attenuated myocyte and expansion of the BZ size.

Although it is a consistent observation in the literature that cellular transplantation improves LV contractile function, the cell engraftment rate a few weeks after the transplantation is usually very low [39, 57-60]. Therefore, it is clear that majority of cells transplanted to the heart do not demonstrate durable engraftment. Further, the majority of transplanted cells that do engraft do not differentiate into host cardiac myocytes cell phenotypes [59-62].

We have recently developed a novel 3D porous fibrin biomaterial that can bind to growth factors to create an optimal microenvironment for stem cells to reside [30, 100, 156, 157]. The biomaterial can also function to control prolonged release of growth factors (SDF-1α) to mobilize the endogenous cardiac progenitors to the injury site enhancing the repair. Using swine and mouse models of hearts with acute myocardial infarction, we have recently shown that bone marrow derived mesenchymal stem cells (MSC) embedded in a novel 3D porous biomaterial “patch” that attached to the surface of the myocardial infarction, resulted in a remarkable increase of engraftment rate and significant functional improvements a few weeks after transplantation [30, 100, 156, 157].

Additionally, we have recently developed a novel method in differentiating hESC into endothelial (hESC-ECs) and smooth muscle (hESC-SMCs) cells, which can provide an ample source for clinical cellular therapy application in patients with heart failure [158].

In the present study, we hypothesized that the trophic effects of cellular therapy are associated with increased neovascularization and regional myocardial contractile function, reduction of LV wall stresses and myocytes apoptosis, and possibly mobilization of the endogenous cardiac progenitors to the injury site for repair. Using a well established clinically relevant pig model of postinfarction LV remodeling, and an enhanced cell delivery by the 3D porous fibrin biomatrix, we examined whether the transplantations of mixture of hESC-ECs and hESC-SMCs can ameliorate LV dysfunction and hypertrophy in hearts with post-infarction LV remodeling. Immuno-suppression was achieved by using the established xenotransplantation protocol. LV infarct size and chamber function were examined by magnetic resonance imaging (MRI). Additionally, we used an immunodeficient mouse model of postinfarction LV remodeling to assess the time course of the in vivo cell engraftment rate using molecular bioluminescent imaging (BLI). The results demonstrated that the fibrin patch enhanced delivery of hESC-ECs and hESC-SMCs resulted in a significant cell engraftment, which is accompanied by improvement of LV chamber function, reduction of infarct size and increase of neovascularization at both infarct zone and peri-infarct border zone, suggesting a promising novel cellular therapy using hESC-derived vascular cells with the novel biomatrix delivery mode.

2.2 Methods

All experiments were performed in accordance with the animal use guidelines of the University of Minnesota, and the experimental protocols were approved by the University of Minnesota Research Animal Resources Committee. The investigation conformed to the Guide for the Care and Use of Laboratory Animals published by the National Institutes of Health (NIH publication No. 85-23).

2.2.1 In vitro Studies

Embryonic Stem Cell Culture and Vascular Differentiation

Human embryonic stem cell line H9 (Wicell, Madison, WI) was maintained on mouse embryonic fibroblasts and genetically modified to express green fluorescent protein and firefly luciferase (GFP/Luc), as previously described [159]. Endothelial cells (hESC-ECs) and smooth muscle cells (hESC-SMCs) were derived from the H9 GFP/Luc cell line as previously described and cultured under EC and SMC conditions, respectively [158]. Briefly, undifferentiated hESCs were co-cultured with M210 mouse stromal cells to induce mesoderm differentiation. After 13-15 days, $CD34^{+}CD31^{+}$ hESC-derived vascular progenitor cells were sorted by magnetic nano-particle selection system. Cells were cultured on fibronectin-coated plates with cytokine containing media to support EC development. Subsequently, to generate SMCs, these cells were cultured in media containing PDGFBB and TGF-beta. Immediately prior to transplantation, cells were harvested using 0.05% Trypsin-1mM EDTA (Invitrogen, Carlsbad, CA), counted, pelleted and resuspened in 30 μL PBS solution (Hyclone/Thermo

Scientific, Waltham, MA) for mouse studies or in 1 mL fibrinogen solution (Sigma-(Sigma-Aldrich) for pig studies.

Anti-apoptotic Capability of hESC-ECs

Prior to in vivo applications, the anti-apoptotic capability of hESC-ECs was examined in vitro with HL-1 myocytes co-culture experiment.

HL-1 myocytes (Claycomb Laboratory, University of Louisiana) were plated onto fibronectin/gelatin-coated 150 cm^2 flasks and cultured in Claycomb medium supplemented with 10% fetal bovine serum, 100 U/ml penicillin, 100 μg/ml streptomycin, 0.1 mM norepinephrine, and 2 mM L-glutamine. HL-1 and hESC-were individually cultured in serum free (SF, to induce apoptosis) and serum (S) medium for 24 hr as negative and positive controls. One more flask of HL-1 was cultured in conditioned medium (C) which was harvested from the hESC-EC cultured in serum free medium for 24 hr. Apoptosis was assessed by staining with Hoechst 33342 dye and then quantified by the percentage of apoptotic nuclei. Further, the mitochondrial membrane potential changes associated with were also examined with immunostaining. HL-1 cells were plated on chamber slides the first day. After 24 hours, the cells were treated with 40ng TNFα for 6 hour to induce apoptosis. Mitochondrial inner-membrane potential changes were evaluated using mitochondria staining kit according to manufacture's direction (Sigma-aldrich, Saint Louis, Missouri). The cationic, lipophilic dye, JC-1 (5,5',6,6'-(5,5',6,6'-tetrachloro-1,1',3,3'-tetraethybenzimidazolocarbo-cyanine iodide) aggregates can be visualized in the mitochondria as bright red fluorescence, representing intact mitochondria and JC-1 monomers as the green fluorescence,

which represents disrupted mitochondria.

2.2.2 In vivo Mouse Studies

Immunodeficient NOD/SCID mice 12 weeks of age weighing 17-20 g were used for the infarct model. Acute myocardial infarction (AMI) was induced by left coronary artery ligation according to a previously described method [20]. Fifteen minutes post ligation of left anterior descending (LAD) coronary artery, mice were randomized into three groups that received saline only (MI, n=13), hESC-derived ECs (MI+EC, n=8) or a mixture of hESC-derived ECs and SMCs (MI+EC+SMC, n=13). Cell transplantation was achieved with 3 injections (total volume of 30 μL) into the peri-infarct regions with a 31-gauge needle. 1 x10^6 cells (100% hESC-EC or a 50/50 mixture of hESC-EC and hESC-SMC) were delivered to MI+EC and MI+EC+SMC groups, respectively. The functional outcome of cell transplantation was assessed by echocardiography [39] with 4-week follow-up while in vivo cell engraftment rate was measured with in vivo bioluminescent imaging (BLI) [160]. Following the 4 week echocardiogram, mice were sacrificed and the hearts excised. Mouse heart infarct size was measured by using NIH Image J software and saved tissue was subject to cryosection and immunofluorescent staining [39]. Methods detailing mouse AMI surgery, in vivo BLI, cardiac echocardiography, and immunohistochemistry staining are described as follow.

Mouse Model of Postinfarction LV Remodeling

MI was produced under a dissection microscope by permanently ligating the left coronary artery with a 9-0 nylon surgical suture. The ligation induced

approximately 30% infarction of the LV. Surviving mice were randomized into groups to receive either a direct injection of cell treatment or saline. Immediately prior to injection, the cells were harvested using 0.05% Trypsin-1mM EDTA (Invitrogen, Carlsbad, CA), counted and aliquoted. For each transplantation, $1x10^6$ cells (100% hESC-EC for MI+EC group or a 50/50 mixture of hESC-ECs and hESC-SMCs for MI+EC+SMC group) were pelleted, resuspended in 25-30 PBS (Hyclone/Thermo Scientific, Waltham, MA), drawn into a 31-gauge insulin syringe (Beckton Dickinson, Franklin Lakes, NJ), and directly injected through epicardium of the peri-infarct region with a 31-gauge needle. The chest was closed in layers. After surgery, the mice were allowed to recover for timed intervals of 4 weeks.

In vivo Bioluminescent Imaging

For post surgical in vivo bioluminescent imaging mice were given intra-peritoneal (ip) injection of 150 µL 3.75 mg Sodium Luciferin substrate (Gold Biotechnology, St Louis, MO) and lightly anesthetized using 1% inhaled isoflurane as previously described in details [161]. Fifteen minutes after introduction of the substrate, bioluminescent images were obtained using the IVIS Imaging System (Xenogen/Caliper Life Sciences, Hopkinton, MA). For quantification purposes, each image collected under standard conditions (5 minutes of exposure under the medium binning setting at the lowest shelf height). Quantification of luciferase activity using Living Image software (Xenogen) was achieved by measuring luminescent signal in photons per second within a standard digital area. Control animals without cell injection were imaged to determine background signal.

Mouse Cardiac Echocardiography

Mice were lightly anesthetized by ketamine HCl (50 mg/kg, ip) and xylazine (16.5 mg/kg, ip). Echocardiography was performed using a Visualsonics Vevo707 echocardiographic Imaging system [39, 57]. The 2-dimensional short-axis view of the LV was obtained at the level of the papillary muscles. The LV internal dimensions, such as end-diastolic and end-systolic dimensions, were measured by the leading-edge method from at least 8 consecutive cardiac cycles on the short-axis view of the LV and were used to calculate the ejection fraction (EF) and fractional shortening (FS).

Tissue Preparation and Immunohistochemistry

The immunostaining of in vitro cell culture are as follows. CD31 and VE-cadherin were detected using mouse anti-human antibodies (eBioscience, San Diego, CA, USA and BD Pharmingen) diluted 1:100 and 1:50, respectively. Alexa Fluor 488 goat anti-mouse secondary antibody (Invitrogen) diluted 1:600 was used for final detection and visualization. For hESC-SMCs, we examined expression of α-smooth muscle actin using mouse anti-α-SMC actin Cy 3-conjugated antibody (Sigma). SM22 was detected with primary goat anti-human SM22 (Abcam, Cambridge, MA, USA) followed by visualization of species matched secondary antibody labeled with Alexa Fluor 488. ProlongGold + Dapi (Invitrogen) was utilized for slide preparation and nuclear visualization via fluorescent microscopy.

Following the 4-week echocardiogram, mice were sacrificed and the hearts excised. Hearts were then washed with PBS and dissected along the ventricular

septal wall. Samples were laid flat and embedded in Tissue-TEK OCT compound (Sakura Finetek, Zoeterwoude, The Netherlands). Using cryostat sectioning, 7 sections were cut for immunostaining purposes as previously described [39].

2.2.3 In vivo Swine Studies

Swine Model of Myocardial Ischemia/Reperfusion Model

Details of the animal model of postinfarction LV remodeling secondary to myocardial ischemia/reperfusion have been described previously [30, 59]. Briefly, young Yorkshire female swine (~20kg; Manthei Hog Farm, Elk River, MN) were anesthetized with pentobarbital (30 mg/kg, iv), intubated, and ventilated with a respirator with supplemental oxygen. A left thoracotomy was performed. The root of 1st diagonal coronary artery from left anterior descending coronary artery (LAD) was ligated for 60 min followed by reperfusion to create MI, which resulted in 10% LV mass damage. Other drugs administrated during open-chest surgery include Lidocaine (2 mg/kg iv bolus before ligation followed by 1 mg/(kg·min) iv for 70 minutes) and nitroglycerine (0.5 g/(kg·min) iv for 70 minutes starting 10 minutes before ligation). If ventricular fibrillation occurred, electrical defibrillation was performed immediately. Fifteen minutes after reperfusion, surviving pigs were randomized to ligation only (MI, n=5), open fibrin patch transplantation (MI+P, n=5) and cell seeded fibrin patch transplantation (MI+P+C, n=6) groups. The chest was then closed. Animals received standard post-operative care including analgesia until they ate normally and became active.

Fibrin Patch-based Stem Cell Transplantation

A fibrin patch was employed as the vehicle to deliver stem cell as described previously in detail [30]. Briefly, a fibrin biomatrix gel was formed by combining fibrinogen solution with thrombin solution. Without being bound by a particular mechanism, fibrinogen was converted to fibrin through a proteolytic reaction catalyzed by thrombin. Fibrin monomers then aggregated to form a flexible biomatrix. In this study, a fibrinogen solution (25 mg/mL) and a thrombin solution (75 NIH units/mL) supplemented with 4 mM $CaCl_2$ and 2 mM ε-aminocaproic acid (εACA) were mixed with equal volume (1 mL each) to form the fibrin patch (Approximately 2 cm in diameter and 5 mm in thickness). For cell transplantation, about 2×10^6 each of hESC-derived ECs and SMCs were pre-suspended in fibrinogen solution and then applied to the ischemic region together with thrombin solution. Typically, the biomatrix reaches a gel-like state within 30 sec as measured by curve of turbidity change [162]. The addition of εACA, an inhibitor of fibrinolysis, is to prolong the durability of fibrin patch in vivo [163]. Flexibility of fibrin patch can be also altered by changing the fibrinogen, thrombin and $CaCl_2$ concentration, whereas its biodegradability can be modified by adding fibrinolytic inhibitors (tranexamic acid at 9.2% w/v, or aprotinin at 3000 KIU/ml, where KIU is kallikrein IU) or anticoagulants. All components used for fibrin patch were purchased from Sigma-Aldrich (St. Louis, MO).

Immunosuppression

All pigs received clinical protocol of immunosuppression for xeno-transplantation with Cyclosporine 30 mg/kg per day with food as previously

described in details [60].

MRI Methods

MRI was performed on a 1.5 Tesla clinical scanner (Siemens Sontata, Siemens Medical Systems, Islen NJ) using a phased-array 4-channel surface coil and ECG gating as previously described in details [105]. MRI scans (before, 1 week after and 4 weeks after MI) were performed on a 1.5 Tesla clinical scanner (Siemens Sontata, Siemens Medical Systems, Islen, NJ) using a phased-array 4-4-channel surface coil and ECG gating as previously described [59, 60]. Animals were anesthetized with 1% isoflurane and positioned in a supine position within the scanner. The protocol consisted of: 1) localizing scouts to identify the long- and short-axis of the heart, 2) short- and long-axis cine (Steady-state free precession "True-FISP" sequence) for the measurement of global cardiac and 3) delayed contrast- enhancement imaging (turboFLASH sequence) for the assessment of scar size. Steady-state free precession "True-FISP" cine imaging used the following MR parameters: TR = 3.1 ms, TE = 1.6 ms, flip angle = 79^{o}, matrix size = 256 x 120, field of view = 340 mm x 265 mm, slice thickness = 6 (4 mm gap between slices) and 16-20 phases were acquired across the cardiac cycle. Global function and regional wall thickness data were computed from the short-axis cine images using MASS (Medis Medical Imaging Systems, Leiden, The Netherlands) for the manual segmentation of the endocardial and epicardial surfaces at both end-diastole (ED) and end-systole (ED) from base to apex. Short-axis turboFLASH imaging, from base to apex, used TR = 16 ms, TE = 4 TI ~ 220 ms, flip angle = 30^{o}, matrix size = 256 x 148, field of view = 320 mm x

185 mm, slice thickness = 6 mm (0 mm gap between slices) and two signal averages. The appropriate inversion time (TI) was chosen to adequately null the signal intensity (SI) of normal myocardium. Infarct size was calculated from the delayed contrast-enhanced images using MASS to manually segment regions of non-viable tissue. Infarct size was calculated as the ratio of the total scar area to the total LV area.

Tissue Preparation and Immunohistochemistry

After the MRI experiments were completed, the animals were anesthetized, the thoracotomy incision was reopened. Hemodynamics was measured. The heart was then explanted. The LV was sectioned in a bread-loaf manner into 6 transverse sections (1 cm in thickness) from apex to base. Even rings were subdivided into 12 circumferential specimens and fixed in zinc fixative (Anatech Ltd, Battle Creek, Mich). Detailed immunohistochemistry methods have been described previously [58, 59]. Briefly, tissues (~0.5 cm^3) were embedded in Tissue-Tissue-Tek OCT compound (Sakura Finetek, Zoeterwoude, The Netherlands) then subject to cryostat sectioning (10 μm in thickness). Immunofluorescence staining was employed to evaluate myocyte and transplanted cells. GFP expression was detected using goat anti-GFP primary antibody (abcam, 1: 20 dilution) followed by visualization of Donkey anti-goat IgG conjugated with FITC (Jackson ImmunoResearch, 1:50 dilution). Endothelial marker vWF and cardiac marker Troponin T were detected using mouse anti-vWF (abcam, 1:50 dilution) and mouse anti-cTnT (Thermo Scientific, 1:50 dilution) antibodies followed by visualization of Alexa Fluor 568-conjugated secondary antibody (Invitrogen,

dilution). Detailed immunohistochemistry methods have been described previously [39, 58].

Analysis of Myocardial Vascular Density

Vascular density was assessed using the methods as previously described in details [59]. Briefly, vascular density was assessed by staining with mouse monoclonal anti-Von Willebrand Factor (vWF, abcam, Cambridge, MA) antibody as previously described [58, 59]. The sections were visualized by fluorophore-conjugated secondary antibody (Molecular Probes, Inc, Eugene, Ore). Nuclear counterstaining by 4',6'-diamino-2-phenylindole (DAPI, Molecular Probes, Grand Island, NY) was also performed to serve as a control for total cell density. Images were taken at a magnification of 10X with an EVOS fl microscope (AMG, Mill Creek, WA). Capillary density was calculated as the fraction of vWF positive area per each high power field. 5 images were taken in a blind fashion per each section (10 μm in thickness), a total of 5 sections per each tissue area (infarct zone (IZ), border zone (BZ) and remote zone (RZ)) were analyzed for each animal group (n=2). Automatic analysis was performed with the aid of ImageJ software (NIH, http://rsb.info.nih.gov/ij) and checked against manual counting.

2.2.4 Statistics and Data Analysis

The repeated measures ANOVA was applied to compare the measurements systolic thickening fraction, ejection fraction and scar size across treatment groups and different time points (before MI, 1 week, and 4 weeks after MI). The significance level of type I error ($p < 0.05$) was used. The Bonferroni correction

the significance level was used to take into account multiple comparisons [164]. All values are expressed as mean ± standard deviation (SD). All statistical analyses were performed in Sigmastat version 3.5 (San Jose, CA).

2.3 Results

2.3.1 Endothelial and Smooth Muscle Cells Derived from Human Embryonic Stem Cells

As previously demonstrated, hESCs co-cultured with stromal cells gave rise to a population of $CD34^+CD31^+$ cells [165]. These hESC-derived $CD34^+CD31^+$ cells function as vascular progenitor cells that can be placed into secondary culture systems to produce homogeneous populations of endothelial and smooth muscle cell types (hESC-ECs and hESC-SMCs), respectively [158]. Here, we derived hESC-ECs and hESC-SMCs from the H9 hESC line that has stable expression of GFP and luciferase (GFP/Luc). These hESC-ECs exhibit classic endothelial cell morphology, express endothelial surface markers, and form capillary structures on Matrigel (Figure 2.1A). hESC-SMCs also assumed appropriate morphology, expressed intracellular smooth muscle cell markers, and lacked expression of endothelial surface marker CD31 (Figure 2.1B).

The in vitro HL-1 myocytes co-culture experiments (Figure 2.2) demonstrated the anti-apoptosis capability of the hESC-ECs.

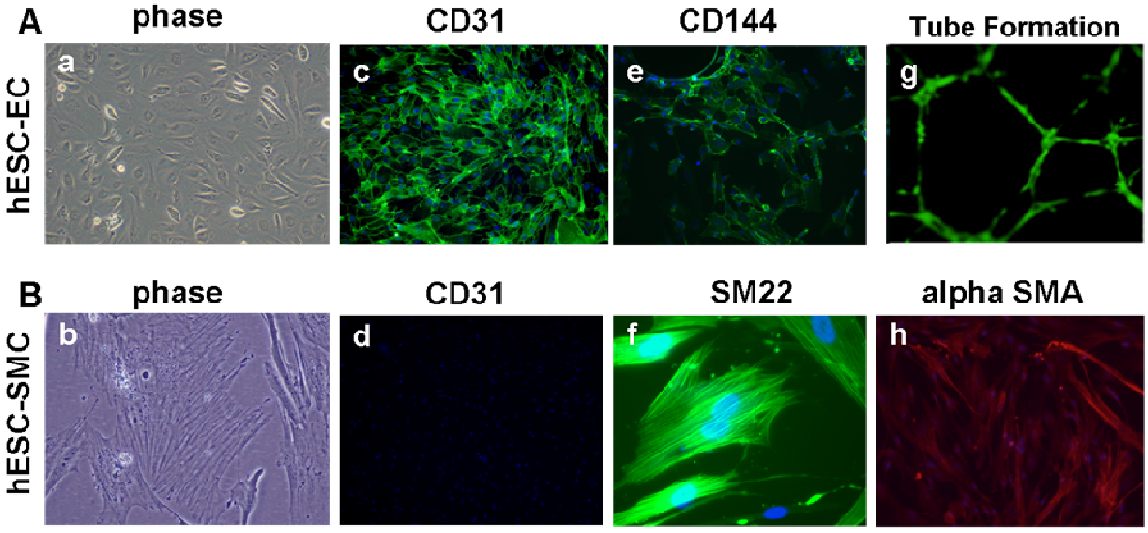

Figure 2.1 Endothelial and smooth muscle cells derived from human embryonic stem cells. Using GFP/Luc expressing H9 human embryonic stem cells, distinct populations of endothelial and smooth muscle cells were derived from a common $CD34^{+}CD31^{+}$ vascular progenitor cell population. Panel A (left to right) hESC-ECs showed classic cobblestone morphology, expressed CD31 (PECAM), CD144 (VE-Cadherin), and formed capillary structures on Matrigel. Original magnification: 40x. Panel B (left to right) hESC-SMCs assumed appropriate filamentous morphology, lacked expression of endothelial marker CD31, and expressed smooth muscle makers SM22 and alpha-smooth muscle actin (alpha SMA). Original magnification: 40x (alpha-smooth muscle actin, CD31) and 80x (phase, SM22). Panel a-f and h were acquired from GFP^{-} cells to avoid overlapping of immunofluorescence (Alexa Fluor 488) and GFP expression.

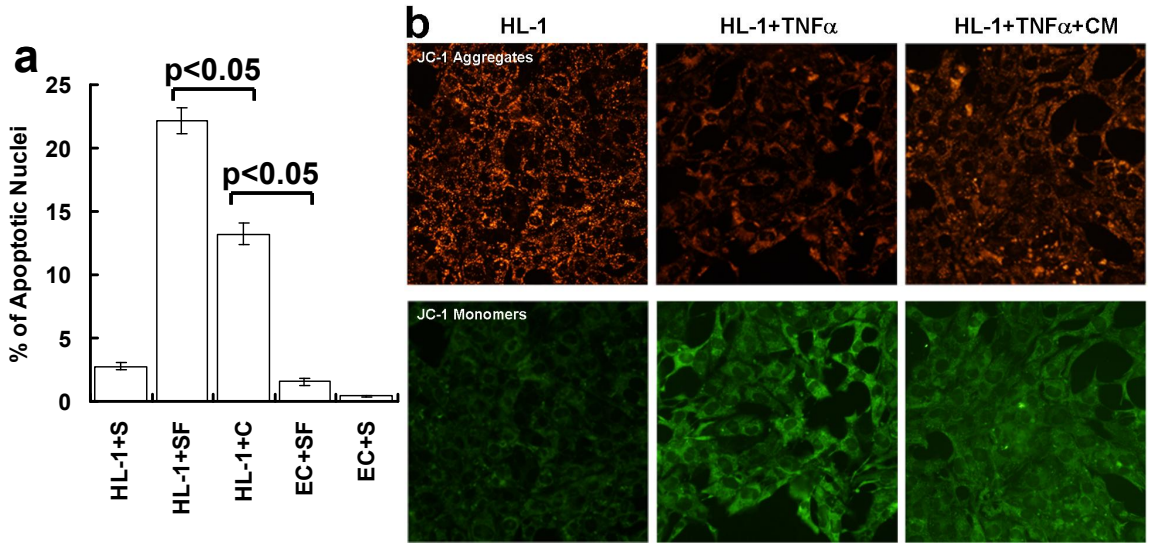

Figure 2.2 Anti-apoptotic capability of hESC-ECs. Panel a, reduced apoptosis of HL-1 cells by co-cultured in conditioned medium secreted from hESC-ECs. Panel b, alleviation of mitochondria disruption of HL-1 cells by co-culture with hESC-EC secreted conditioned medium.

2.3.2 Significant Improvement of Cardiac Function and Cell Engraftment in Infarcted Mouse Hearts Treated with hESC-ECs and hESC-SMCs

We have previously demonstrated interaction between hESC-ECs and hESC-hESC-SMCs in vitro [158]. Data from present study demonstrated these cell populations significantly improved LV chamber function and regional myocardial contractile performance in vivo while transplantation of hESC-ECs alone showed moderate improvement when compared to hearts that did not receive a cellular treatment and exposed to an identical LAD ligation protocol (Figure 2.3a-b). the hESC-derived cells maintained stable Luc expression, we were able to use bioluminescent imaging (BLI) to demonstrate persistence of the hESC-derived cells up to 8 weeks post-treatment (Figure 2.3c-e). BLI illustrated persistence of

luminescent signal, indicating engraftment of human cells, in hearts that received hESC-EC injections and co-injections of hESC-ECs and hESC-SMCs (Figure 2.3c). Measurable signal from engrafted cells in the left ventricle was detected throughout the course of the 4 week study and in excised hearts (Figure 2.3e). Some animals receiving both hESC-ECs and hESC-SMCs were assessed for luciferase signal beyond the 4 week study. Remarkably, the luminescent signal actually increases at later time points (8 weeks), demonstrating stable engraftment and expansion of these cells (Figure 2.3d). Additional immunohistochemical studies demonstrated development of GFP^+ vascular cells at 4 weeks post transplant, again demonstrating survival and function of these hESC-derived cells in hearts with postinfarction LV remodeling (Figure 2.3f).

Because of the significant difference in heart rate between mouse and human (600 beats compared to 70 beats per minute), and the arrhythmia concerns that associated with the human cells engraftment in the mouse heart, we combined these novel cell types derived from hESC in a 3D porous biodegradable fibrin patch to a clinical relevant pig model of ischemia-reperfusion and post-infarction LV remodeling. To assess the therapeutic potential of the cellularized patch, we examined LV chamber and regional myocardial contractile function, LV wall thickness and systolic wall stresses, scar size and chamber function.

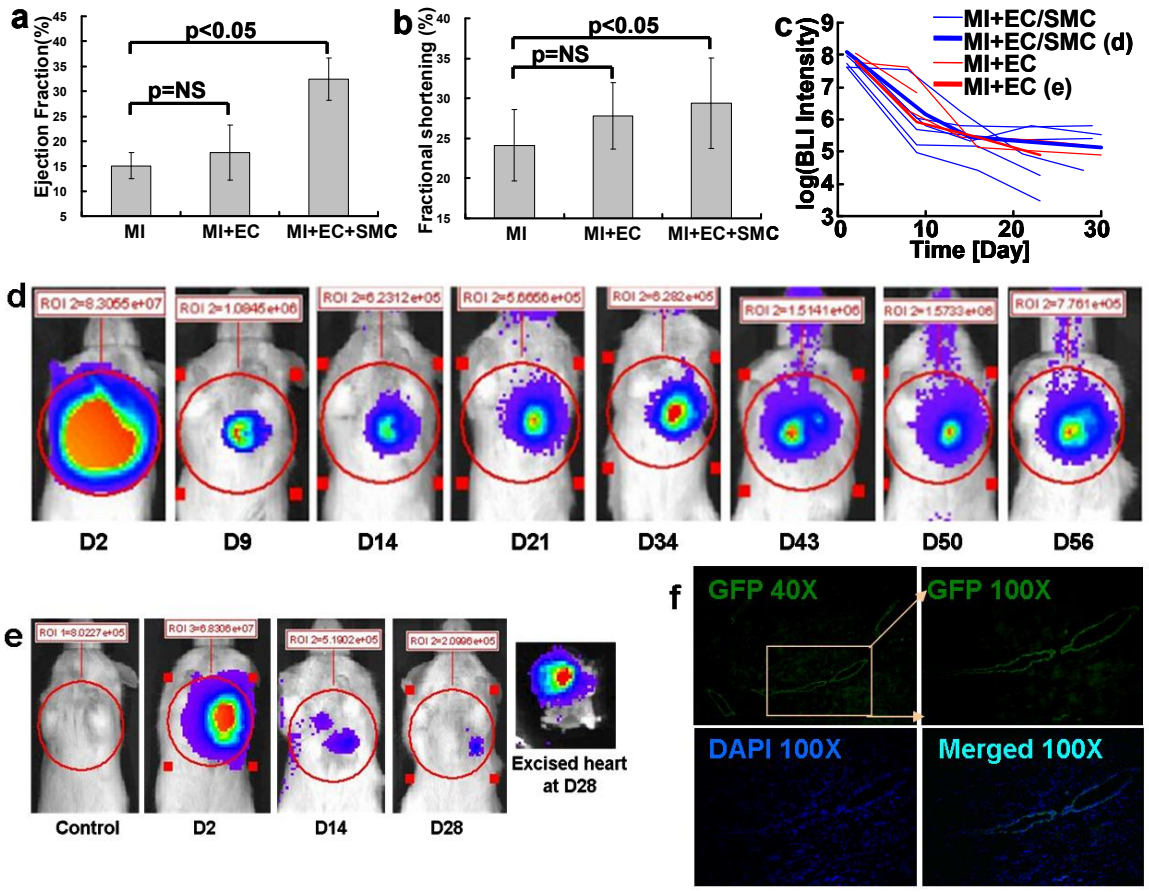

Figure 2.3 Significant improvement of cardiac function and cell engraftment in infarcted mouse hearts treated with hESC-ECs and SMCs. Cell therapy was delivered to the ischemic region of the LV after LAD coronary artery ligation. Ejection fraction (panel a) and shortening fraction (panel b) were measured 4 weeks post-infarction in mice receiving no injection (MI), 10^6 hESC-ECs (MI+EC), and $5x10^5$ each hESC-EC and SMC (MI+EC+SMC). Significant improvement in LV function was achieved in mice that received combined cellular therapy ($p<0.05$). Transplanted GFP/Luc cells were tracked in vivo via bioluminescent imaging (BLI, panel d-e) and cell engraftment was confirmed post mortem by immunofluorescent staining against GFP (panel f). Panel d, quantification of luciferase signal from mouse hearts receiving cellular injection throughout the course of the experiment. The BLI intensity curves corresponding to panel d and e are highlighted in bold.

2.3.3 Swine Studies

Anatomic Data

Cell transplantation resulted in a significant decrease in left ventricular hypertrophy as reflected by a decrease in LVW/BW (Figure 2.4a, $p<0.05$) in the cell treated hearts as compared to the hearts in both of the control groups. The myocardial infarct size data measured by MRI are illustrated in Figure 2.4b. At week 1 post LAD ligation the infarct size was about 9 percent of total LV, and was not significantly different among the 3 groups (p=NS). However, at week 4 the infarct size was significantly smaller in cell treated group than the MI group ($p<0.05$).

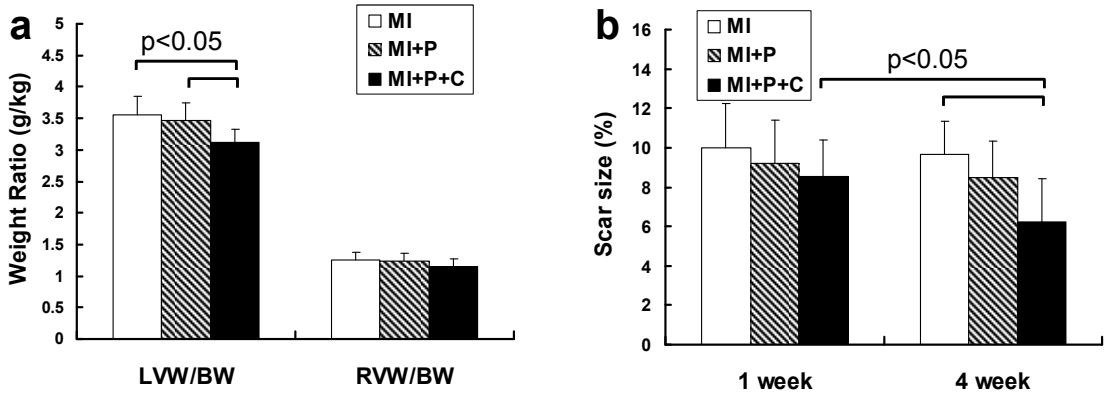

Figure 2.4 Anatomic data of swine studies. Panel a, heart weight to body weight ratio (g/kg) at 4 weeks after MI. Panel b, scar size as measured by delayed contrast-enhanced cardiac MRI at 1 week and 4 weeks after MI.

Myocyte hypertrophy in border zone is examined by histological sections (H & E staining, Figure 2.5a-c) of the harvested hearts. The stem cell transplantation resulted in a decreased myocyte cross section area (Figure 2.5d) and an increased nuclei density (Figure 2.5d) as compared to the other two groups (MI

and MI+P). Taken together, the stem cell transplantation alleviated the LV hypertrophy secondary to ischemia damage.

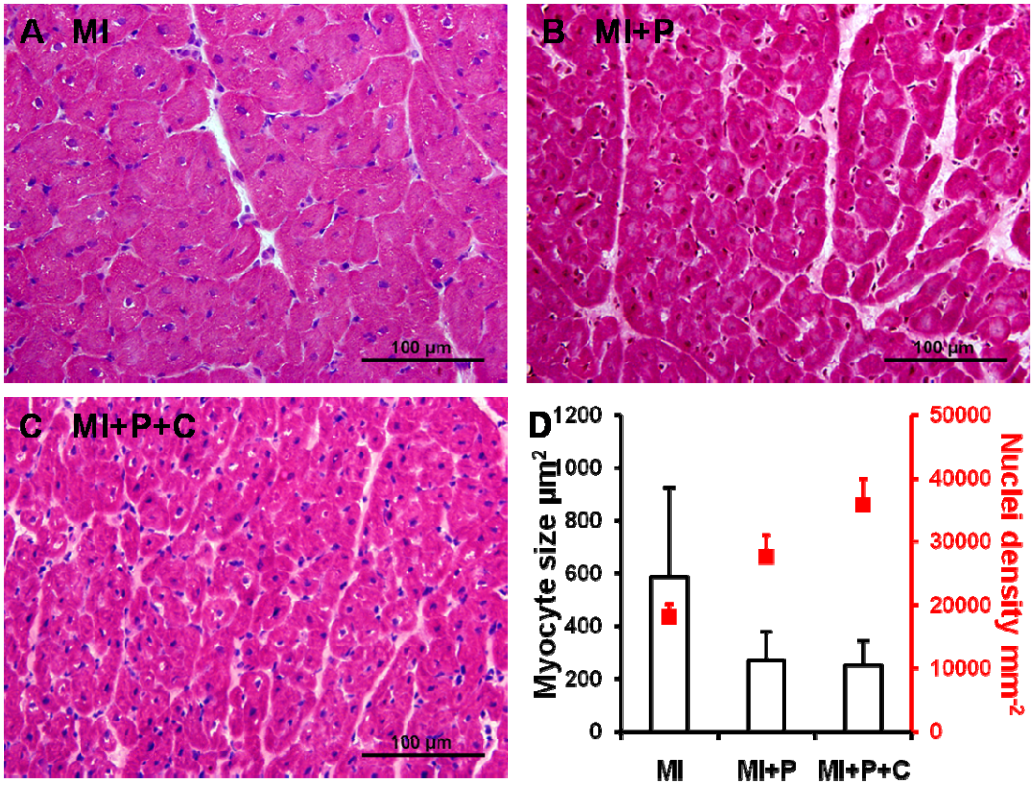

Figure 2.5 Stem cell transplantation alleviated LV hypertrophy. Panel a-c, representative H&E staining of the histological sections from the border zone heart tissues. Panel d, quantification of the staining images for myocyte size and nuclei density.

LV Contractile Functional Data

The temporal changes in ejection fraction (EF) as measured by MRI are illustrated in Figure 2.6a. There was no significant difference among the 3 groups at baseline. However, the fibrin patch-based cell transplantation showed a significant improvement in ejection fraction, which was seen as early as 7 days (MI+P+C (45.2±3.1) vs MI (39.2±3.0), $p<0.05$). The beneficial effect in LV chamber function persisted up to 4 weeks (Figure 2.6a, $p<0.05$). Similarly, the

regional LV systolic thickening fraction in the infarct zone was also significantly improved in cell treated group compared to the other two control groups (Figure 2.6b, $p<0.05$). In addition, the cell treatment resulted in reduction of the left ventricular thinning in the infarct zone seen at 4 weeks after MI, as depicted by significantly lower across the LV wall thickness in the saline treated- or open treated- groups (Figure 2.7a, $p<0.05$). This increased LV wall thickness in the infarct zone was accompanied by a significant lower systolic LV wall stresses as compared to MI control group (Figure 2.7b, $p<0.05$).

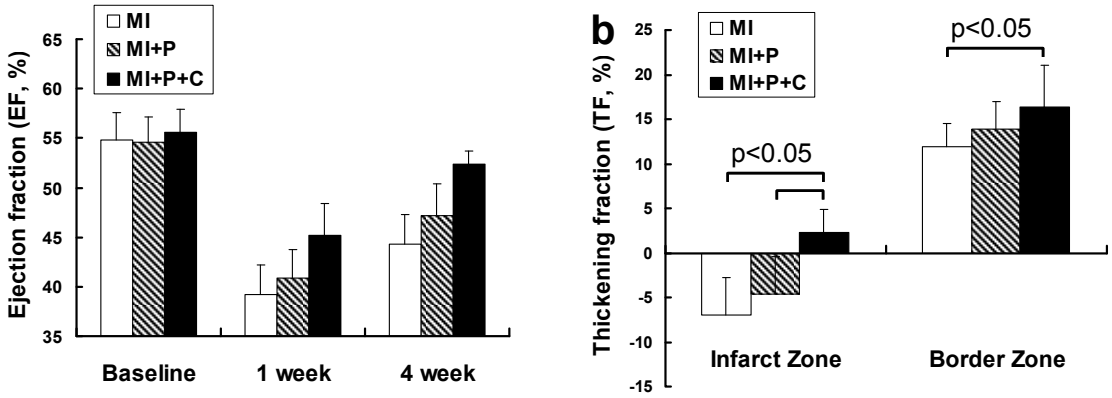

Figure 2.6 Improvement of LV contractile function upon stem cell transplantation. Temporal changes of LV contractile function in terms of ejection fraction (EF, panel a) and thickening fraction (TF, panel b) are measured by cardiac cine magnetic resonance imaging.

Vascular Density

To determine the mechanisms underlying the beneficial effects of cell transplantation, we investigated the effects of cell transplantation on neovascularization and angiogenesis in the post-MI hearts. At 4 weeks after cell transplantation, immunofluorescence staining for vWF indicated significant angiogenesis in stem cell treated hearts, with more vWF expressing capillaries

being present in both infarct and peri-infarct regions of cell treated compared with the other two groups (Figure 2.8a). Quantitative evaluation of vWF-positive capillary fractional area per high-power field (20x) indicated that vascular density was significantly greater in the cell treated group than the control groups of saline-treated and open patch-treated hearts (Figure 2.8b). In the peri-infarct region of cell transplanted hearts, double vWF^{+}/GFP^{+} cells were observed via co-co-staining of vWF and GFP, however, few cells were stained positive for both myocyte marker TnT or MHC, and GFP (data not shown). These data suggested that transplanted hESC-derived cells may rescue ischemia threatened myocytes from apoptosis, promote angiogenesis through a paracrine effect.

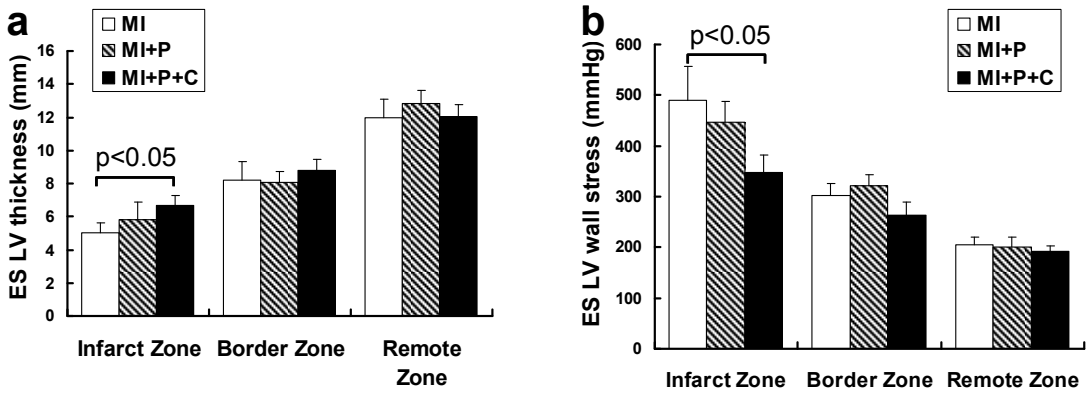

Figure 2.7 Alleviation of LV wall stress by increased LV thickness from stem cell transplantation. Panel a, end-systolic LV wall thickness at 4 weeks after MI. Panel b, end-systolic LV wall stress at 4 weeks after MI.

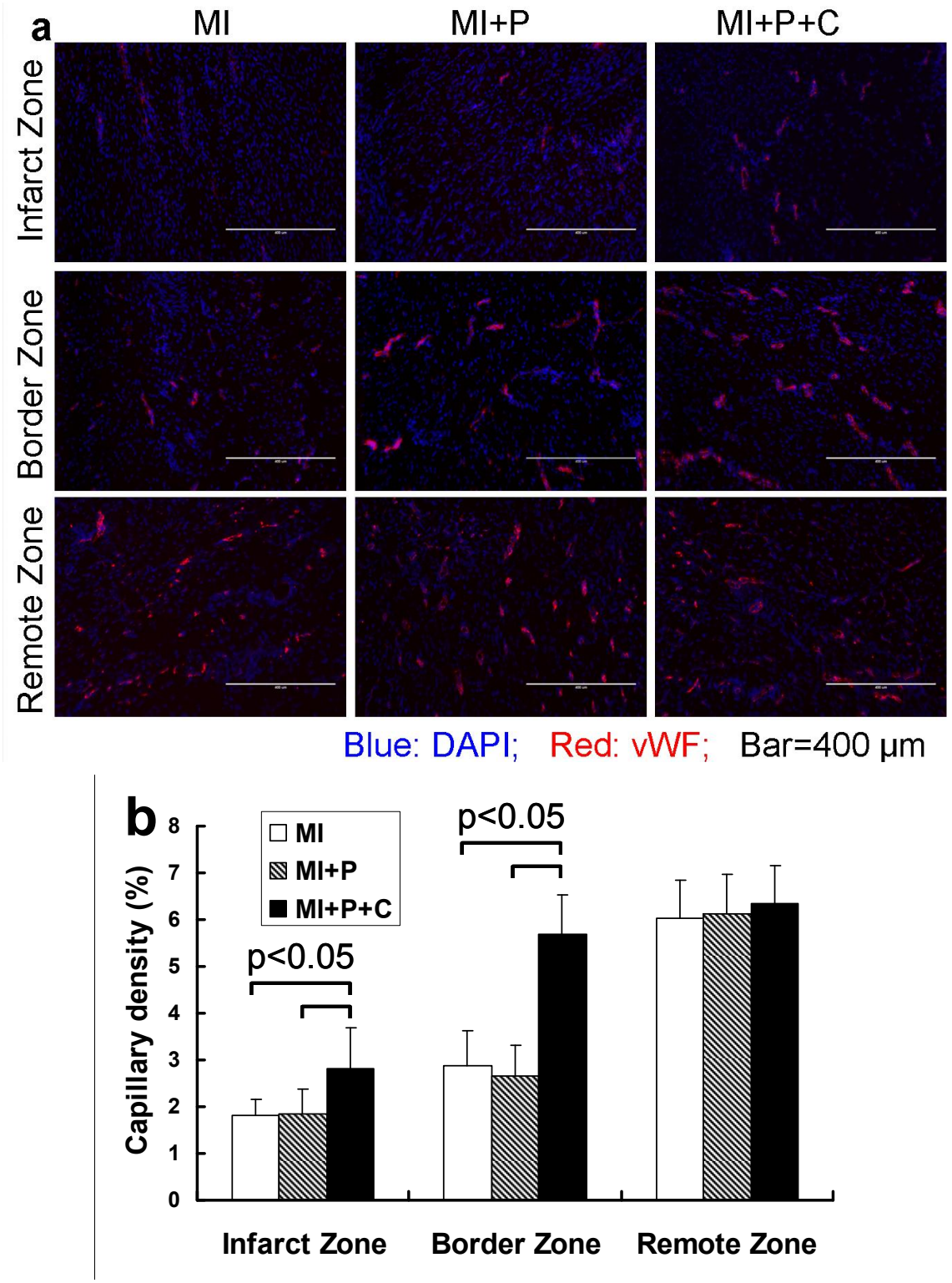

Figure 2.8 Increased capillary density from stem cell transplantation. Panel a, immuno-fluorescent staining of vWF at 4 weeks after MI. Panel b, quantification of vWF-positive capillary density.

Cell Engraftment

There was significant engraftment of hESC-derived endothelial cells and smooth muscle cells observed at 4 weeks after transplantation in the cell treated animals of both mouse (4 weeks, Figure 2.3c-e) and swine (day 9, 16 and 27, Figure 2.9) model of postinfarction LV remodeling as confirmed by in vivo and ex vivo BLI.

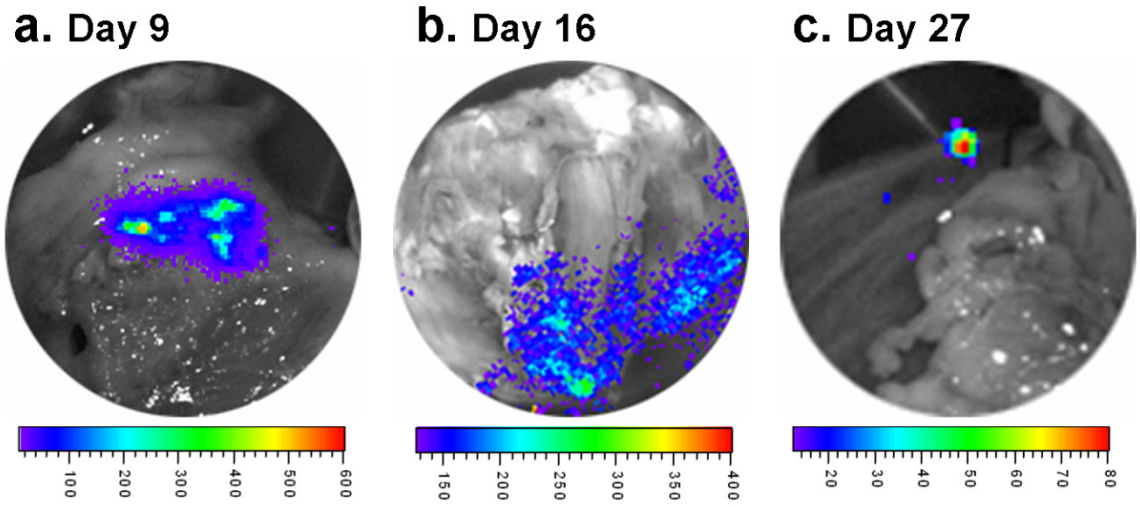

Figure 2.9 Substantial cell engraftment. Ex vivo bioluminescent imaging of excised pig hearts showed substantial cell engraftment at Day 9 (panel a), 16 (panel b) and 27 (panel c) after MI.

The substantial cell engraftment on swine hearts was also supported by ex vivo tissue culture (Figure 2.10). Approximately 1 gram of heart tissue underneath the patch area was used for ex vivo tissue culture (Day 16 post cell transplantation). GFP^+ cells were detected upon 24 hr culture, and they were actively proliferating as evidenced by increased GFP^+ cells number upon 72 hr culture.

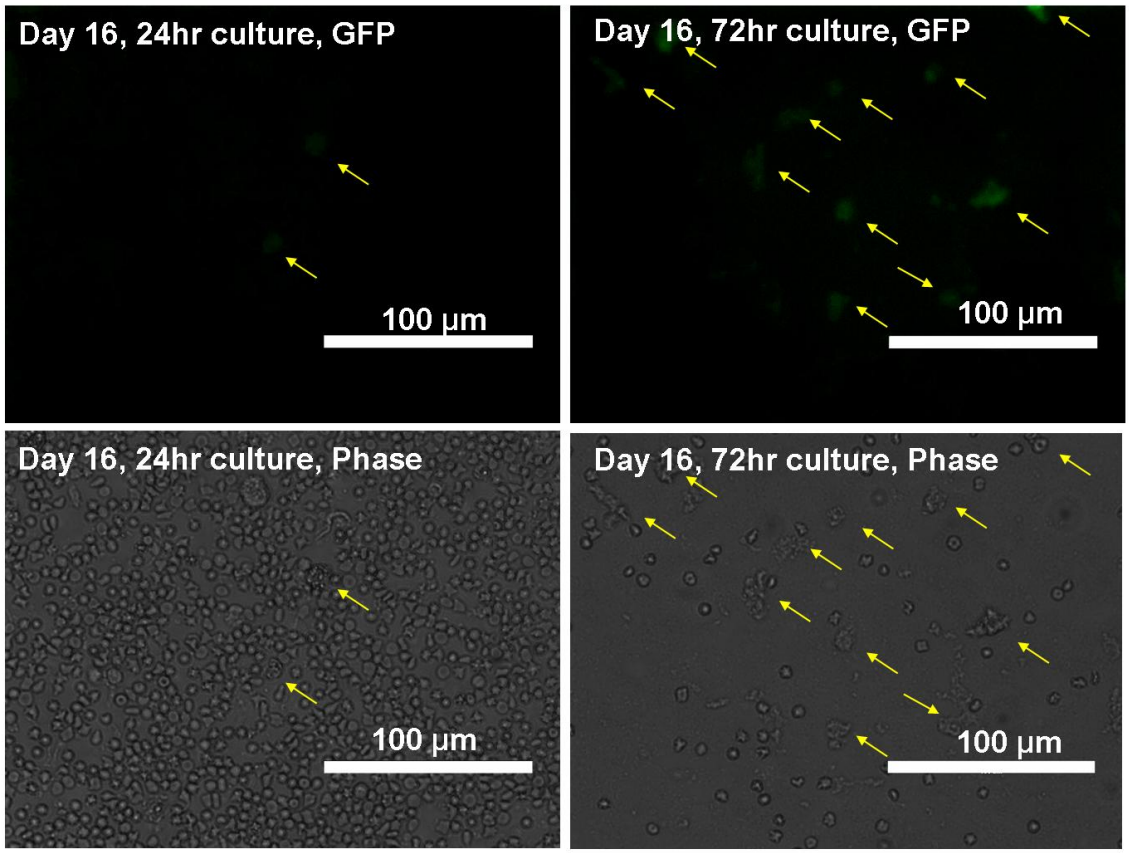

Figure 2.10 GFP$^+$ cells migrating out of excised pig heart at Day 16 post treatment. The ex vivo tissue culture was performed at Day 16 post cell transplantation. Approximately 1 gram of heart tissue underlying the patch area was minced (~1 mm size), cultured in fibronectin coated T75 flasks and examined for GFP$^+$ cells at 24 hr and 72 hr. Much more GFP$^+$ cells were observed at 72 hr, indicating active proliferation of the transplanted cells. The engraftment rate on Day 16 post transplantation is 3~10% based on the number of GFP$^+$ cells observed on 24 hr and 72 hr incubation.

The successful cell engraftment was also confirmed by immunohistochemistry staining of GFP and/or vWF on explanted pig heart tissue at Day 9 and Week 4 post cell transplantation, as shown in Figure 2.11. The co-staining of GFP and vWF (lower left panel) indicated that the transplanted vascular progenitor cells started to engraft into host vessel as early as Day 9 and persisted up to week 4 post transplantation (upper right panel). The vessel was not uniformly positive for

GFP staining, excluding the possibility of autofluorescence or non-specific A phase contrast image was also included (lower right panel) to demonstrate absence of tissue folding, a potential cause of false positive GFP staining.

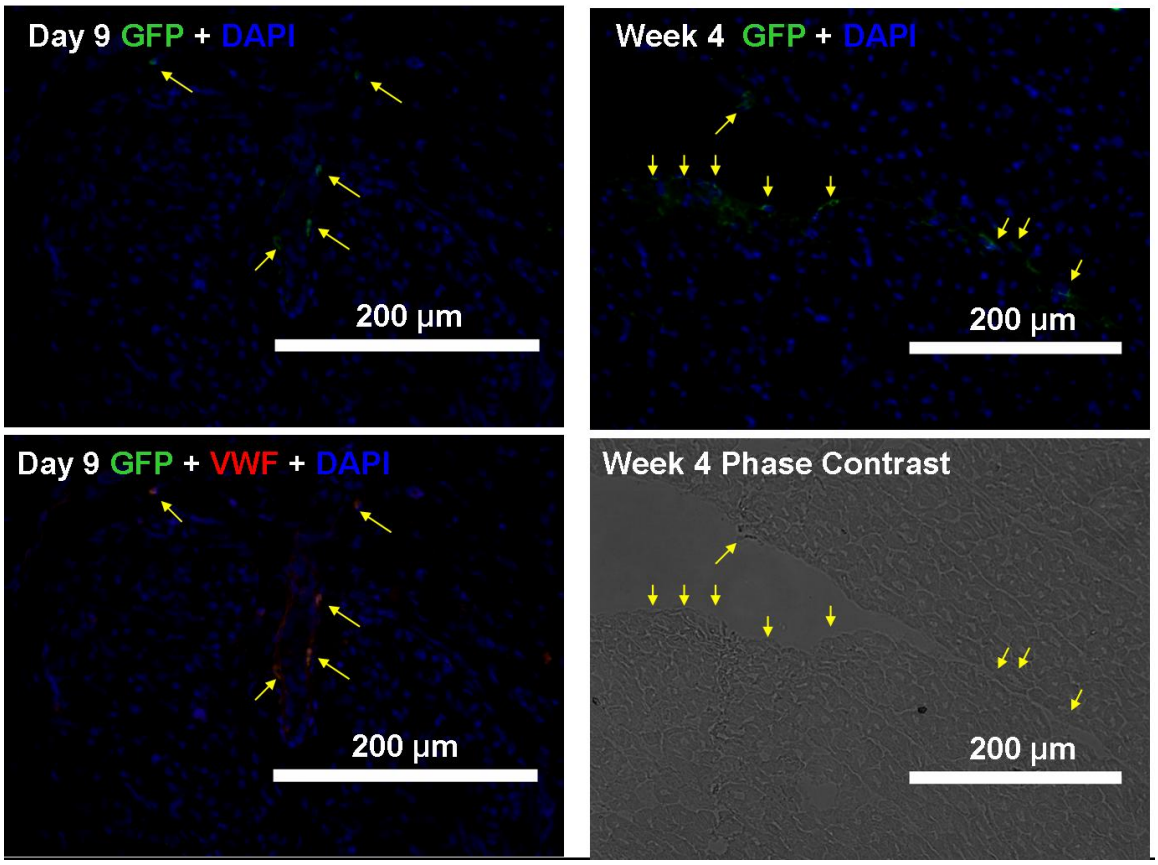

Figure 2.11 Immunostaining of the transplanted stem cells. GFP (green) and/or vWF (red) staining was performed on histological sections from peri-infarct region of the explanted pig hearts at Day 9 (left) and 27 (right) post MI.

2.4 Discussion

The present study demonstrates that a fibrin patch-based hESC-derived vascular cell transplantation leads to functional improvement in a clinically relevant porcine model of postinfarction LV remodeling. Stem cell transplantation resulted in an overall improved LV function and LV remodeling following MI with an amelioration of LV scar thinning. This was associated with a reduction in scar size at 4 weeks. Cell transplantation also resulted in a significant increase of neovascularization in both infarct and peri-infarct regions. These data demonstrate that using a novel 3D porous fibrin patch-enhanced delivery, the transplantation of the equal mixture of endothelial cell and smooth muscle cells derived from the hESCs can promote the myocardial neovascularization of the recipient heart, reduce the ischemic injured myocytes from apoptosis, and improve the LV contractile function. The findings suggest a promising therapeutic potential of using this cell type and mode of delivery.

2.4.1 Translational Potential of hES-derived Endothelial and Smooth Muscle Cells

hESCs have been used to derive diverse cardio-vascular cell populations [18]. RT-PCR and immunohistochemical studies demonstrate that hESC-derived cardiomyocytes (hESC-CMs) express early cardiac specific transcription factors, sarcomeric proteins and gap junction proteins [20]. Although, electrophysiologic studies showed that most of the hESC-CMs resemble human fetal ventricular myocytes capable of propagating action potentials [166], a recent study suggested

that transplantation of hESC-CMs with serum free medium to hearts with injuries resulted in a very low engraftment rate [20]. On the other hand, there are reports demonstrating that beneficial effects of LV chamber function in response to the bone marrow derived progenitors transplantation therapy, is associated with the increased neovascularization [30, 39, 58, 60]. Consequently, the present study was carried out to examine whether hESC derived cardiac vascular cells can be utilized to prevent LV dysfunction and postinfarction LV remodeling in hearts suffering from acute myocardial infarction. The data from the present study demonstrate that these cell types can promote the myocardial neovascularization of the recipient heart (Figure 2.8), which in turn, reduce the ischemic injured myocyte from apoptosis, and improve the LV chamber function.

2.4.2 Engraftment of hESC-derived Cells

Using the novel fibrin patch-enhanced delivery, data from both the mouse model and pig model demonstrated significant cell engraftment a few weeks after the transplantation, which was accompanied by the functional and bioenergetic improvement. Recently, there are reports suggesting that less than 50% of the cells remained in the myocardium a few hours after the transplantation, which was caused by the pulsate intramyocardial pressure changes during the continuous cardiac cycle [68]. These data suggest that a significant fraction of the acute loss of delivered cells is caused by the active contraction of the LV, but is independent from the apoptosis or necrosis.

In the present study, the BLI data from both rodent and swine studies demonstrate the persistence of hESC-derived cells (Figure 2.3 and 2.9), which is

in agreement with our earlier reports that applying this 3D porous biomaterials in stem cell delivery for myocardial repair is accompanied by further increase of cell engraftment rate, reduction in apoptosis in ischemia threatened myocytes, decrease of peri-infarct area fibrosis and prevention of LV scar systolic bulging [30]. The reduced LV dilatation and LV scar bulging, in turn, result in significantly reduced myocardial wall stress and improved myocardial bioenergetics.

This fibrin 3D porous biomatrix is useful for several reasons. First, it is tightly patched on the surface of injured myocardium that had exposed to ischemia reperfusion. Therefore, the active myocardial contraction will not squeeze the out of the site of the delivery. Second, there are ample fibrinogen and thrombin proteins in the circulation that can be used for the patch biomaterial. In principle, both components can be autologous. In the present study, we try to use the autologous thrombin by scraping the surface of myocardial patch area, which effectively make the patch tightly stick on the surface at 4 weeks post transplantation. The scraping channels may also serve as routes for the stem get into the myocardium. Third, the fibrin patch can be chemically modified to any peptides such as HGF or SDF-1α, creating a progenitor cell friendly environment for the purposes such as enhancing the engraftment or controlled differentiation [30, 100, 156, 157]. Fourth, we have previously demonstrated that the mesenchymal stem cell fibrin patch itself result in a remarkable increase of neovascularization into the patch material 4 weeks after the transplantation [30, 100, 156, 157], which was accompanied by a significant increase of engraftment rate and improvement of systolic thickening fraction in the patched area of myocardium. In

the present study, we have found that this patch delivery is associated a engraftment rate (Figure 2.9). In some cases, the BLI signals indeed increased. Most importantly, the data from the present study demonstrate that both chamber function and regional systolic thickening fraction improved significantly (Figure 2.6).

2.4.3 Improvement in Ventricular Function and Reduction in Regional Wall Stress

The present study demonstrates that transplantation of hESC-derived vascular cells leads to improvement in ventricular function in a large animal model. We have previously reported that LV bulging at infarct zone was accompanied by a significant increase of regional LV wall stress at IZ and peri-infarct BZ [154]. This particular increase of regional wall stresses and its associated severe bioenergetic abnormality were significantly ameliorated by the autologous MSC transplantation [30, 59, 60]. We reasoned that the decrease of LV bulging at LV scar area (Figure 2.6b) resulted in reduction of the regional wall stress (Figure 2.7b) and energy demand, which in turn, would otherwise cause severe bioenergetic abnormality [167]. In the present study, the engraftment of the hESC-derived vascular cells (Figure 2.9) was accompanied by increase of LV wall thickness and thickening fraction in the IZ and BZ, which in turn, resulted in a significant reduction of regional LV wall stresses (Figure 2.7b). By necessity, these improvements will result in the myocardial bioenergetics that has been observed using the same pig model of postinfarction LV remodeling.

During the 4 weeks follow up by cardiac MRI, we observed a significant reduction of infarct size (Figure 2.4b) that occurred only in the MI+P+C group. The LV dysfunction of failing hearts is associated with the oxidative stress caused by the excess of reactive oxygen species (ROS) production in the cytoplasm and the electron transport chain of mitochondria in myocytes [168]. Using a similar animal model and bone marrow derived progenitor cells, we also observed that cell transplantation associated improvement in myocardial contractile function was accompanied by reduction of several different subunits of the respiratory chain oxidative enzyme, which may in turn, result in the reduction of the oxidative stress, and consequently reduce the infarct size associated with apoptosis [59].

2.4.4 Effect of Immunosuppression

In the current pig study, cyclosporine A was administered for immunosuppression. This approach has been utilized previously in a similar pig study with bone marrow-derived multipotent progenitor cell transplantation [60]. In that study, there was no significant difference in the LV postinfarction remodeling between the cell treated hearts with and without cyclosporine A administration. From the same study, pigs (3 months of age) that received myocardial infarction and no cyclosporine A had an average body weight of 29±7 kg and a mean LV/BW ratio of 3.57±0.27. In the current study, pigs that received similar myocardial infarction and cyclosporine A had an average body weight of 35±3 kg at age 3.4 months, and mean LV/BW of 3.6±0.3. These data indicated that in the Cyclosporine A does not have an obvious influence on the LV remodeling myocardial infarction.

2.4.5 Effect of Cell Transplantation on Infarct Size

Sequential MRI functional assessment allowed us to conclude that the infarct size in swine treated with hESCs decreased from 1 week to 4 weeks interval, while the scar sizes in swine without hESC treatment was maintained throughout the follow-up (Figure 2.4b). This reduction in scar size with stem cell treatment has been seen previously in other reports [62, 169, 170]. The beneficial effects of cell transplantation could be related to the mobilization of endogenous cardiac progenitors to the injury site by paracrine effects as we and others have observed previously [62, 170]. As we did not observe significant myocytes transdifferentiation at 4 weeks, the functional and structural improvements of decrease of infarct size and improved vascular density, are likely secondary to paracrine effects that include sparing of native cardiomyocytes from apoptosis as we observed recently [171]. It was also observed recently that cell transplantation is accompanied by an up-regulation of MEF2A, the predominant MEF2 gene product expressed in postnatal cardiac muscle. MEFs play an important role in myogenesis [172]. We postulate that cell transplantation may cause an activation of endogenous cardiac progenitor cells [62, 173], and MEF2A may play a role in their differentiation into cardiomyocytes.

In summary, the present study demonstrates that a fibrin patch based transplantation of hESC-derived vascular cells (ECs and SMCs) leads to a significant engraftment of vascular cells derived from the hESCs that is accompanied by a significant increase of neovascularization and LV contractile functional improvement, which in turn, results in a significant reduction of regional

wall stress and infarct size. Taken together, these findings suggest a promising therapeutic potential of this combined approach using these vascular cell populations derived from hESC and the novel mode of delivery.

Chapter 3

NOVEL STRATEGY FOR MEASURING CREATINE KINASE REACTION RATE IN THE IN VIVO HEART

3.1 Introduction

Cardiac hypertrophy occurs as a compensatory response to various stressors including pressure overload, volume overload and myocardial infarction. After a prolonged period of compensatory hypertrophy with restored ventricular wall stress, severe ventricular dysfunction often occurs with signs of congestive heart failure (CHF). The exact mechanisms underlying this transition from ventricular hypertrophy to CHF are likely multi-factorial, but alterations in myocardial bioenergetics have been considered to be important factors in this pathway [174, 175]. The creatine kinase (CK) enzyme catalyzes the reaction that converts adenosine diphosphate (ADP) and phosphocreatine (PCr) to adenosine triphosphate (ATP) and creatine (Cr) [176]. This maintains high ADP levels in the

mitochondria where ATP is generated and low ADP levels at the contractile apparatus where ATP is utilized, thus facilitating the production and utilization of ATP [126, 177]. We have previously reported that the myocardial CK forward flux rate is significantly reduced in hypertrophied hearts [178-181]. The severity of this reduction is linearly related to the severity of the hypertrophy and left ventricular dysfunction [179]. Recently, using a low field 1.5 Tesla magnet, Dr. Weiss and associates examined heart failure patients and found that the CK flux was reduced in patients with left ventricular hypertrophy (LVH) and CHF [182, 183]. Importantly, the studies demonstrate that the severity of the reduction in CK flux rate is related to the severity of LV contractile dysfunction [182], and suggest that CK flux rate may be a more sensitive myocardial energetic indicator for the severity of LV dysfunction as compared to the PCr/ATP ratio in heart failure patients [183]. However, the quantitative assessment of CK forward flux rate at low field magnet may be limited by the low signal-to-noise ratio (SNR).

Transmurally differentiated measurements of ATP production rate via CK require longer data acquisition time for spatial localization. In a dog model, the CK flux rate was reported to be heterogeneous across the LV wall of normal heart with the lowest rate in inner layers of the LV wall [184]. These CK flux measurements with transmural differentiation took ~ 6 hours to complete the data acquisition for one experimental condition, suggesting unlikely to perform experimental interventions.

Here, we demonstrate a novel strategy for magnetization saturation transfer (MST) study of ATP production rate via CK forward reaction (k_f). By employing

numerically optimized pre-saturation delays, this strategy results in an 82% and a 56% reduction in total data acquisition time and saturation pulse duration, respectively. The novel strategy was validated using an fin vivo porcine heart model, which generated identical k_f values as compared to that measured with conventional approach from the same heart. The significant reductions in acquisition time as well as saturation pulse duration provided by this novel approach can potentially facilitate the future high field cardiac CK MST studies with spatial localization on patients with heart failure in high field magnet.

3.2 Methods

All experiments were performed in accordance with the animal use guidelines of the University of Minnesota, and the experimental protocol was approved by the University of Minnesota Research Animal Resources Committee. The investigation conformed to the *"Guide for the care and use of laboratory animals"* published by the National Institutes of Health (NIH publication No 85-23, revised 1985).

3.2.1 Open-chest Surgery Preparation for ^{31}P MR Spectroscopy

Details of the open-chest surgery preparation for ^{31}P MR spectroscopy (MRS) have been described previously [154, 185]. Briefly, young Yorkshire swine (~30 kg) were anesthetized with pentobarbital sodium (initial dose 30 mg/kg iv, maintenance dose 4 mg/(kg/h) iv), intubated and ventilated with supplemental oxygen on a respirator. Polyvinyl chloride catheters (3 mm OD) were inserted into

the ascending aorta, superior vena cava, and left ventricle for hemodynamic monitoring. The ascending aorta catheter was placed via the left internal carotid artery and the two intravenous catheters were placed through the left external jugular vein. The heart was exposed via a sternotomy and suspended in a pericardial cradle. The LV catheter was introduced through the apical dimple. Aortic and LV pressures were measured by pressure transducers positioned at mid-chest level and recorded on an eight-channel recorder. Ventilation rate, volume, and inspired oxygen content were adjusted to maintain physiological values for arterial PO_2, PCO_2, and pH. Aortic and LV pressures were continuously monitored throughout the study.

3.2.2 ^{31}P MR Spectroscopy

Measurements were performed in a 40 cm bore 4.7 T magnet interfaced with a SISCO (Spectroscopy Imaging Systems Corporation, Fremont, CA) console. ^{31}P and ^{1}H NMR frequencies were 81 and 200 MHz, respectively. Radiofrequency transmission and signal detection were performed with a 28 mm-diameter double tuned surface coil sutured directly to the epicardium of anterior LV wall. The coil was cemented to a sheet of silicone rubber 0.7 mm in thickness and approximately 20% larger in diameter than the coil itself. A containing 15 µl of 3 M phosphonoacetic acid was placed at the coil center to serve as a reference. The proton signal from water detected with the surface coil was used to homogenize the magnetic field and to adjust the position of the animal in the magnet so that the coil was at or near the magnetic isocenter. This

was accomplished using a spin-echo experiment and a readout gradient. The information gathered in this step was also utilized to determine the spatial coordinates for spectroscopic localization [111, 186]. Chemical shifts were measured relative to PCr, which was assigned a chemical shift of -2.55 ppm relative to 85% phosphoric acid at 0 ppm. Baseline myocardial high energy phosphate (HEP) data acquisition was achieved with a 90^{o} adiabatic half passage pulse and selective saturation on γ-adenosine triphosphate (ATPγ) was achieved with *B*1-*B*1-*i*nsentitive *tr*ain to *o*bliterate signal (BISTRO) as previously reported [187].

3.2.3 k_f Calculation of Conventional MST Methods

Table 3.1 summarizes all the abbreviations and symbols.

A conventional magnetization saturation transfer (MST) method consists of two experiments, namely, progressive and steady state saturations. The Creatine Kinase (CK) enzyme catalyzes the reaction $\mathrm{PCr} + \mathrm{ADP} + \mathrm{H}^{+} \underset{}{\overset{k_f}{\rightleftarrows}} \mathrm{Cr} + \mathrm{ATP}$ in which k_f is the forward pseudo-first-order rate constant.

The progressive saturation transfer experiment employs multiple data acquisitions with progressively prolonged saturation on ATPγ to retrieve the apparent relaxation time constant of PCr by fitting its signal intensity to the following equation [188]:

$$M_{\mathrm{PCr}}(t) = M_{0,\mathrm{PCr}}\left[T_{1,\mathrm{PCr}}^{\mathrm{app}} k_{\mathrm{f}} \exp\left(\frac{-t}{T_{1,\mathrm{PCr}}^{\mathrm{app}}}\right) + \frac{T_{1,\mathrm{PCr}}^{\mathrm{app}}}{T_{1,\mathrm{PCr}}^{\mathrm{int}}}\right] \qquad [3.1]$$

Table 3.1 Abbreviations and symbols

Abbreviation	Actual physical meaning
MST	Magnetization saturation transfer
MRS	Magnetic resonance spectroscopy
CK	Creatine kinase
d_1	The pre-saturation delay employed in the MST experiment.
d_2	The duration of saturation pulse in the MST experiment.
FID	Free induction decay,
k_f	Pseudo-first-order rate constant to characterize the ATP production rate via CK.
M_0	Magnetization measured by ^{31}P MRS under fully relaxed condition.
M_{short}	Magnetization measured with very short repetition time. This measurement in combination with M_0 can yield an approximate value of T_1^{int} according to equation [3.14].
M_{ss}	Steady state magnetization of a spin (e.g. PCr) when the counterpart spin (e.g. ATPγ) is continuously saturated, as dictated by equation [3.1].
$M_{TR,PCr}$	Magnetization measured with ATPγ continuously saturated. The TR can be arbitrary. This in combination with $M_{ss,PCr}$ can yield accurate value of $T_{1,PCr}^{app}$ according to equation [3.10]
nt	Number of averaged FIDs for one spectrum.
T_1^{app}	Apparent longitudinal relaxation time constant of a spin (e.g. PCr) when the counterpart spin (e.g. ATPγ) is continuously saturated, as dictated by equation [3.1].
T_1^{mix}	Apparent longitudinal relaxation time constant when chemical exchange is involved. T_1^{mix} is an approximation because the actual recovery of spin magnetization under chemical exchange is not an exact exponential curve.
TR	The repetition time of pulse sequence in MST experiment.

where $M_{0,PCr}$ is the thermal equilibrium signal intensity of PCr detected by MRS, $T_{1,PCr}^{int}$ is the intrinsic spin-lattice relaxation time of PCr . $T_{1,PCr}^{app}$ is the apparent relaxation time of PCr when ATPγ is continuously saturated and defined according to the following equation [188]:

$$T_{1,\mathrm{PCr}}^{\mathrm{app}\ -1} = T_{1,\mathrm{PCr}}^{\mathrm{int}\ -1} + k_{\mathrm{f}} \qquad [3.2]$$

The steady state saturation transfer experiment employs "infinitively long" saturation on ATPγ (usually 3 to 5 times of $T_{1,PCr}^{app}$) to find the steady state signal intensity of PCr ($M_{ss,PCr}$) and then the k_f can be calculated according to the following equation [188]:

$$k_{\mathrm{f}} = \left(\frac{\Delta M_{\mathrm{PCr}}}{M_{0,\mathrm{PCr}}} \right) \Big/ T_{1,\mathrm{PCr}}^{\mathrm{app}} \qquad [3.3]$$

where $\Delta M_{PCr} = M_{0,PCr} - M_{ss,PCr}$.

A steady state saturation transfer experiment alone can determine the k_f according to the following equation [189]:

$$k_{\mathrm{f}} = \left(\frac{\Delta M_{\mathrm{PCr}}}{M_{\mathrm{ss,PCr}}} \right) \Big/ T_{1,\mathrm{PCr}}^{\mathrm{int}} \qquad [3.4]$$

The exact value of k_f requires knowledge of intrinsic spin-lattice relaxation time of PCr. In presence of chemical exchange, the progressive saturation experiment is the gold standard for measuring $T_{1,PCr}^{int}$. However, since it has been suggested numerous studies that the $T_{1,PCr}^{int}$ is constant among subjects with different physiological and pathologic conditions [178, 180, 188, 190] and even among different species [191], valid comparisons of CK kinetics between subjects can still be achieved based on $\Delta M_{PCr}/M_{ss,PCr}$ ratio. Moreover, a recent method developed by

Spencer and colleagues allows fast measurement of intrinsic spin-lattice relaxation times in presence of chemical exchange without using multi-point progressive saturation experiment and curve fitting [192, 193].

3.2.4 Numerical Analysis of MST Governing Equations and Novel MST Strategy

A standard pulse sequence for CK MST experiment is composed of three segments (Figure 3.1): a pre-saturation delay (d_1), selective saturation on ATPγ (d_2) and 90° readout pulse followed by free induction decay (FID) acquisition (pw+at). The duration of the readout pulse plus acquisition is usually less than 100 ms and neglectable, thus total repetition time (TR) is approximated by d_1+d_2.

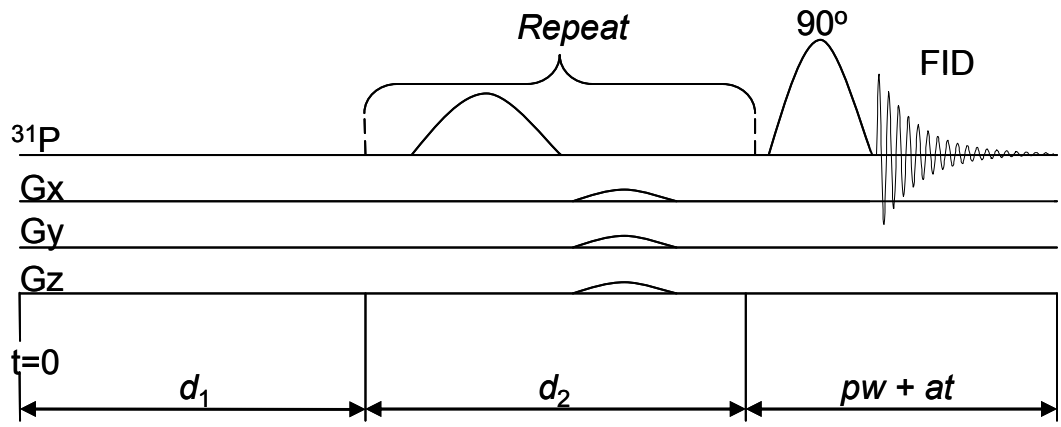

Figure 3.1 Schematic view of pulse sequence used for magnetization saturation transfer study. d_1 is the duration of pre-saturation delay, d_2 is the duration of saturation process, and *pw+ at* is the duration of readout pulse plus acquisition time. Total repetition time TR≈d_1+d_2.

The change of PCr and ATPγ magnetizations along z direction (*M(t)*) during this saturation pulse sequence could be described by the modified Bloch-

Bloch-McConeell equations [194, 195] shown as below:

$$\left.\begin{aligned} \frac{dM_{\mathrm{PCr}}(t)}{dt} &= \frac{M_{0,\mathrm{PCr}} - M_{\mathrm{PCr}}(t)}{T_{1,\mathrm{PCr}}^{\mathrm{int}}} - k_{\mathrm{f}} M_{\mathrm{PCr}}(t) + k_{\mathrm{r}} M_{\gamma\mathrm{ATP}}(t) \quad [3.5] \\ \frac{dM_{\mathrm{ATP}\gamma}(t)}{dt} &= \frac{M_{0,\mathrm{ATP}\gamma} - M_{\gamma\mathrm{ATP}}(t)}{T_{1,\mathrm{ATP}\gamma}^{\mathrm{int}}} + k_{\mathrm{f}} M_{\mathrm{PCr}}(t) - k_{\mathrm{r}} M_{\mathrm{ATP}\gamma}(t) \quad [3.6] \end{aligned}\right\} \; t \in [0,\ d_1]$$

$$\left.\begin{aligned} \frac{dM_{\mathrm{PCr}}(t)}{dt} &= \frac{M_{0,\mathrm{PCr}} - M_{\mathrm{PCr}}(t)}{T_{1,\mathrm{PCr}}^{\mathrm{int}}} - k_{\mathrm{f}} M_{\mathrm{PCr}}(t) \quad [3.7] \\ M_{\mathrm{ATP}\gamma}(t) &= 0 \quad [3.8] \end{aligned}\right\} \; t \in (d_1,\ d_1 + d_2]$$

A numerical analysis of the above equations is shown in Figure 3.2, where the time dependence of PCr and ATPγ magnetizations is plotted against different pre-saturation delays (d_1). This figure suggests two important points: (1) the M_{PCr} relaxation is a single exponential curve (decay or recovery) characterized only by $T_{1,PCr}^{app}$ as long as ATPγ is fully saturated (i.e. $M_{ATP\gamma}(t) = 0$); and (2) the same steady state value of PCr magnetization ($M_{ss,PCr}$) is achieved regardless of d_1. In fact, the explicit expression of $M_{ss,PCr}$ can be obtained by solving equation [3.7] :

$$M_{\mathrm{ss,PCr}} = M_{0,\mathrm{PCr}} \frac{T_{1,\mathrm{PCr}}^{\mathrm{app}}}{T_{1,\mathrm{PCr}}^{\mathrm{int}}} = \frac{M_{0,\mathrm{PCr}}}{1 + T_{1,\mathrm{PCr}}^{\mathrm{int}} k_{\mathrm{f}}} \qquad [3.9]$$

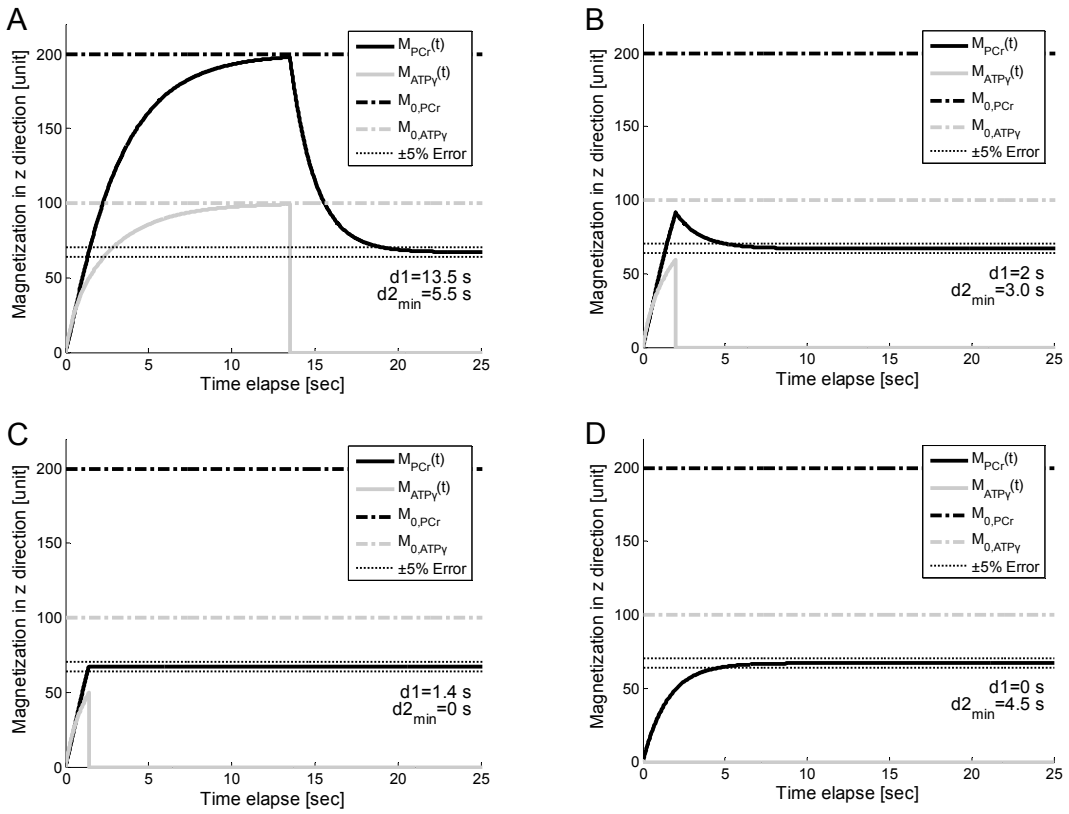

Figure 3.2 The numerical analysis of governing equations [3.5] to [3.8]. Time dependence of PCr and ATPγ magnetizations in z direction during MST pulse sequence (see in Figure 3.1) is plotted with different pre-saturation delays: (A) 13.5 sec, (B) 2 sec, (C) 1.4 sec and (D) 0 sec. Dotted lines indicate ±5% deviations from theoretical $M_{ss,PCr}$ value as given by equation [3.9], from which the minimal saturation time $d_{2,min}$ is defined such that M_{PCr} at the end of saturation process just lies between those lines. Simulation parameters are: k_f=0.44 s^{-1}, $T_{1,PCr}^{int}$=4.5 s, $T_{1,PCr}^{int}$=1.5 s, and $M_{0,PCr}/M_{0,ATP\gamma}$ =2.The simulation demonstrated that the values of $M_{ss,PCr}$ and $T_{1,PCr}^{app}$ are independent of pre-saturation delay (d_1).

Based on the numerical analysis of equations [3.5]-[3.8] which are the governing equations for CK MST experiments, we have derived the following equations ([3.10]-[3.13]), and proposed a novel strategy for MST experiment that can be applied to any solid organ. This novel approach has the following significant benefits:

1. For progressive saturation experiment, short d_1 (d_1=0) can be employed (Figure 3.2D) to yield the same $T_{1,PCr}^{app}$ as measured by conventional method where long d_1 would be employed (Figure 3.2A). The short d_1 strategy can offer great reduction of repetition time (TR). In case of a very limited time window for MST experiment, only one spectrum with ATPγ saturated is needed in additional to $M_{ss,PCr}$ measurement to unambiguously solve the $T_{1,PCr}^{app}$ according to the following equation:

$$T_{1,PCr}^{app} = -TR / \ln(1 - M_{TR,PCr} / M_{ss,PCr}) \qquad [3.10]$$

where $M_{TR,PCr}$ is the PCr signal intensity acquired with a repetition time of TR and continuous saturation on ATPγ.

2. An optimal d_1 ($d_{1,opt}$) can be employed (Figure 3.2B) to yield the same $M_{ss,PCr}$ as measured by conventional method where long d_1 followed by long saturation time (d_2) would be employed. The $d_{1,opt}$ strategy not only reduces the TR but also shortens the duration of saturation pulse required for $M_{ss,PCr}$ quantification. The reduced duration of saturation pulse results in a minimal specific absorption rate (SAR), which is often an FDA concern in clinical studies.

3.3 Results

3.3.1 $d_{1,opt}$ Calculation

As shown in Figure 3.2, in principle, for each CK system with known parameters, there exists an “ideal” pre-saturation delay ($d_{1.ideal}$, shown in Figure 3.2C) such that the PCr signal intensity after pre-saturation delay just equals the

steady state value after a long saturation on ATPγ, i.e.

$$M_{\mathrm{PCr}}(d_{1,\mathrm{ideal}}) = M_{\mathrm{ss,PCr}} \qquad [3.11]$$

When a $d_{1.ideal}$ is applied, an accurate $M_{ss,PCr}$ can be measured without any saturation process, thus the total repetition time will be the shortest. The relaxation process of PCr signal intensity during pre-saturation delay can be approximately described by the following equation [187]:

$$M_{\mathrm{PCr}}(t) = M_{0,\mathrm{PCr}}\left(1-\exp(-t/T_{1,\mathrm{PCr}}^{\mathrm{mix}})\right) \qquad [3.12]$$

where $T_{1,PCr}^{mix}$ is the approximate apparent relaxation time of PCr undergoing chemical exchanges with ATPγ and depends on $T_{1,PCr}^{int}$, $T_{1,ATP\gamma}^{int}$, $M_{0,PCr}/M_{0,ATP\gamma}$, and k_f. By combining equations [3.10]-[3.12], the ideal pre-saturation delay can be calculated as:

$$d_{1,\mathrm{ideal}} = T_{1,\mathrm{PCr}}^{\mathrm{mix}} \ln\left((T_{1,\mathrm{PCr}}^{\mathrm{int}} k_{\mathrm{f}})^{-1}+1\right) \qquad [3.13]$$

Equation [3.13] is not helpful for practical use since $d_{1,ideal}$ calculation requires a k_f value which is the purpose of the experiment itself. However, based on literature and/or prior experiences, a confident estimate of k_f range for a specific study can be made, then an optimized pre-saturation delay ($d_{1,opt}$) can be derived (in contrast to $d_{1,ideal}$ which requires the exact value of k_f) such that, when $d_{1,opt}$ is applied, the required saturation time for accurate quantification of $M_{\mathrm{ss,PCr}}$ is minimal for all possible k_f values within the estimated range.

Based on previous CK reaction rate studies k_f ranges from 0.2-0.8 sec^{-1} under physiological conditions [178-180, 182, 189, 190, 196, 197] and $T_{1,PCr}^{int}$ ranges from 2 to 6 seconds [178-180, 190, 196]. Other parameters that are required for calculation of $d_{1,opt}$ include $T_{1,ATP\gamma}^{int}$ and $M_{0,PCr}/M_{0,ATP\gamma}$ ratio. Under physiological conditions,

$M_{0,PCr}/M_{0,ATP\gamma}$ in the heart is approximately 2 [183, 197, 198], while the ratio of $T_{1,PCr}^{int}/T_{1,ATP\gamma}^{int}$ is approximately 3 [188, 196, 199, 200]. An example of $d_{1,opt}$ calculation for $T_{1,PCr}^{int}$ of 4.5 sec is illustrated in Figure 3.3. The dependence of minimal saturation time ($d_{2,min}$, defined as the minimal saturation time giving rise to a PCr magnetization that is within ±5% deviation from theoretical $M_{ss,PCr}$ value as given by equation [3.9]) upon d_1 and k_f can be obtained by numerically solving equations [3.5]-[3.8] (Figure 3.3A). Among the $d_{2,min}$ vs k_f curves obtained from different d_1 values (Figure 3.3B), there will be one that has the smallest maximum value throughout the physiological k_f range. This curve represents the optimal value of pre-saturation delay ($d_{1,opt}$) and the corresponding optimal duration of saturation pulse ($d_{2,opt}$) required for the physiological k_f range.

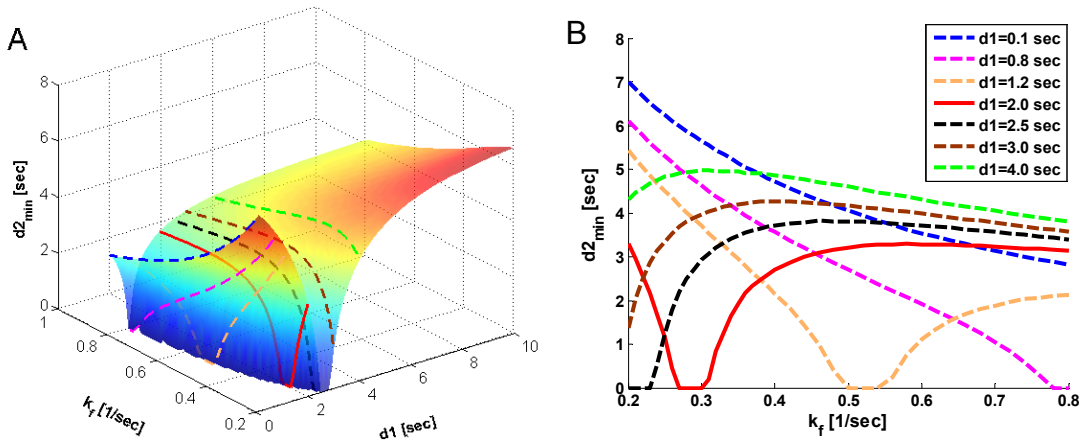

Figure 3.3 $d_{1,opt}$ seeking by numerical solving of equations [3.5] to [3.8]. Parameters for numerical simulation are: k_f=0.2~0.8 s^{-1}, $T_{1,PCr}^{int}$=4.5 s, $T_{1,PCr}^{int}$=1.5 s, and $M_{0,PCr}/M_{0,ATP\gamma}$ =2. Panel (A) is a 3D plot showing the dependence of minimal saturation time ($d_{2,min}$) upon k_f and d_1; panel (B) is a 2D view of (A). The solid line (d_1=2 sec) represents $d_{1,opt}$ condition because the maximum value of $d_{2,min}$ (defined as $d_{2,opt}$) throughout the preset k_f range is the smallest.

3.3.2 Validation of the Novel MST Strategy in in vivo Heart

We firstly validated the $d_{1,opt}$ strategy. To calculate the $d_{1,opt}$ and $d_{2,opt}$ for MST experiment, we have to estimate the intrinsic spin-lattice relaxation time of PCr (Figure 3.4).

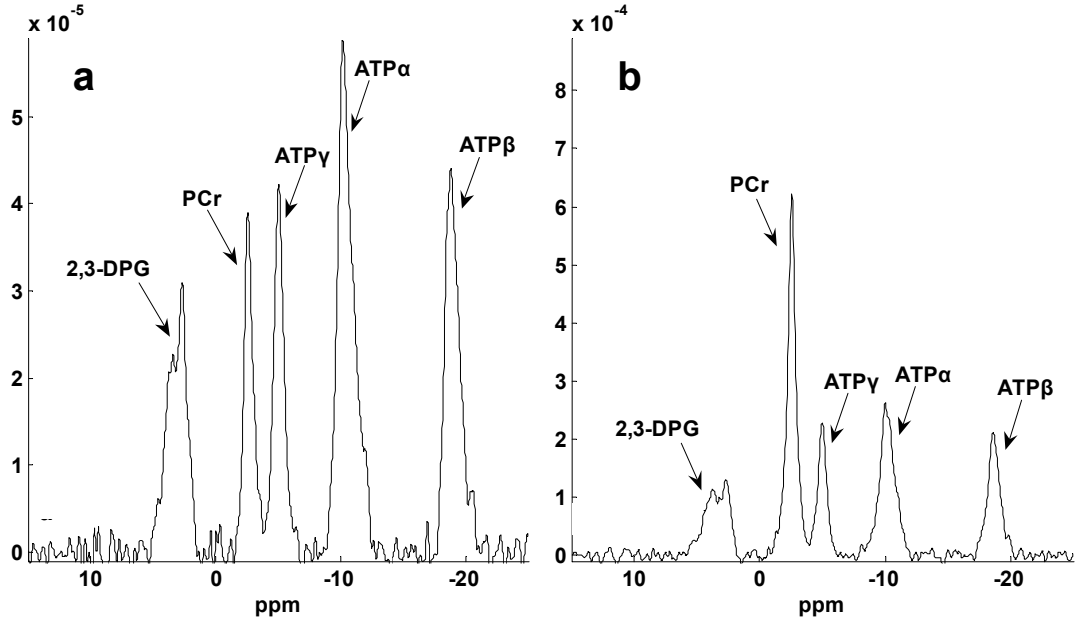

Figure 3.4 $T_{1,PCr}^{int}$ calculation. $T_{1,PCr}^{int}$ was estimated from Spencer's method [201] using two spectra: (a) $M_{short,PCr}$ (TR=0.3 sec, nt=480) and (b) $M_{0,PCr}$ (TR=12 sec, nt=12). The vertical scale of (a) is 15 times of (b) and a larger data acquisition number was employed in (a) for better illustration of the spectra. Both spectra were obtained with a total acquisition time of 2.4 min. The spectra yielded a $T_{1,PCr}^{int}$ value of around 4 sec according to equation [3.14].

Using the method proposed by Spencer et al [192], a short-TR spectrum (see in Figure 3.4a, TR=0.3 sec,) and $M_{0,PCr}$ (Figure 3.4b, TR=12 sec) were used to calculate the $T_{1,PCr}^{int}$ according to equation [3.14]:

$$T_{1,\mathrm{PCr}}^{\mathrm{int}} = TR_{\mathrm{short}} \Big/ \ln\left(1 - \frac{M_{\mathrm{short,PCr}}}{M_{0,\mathrm{PCr}}}\right) \quad [3.14]$$

where TR_{short} and $M_{short,PCr}$ stand for the TR and PCr signal intensity of spectrum 4a, respectively. The calculation resulted in an estimated $T_{1,PCr}^{int}$ of around 4 sec, therefore, a $T_{1,PCr}^{int}$ value of 4.5 sec (10% overestimation based on the mathematical simulation to compensate the possible errors in $T_{1,PCr}^{int}$ measurement) was employed to calculate the $d_{1,opt}$ and $d_{2,opt}$. Other parameters used in calculation are: k_f =0.2~0.8 sec^{-1}, $M_{0,PCr}/M_{0,ATP\gamma}$ = 2 and The calculation yielded a $d_{1,opt}$ value of 2 sec and a $d_{2,opt}$ of 3.3 sec. In order to compensate possible deviations in $M_{0,PCr}/M_{0,ATP\gamma}$ and $T_{1,PCr}^{int}/T_{1,ATP\gamma}^{int}$ estimation, saturation time of 3.5 seconds was applied based on the mathematical The spectra obtained with $d_{1,opt}$ and conventional strategies are shown in Figure 3.5. There was no detectable difference in $M_{ss,PCr}$ measurement between the and the conventional strategies (Figure 3.5, b1 to b3). However, substantial reductions in saturation time (56%) and total repetition time (73%) were granted by using the $d_{1,opt}$ strategy. A control spectrum (Figure 3.5, a2) with saturation pulse set downfield to PCr symmetrically opposite from ATPγ was also acquired. By comparing it with $M_{0,PCr}$ measurement (Figure 3.5, a1), there was no detectable spillover effect on PCr peak with a saturation time of 8 seconds.

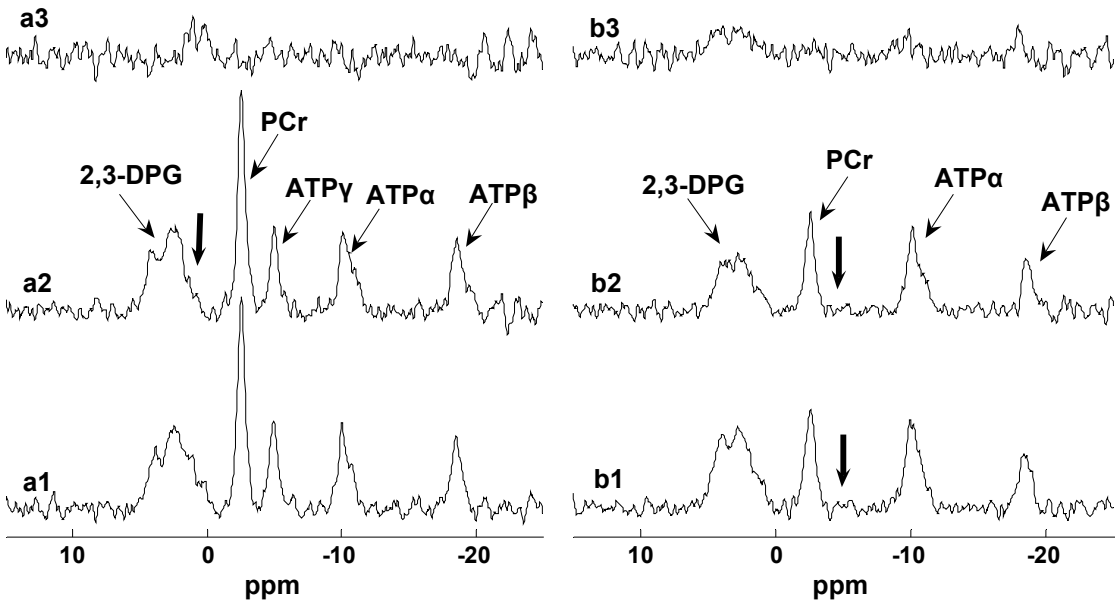

Figure 3.5 Representative steady state saturation transfer spectra for $d_{1,opt}$ strategy validation. Bold arrows indicate the frequency of saturation pulse. Spectrum a1 is the $M_{0,PCr}$ measurement (TR =12 sec and no saturation); spectrum a2 is the control spectrum with saturation pulse set downfield from PCr symmetrically opposite from ATPγ (d_1=12 sec, d_2=8 sec). Spectrum a3=a1-a2. Spectrum b1 and b2 are $M_{ss,PCr}$ measurements using $d_{1,opt}$ (d_1=2 sec and d_2=3.5 sec) and conventional (d_1=12 sec and d_2=8 sec) approaches, respectively. Spectrum b3=b1-b2. All spectra were acquired with 12 averaged FIDs, and the total acquisition times for spectra a1, a2, b1 and b2 were 2.4, 4, 4, 1.1 min, respectively. The spectra demonstrated an identical $M_{ss,PCr}$ measurement obtained by $d_{1,opt}$ and conventional approaches and no spillover effect on PCr signal provided by

A further validation of our novel MST strategy was performed using progressive saturation experiments with long, short and optimal pre-saturation delays (Figure 3.6).

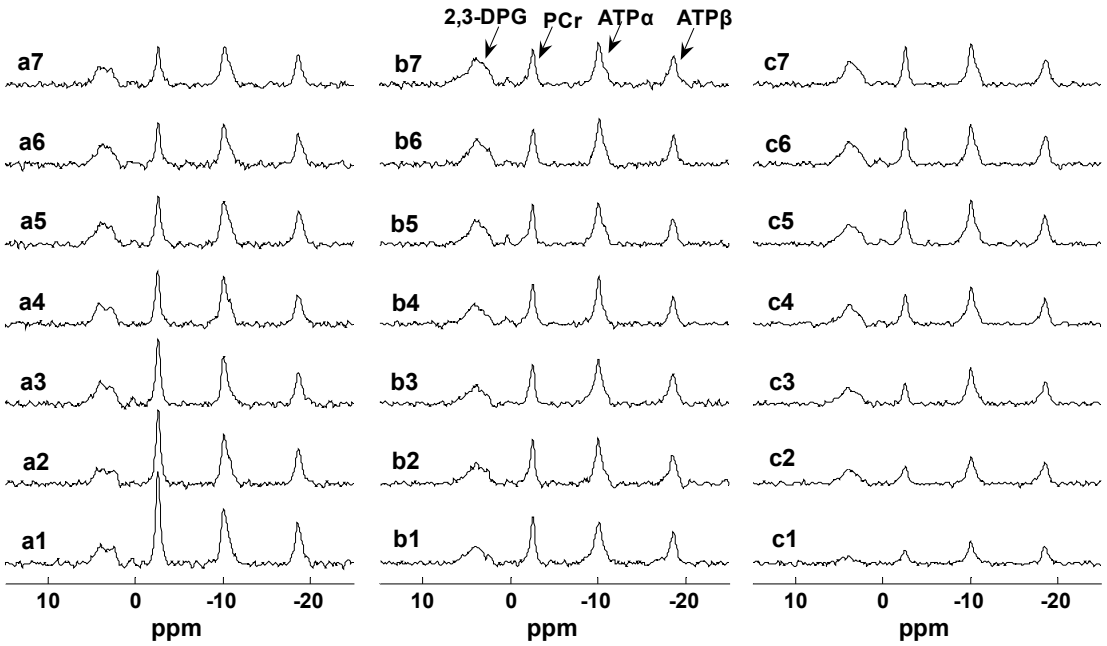

Figure 3.6 Further validation of $d_{1,opt}$ strategy. Shown are typical progressive saturation spectra from same heart with different pre-saturation delays of (a) 7 sec; (b) 2 sec and (c) 0 sec. Spectra 1 to 7 (bottom to top) represent prolonged saturation on ATPγ of 0.5, 1, 1.5, 2.5, 4, 6, 8 sec, respectively. Total data acquisition times for panel a, b and c are 14.5, 7.5 and 5.6 minutes, respectively. These spectra confirmed the simulation results as shown in Figure 3.2.

As saturation times prolonged, PCr peak intensities from all three different pre-saturation delays approached towards the same $M_{0,PCr}$ value. However, in contrast to the long or short pre-saturation delays (Figure 3.6, Panels a and c), initial value of M_{PCr} very close to $M_{ss,PCr}$ was granted when $d_{1,opt}$ was applied (Figure 3.6, Panel b). This further demonstrated the underlying mechanism of saturation time reduction of our $d_{1,opt}$ strategy. A quantification of these progressive saturation experiments was performed and shown in Figure 3.7. The PCr peak areas obtained in progressive saturation experiments from four independent pig hearts were integrated, normalized to $M_{0,PCr}$ of each heart, and

then fitted into the analytical solution of equation [3.7] as follow:

$$\frac{M_{\mathrm{PCr}}(t)}{M_{0,\mathrm{PCr}}} = \frac{\left[M_{\mathrm{PCr}}(0) - M_{\mathrm{ss,PCr}}\right]\exp\left(\dfrac{-t}{T_{1,\mathrm{PCr}}^{\mathrm{app}}}\right)}{M_{0,\mathrm{PCr}}} + \frac{M_{\mathrm{ss,PCr}}}{M_{0,\mathrm{PCr}}} \qquad [3.15]$$

where $M_{PCr}(0)$ is the initial value of $M_{PCr}(t)$ at the start of saturation. Least square fitting yielded $T_{1,PCr}^{app}$ values of 1.53±0.05 sec from d_1=7 sec curve and 1.54±0.05 sec from d_1=0 sec curve, respectively. The almost identical $T_{1,PCr}^{app}$ values retrieved from both curves demonstrate that the short-d_1 progressive saturation can be employed to measure the $T_{1,PCr}^{app}$ instead of the conventional long-d_1 counterpart as stated earlier.

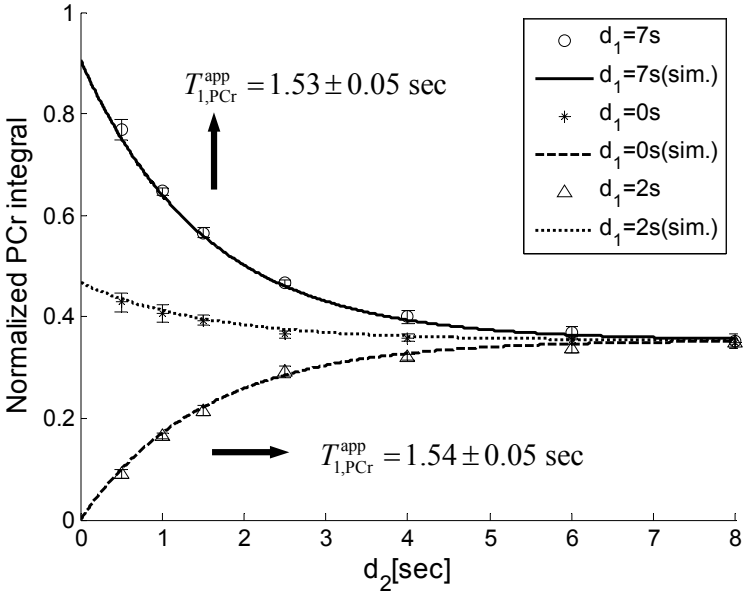

Figure 3.7 Quantification of progressive saturation experiments. A typical set of spectra is illustrated in Figure 3.6. PCr peak integrals obtained from each progressive saturation experiment (d_1 of 0, 2 and 7 sec) were normalized by the $M_{0,PCr}$ value of each heart and plotted against the saturation pulse duration. Data shown were from four independent pig hearts with error bars representing the standard deviation. Also shown in the figure were simulation results (lines) using the k_f and $T_{1,PCr}^{int}$ values from Table 3.2. This figure provided a quantitative validation of our novel MST strategy.

The compiled data from 4 pigs comparing the conventional and novel approaches from same heart are summarized in Table 3.2. Here a TR=1.5 sec spectrum instead of the whole d_1=0 curve was used to calculate the $T_{1,PCr}^{app}$ according to equation [3.10] so that the maximum reduction in TR could be achieved. The detailed reductions in data acquisition time using the novel strategy are summarized in Table 3.3.

Table 3.2 Comparison of measurements between novel and conventional MST strategies from same hearts of four pigs

Strategy	$\Delta M_{PCr}/M_{0,PCr}$	$T_{1,PCr}^{app}$ [s]	$T_{1,PCr}^{int}$ [s]	k_f, [s^{-1}]
Conventional[a]	0.65±0.01	1.53±0.05	4.3±0.2	0.42±0.01
Novel[b]	0.65±0.01	1.56±0.08	4.4±0.2	0.42±0.03

[a]: In conventional approach, progressive saturation transfer experiment with long d_1 was employed to obtain $T_{1,PCr}^{app}$, and long d_1 plus long d_2 was employed for $M_{ss,PCr}$ measurement. k_f was calculated using equation [3.3] and $T_{1,PCr}^{app}$ was calculated using equation [3.2].

[b]: Novel approach used $d_{1,opt}$ plus $d_{2,opt}$ to obtain the $M_{ss,PCr}$ measurement. $T_{1,PCr}^{app}$ was calculated from two spectra (b2 in Fig. 5 and c3 in Fig. 6) according to equation [3.10]: $T_{1,\mathrm{PCr}}^{\mathrm{app}} = -TR / \ln(1 - M_{TR,\mathrm{PCr}} / M_{ss,\mathrm{PCr}})$. Statistical analysis showed no significant difference in any measurement obtained by novel and conventional strategies.

Table 3.3 Comparison of total data acquisition time required for MST measurements between novel and conventional strategies

Strategy	M_0 and M_{ss} TR×nt [sec]	$T_{1,PCr}^{app}$ TR×nt×np [sec]	k_f [minute]
Conventional	(12+20)×12	14.6×12×6 [a]	23.9
Novel	(12+5.5)×12	1.5×30×1 [b]	4.3

[a]: $T_{1,PCr}^{app}$ was calculated from curve fitting of 6 time points (np=6). In conventional approach, 14.6 is the average TR for 6 points. All points were acquired with 12 averaged FIDs (nt=12).

[b]: In novel approach, only TR=1.5 sec spectrum (nt=30, Fig. 6, c3) was used to calculate $T_{1,PCr}^{app}$ together with M_{ss} measurement (nt=12, Fig. 5, b2) according to equation [3.10].

3.4 Discussion

This technical report demonstrates a novel approach in magnetization saturation transfer (MST) experiments which results in a significant reduction in total data acquisition time as well as the duration of saturation pulse. Although the concept has been validated only on myocardial creatine kinase (CK) reaction in the heart, this approach can be applied to other enzyme reactions (such as ATPase) in any solid organs.

3.4.1 Superior Performance Compared to Conventional MST Strategy

The most important advantage of the novel strategy is the reduction of repetition time (TR): the $d_{1,opt}$ approach in steady state saturation transfer

experiment would reduce TR by 73% (5.5 sec in $d_{1,opt}$ approach vs 20 sec in conventional approach), and the total acquisition time for a complete k_f measurement could be reduced by 82% (4.3 min in novel approach vs 23.9 min conventional approach, Table 3.3).

This reduction in TR is significant and will have several future applications. Firstly, it will allow us to determine myocardial CK forward flux rate with transmural differentiation to separate inner layers vs outer layers in open chest preparation. In an early study using a model of normal dog heart, the CK flux measurements with spatial localization required ~6 hours of data acquisition time for one experimental condition [184]. Such a long data acquisition time excludes the CK kinetic measurement of a diseased heart, or CK flux rate changes in response to experimental interventions. Secondly, the novel strategy will facilitate the high field human MST studies using an external coil, in which case similar spatial localization is required. The data acquisition time would be prohibitively long should conventional approach be applied. The strategy presented in this work is compatible with various spatial localization techniques (such as 3D-ISIS and 3D-CSI) and thus would greatly facilitate applications such as CK forward flux rate mapping. We have currently applied this strategy to investigate the ATP production rate via CK forward reaction of rat brain in combination with 3D-ISIS spatial localization techniques. A complete k_f measurement using this novel strategy required only 43 min as compared to ~3 hours in conventional approach [202] (Appendix).

Another advantage brought by this novel strategy is the significant reduction

the duration of saturation pulse train required for $M_{ss,PCr}$ measurement (56% reduction, 3.5 sec in $d_{1,opt}$ approach vs 8 sec in conventional approach). The first beneficial effect from this reduction is the minimal spillover effect on PCr peak of the saturation pulse train and thus better SNR for quantification. In the current work, the novel strategy together with BISTRO saturation pulse train yielded no detectable spillover effect on PCr peak (Figure 3.5, Panel a). Consequently, the control spectrum usually employed in other MST studies [179, 197] can be

A second benefit from the reduced saturation time is related to the specific absorption rate (SAR) issue when human subjects are involved. The minimal saturation time provided by $d_{1,opt}$ strategy can to a large extent relieve the FDA concerns on heat generation by long duration of saturation pulse train employed in conventional MST strategy.

3.4.2 Other Merits of the Novel Strategy

Recently, an important *f*our-*a*ngle *s*aturation *t*ransfer (FAST) method has been developed and utilized for measuring CK reaction rates in humans [182, 183, 203]. method employs a short repetition time ($TR < T_{1,PCr}^{app}$) and different flip angles to calculate the $M_{0,PCr}$, $M_{ss,PCr}$ and $T_{1,PCr}^{app}$. This method is very time efficient and better SNR within a given data acquisition time can be achieved by flip angles optimization. However, the $M_{0,PCr}$, $M_{ss,PCr}$ and $T_{1,PCr}^{app}$ calculations of FAST method heavily rely on the accuracy of designed flip angles. This could be difficult at higher field because of the characteristics of B_1 penetration in high field magnet. A homogeneous flip angle may not be achieved at high field even though adiabatic pulses such as BIR4 or BIRP are employed. The novel strategy

demonstrated in the present study, as an alternative method, can provide the following advantages in addition to reductions in TR and saturation time. Both $M_{0,PCr}$ and $M_{ss,PCr}$ are directly measured, which enables the simple calculation of k_f and insensitivity to flip angle variation. For $T_{1,PCr}^{app}$ calculation, the novel strategy requires only one ATPγ-saturated spectrum (Figure 3.6, c3) in addition to $M_{ss,PCr}$ measurement according to equation [3.10]. The TR for ATPγ-saturated spectrum can be arbitrary and maximum SNR per unit time can be achieved by a flip angle around the Ernst angle.

3.4.2 Validity of the Methodology

The validity of the new methodology was tested in a pig heart model. The results from the novel strategy were the same as the conventional MST method with long pre-saturation delay (Table 3.2). The $T_{1,PCr}^{app}$ values retrieved from d_1 of 0 and 7 sec curves were identical (Figure 3.7). This is consistent with our numerical analysis. The k_f value calculated by using our new strategy yielded a value of 0.42±0.03 sec^{-1} that is similar to our previous report of 0.41±0.03 sec^{-1} [178].

Although we have provided two equations (equations [3.3] and [3.4]) for conventional MST methods, all the k_f calculations described in this work are based on equation [3.3]. A number of previous studies indicated that the $T_{1,PCr}^{int}$ independent of physiological conditions [178, 180, 188, 190], however, variations of $T_{1,PCr}^{int}$ values are observed in the literature. This is likely due to different animal models and different experimental preparations. Therefore, we would

direct determination of $T_{1,PCr}^{int}$ value and use of equation [3.3] for k_f calculation instead of equation [3.4] together with $T_{1,PCr}^{int}$ obtained from literature. The major reason that equation [3.4] was preferred in some studies is because it eliminates the lengthy acquisition time used for progressive saturation experiment to retrieve $T_{1,PCr}^{app}$. However, by using the novel strategy, $T_{1,PCr}^{app}$ can be calculated from one extra ATPγ-saturated spectrum with arbitrary TR. The advantage of this k_f calculation strategy is that it requires no approximation or assumption.

For the purpose of this novel strategy being readily used by others investigators and especially those doing patient studies, we summarized a flow chart in Figure 3.8 to clearly specify each steps of a MR protocol that one could follow in practice to obtain the non-invasive k_f measurements.

Here, we have demonstrated a novel strategy for magnetization saturation transfer (MST) experiments which provides 82% reduction in total data acquisition time as compared to the conventional MST method. The new strategy is based on the numerical analysis of the governing equations of magnetization relaxation, and was validated using an in vivo swine model. This MST strategy can be readily applied to study of other enzyme kinetics (such as ATPase) and in other important organs.

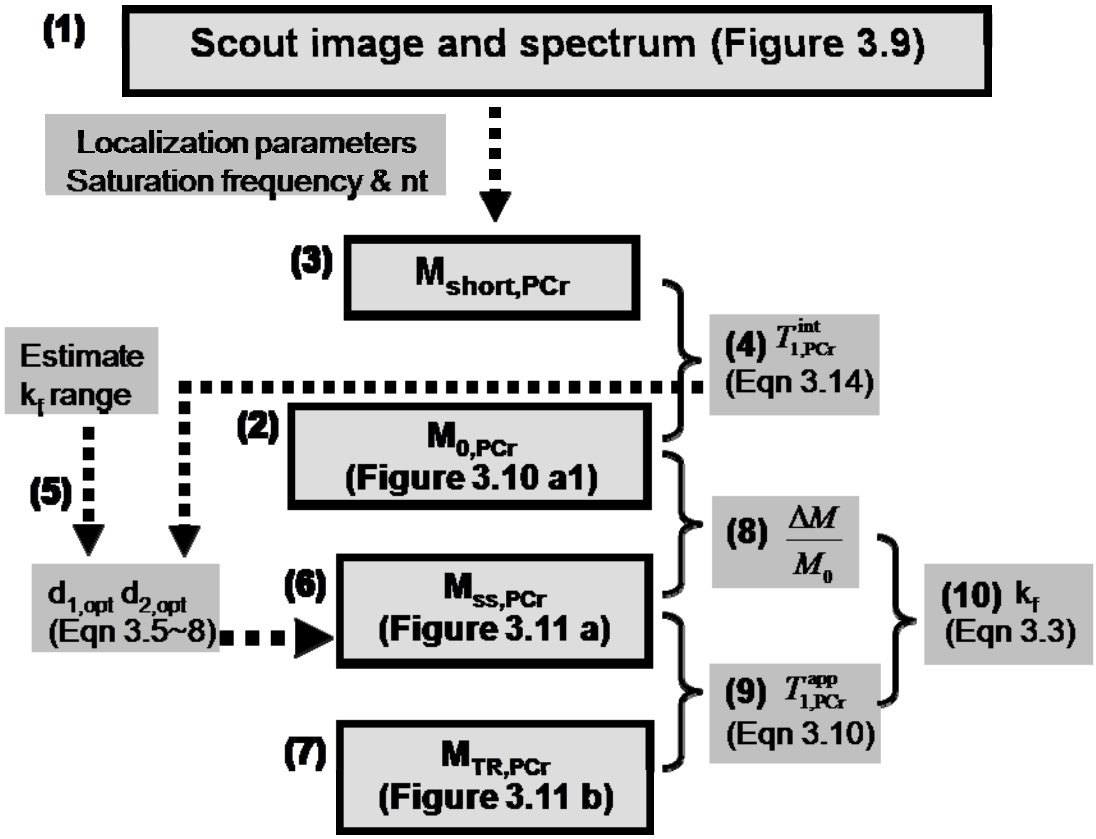

Figure 3.8 $d_{1,opt}$ protocol for k_f calculation. Bold boxes indicate the actual measurements from spectra.

Chapter 4

ATP PRODUCTION RATE VIA CK OR ATPASE IN VIVO: A NOVEL SUPERFAST MAGNETIZATION SATURATION TRANSFER METHOD

4.1 Introduction

The adenosine triphosphate (ATP) metabolism in a living organ is characterized by a chemical exchange network among phosphocreatine (PCr), ATP, and inorganic phosphate (Pi), which is largely controlled by the enzymes creatine kinase (CK, catalyzing PCr↔ATP) and ATP synthase (ATPase, catalyzing Pi↔ATP): [122, 204]

$$\mathrm{PCr} \underset{k_{\mathrm{r,CK}}}{\overset{k_{\mathrm{f,CK}}}{\rightleftharpoons}} \mathrm{ATP} \underset{k_{\mathrm{f,ATPase}}}{\overset{k_{\mathrm{r,ATPase}}}{\rightleftharpoons}} \mathrm{Pi}$$

where k_f and k_r are the pseudo-first-order forward and reverse rate constants for CK and ATPase reactions. Under most *in vivo* circumstances, a steady-state condition is established (i.e. the metabolites concentration does not change with

time), resulting in equal forward and reverse fluxes for both CK and ATPase reactions [122, 204]. Therefore, the kinetics of PCr↔ATP↔Pi chemical exchange can be characterized by two forward pseudo-first-order rate constants ($k_{f,CK}$ for PCr→ATP and $k_{f,ATPase}$ for Pi→ATP), and studied non-invasively by ^{31}P magnetization saturation transfer (MST) experiment where ATPγ resonance is continuously saturated [122, 204].

The exchange rates of CK and ATPase reactions have been extensively studied on various organs, such as heart, brain, and skeletal muscle [137, 176, 205]. Previous studies have suggested that the kinetics of the PCr↔ATP↔Pi exchange network may be associated with the pathological status of the organ. For example, significantly lowered ATP production rates via CK have been observed in association with various heart diseases in both large animals [137, 205] and human patients [142, 174, 183]. In addition, the cerebral ATP metabolic rate through ATPase has been demonstrated to be tightly coupled to brain activity level in a rat model [206] and the CK activity in the visual cortex of human brain was increased during visual simulation [207]. In contrast, in heart it was found that CK forward flux rate was independent from the increase of cardiac workloads in response to catecholamine stimulations [205].

In order to compensate the lengthy data acquisition time imposed by conventional MST technique, Dr. Bottomley *et al.* proposed a four-angle saturation transfer (FAST) method, allowing rapid *in vivo* measurement of CK reaction rates with four short-TR spectra [203]. This method was later employed by Dr. Weiss *et al.* on human patients to examine the myocardial CK reaction

[11]. We have recently reported an improved MST method for measuring CK kinetics with as few as three spectra [208], the method focused on minimizing the saturation time by optimizing the pre-saturation delay, which also resulted in a significant reduction of total TR.

In the present study, we demonstrate a novel steady-state MST method (T_1^{nom}) for performing extremely rapid measurements of CK and ATPase kinetics with **arbitrary** repetition time (TR) and flip angle (α). The accurate quantification of k_f under such partial relaxation conditions requires only two spectra. The T_1^{nom} method is theoretically validated based on numerical simulation of modified Bloch-McConnell equations that govern the evolution of spin magnetizations during MST experiment. In addition, an optimization strategy for finding the best acquisition parameter range (TR and α) used in T_1^{nom} method is provided. The new method is verified experimentally with *in vivo* measurements of: 1) $k_{f,CK}$ on swine heart model during the process of CK inhibition by iodoacetamide (IAA) infusion; and 2) both $k_{f,CK}$ and $k_{f,ATPase}$ on rat brain model at rest condition. Finally, the T_1^{nom} method was employed to measure the cardiac CK forward rate constant with transmural differentiation, demonstrating a reduction of data acquisition time by 91% as compared to a similar study using conventional saturation transfer method [184].

4.2 Theory

4.2.1 k_f Calculation of Conventional Steady-state MST Experiment

Table 4.1 summarizes all the abbreviations and symbols.

Table 4.1 Abbreviations and symbols

Symbols	Actual physical meaning
d_1	The total time in MST experiment that ATPγ is not saturated
k_f	Pseudo-first-order rate constant of enzyme reactions
K_{SNR}	Normalized relative k_f error due to spectral SNR
K_{flip}	Normalized relative k_f error due to flip angle inaccuracy
M_0	Steady-state magnetization in control spectrum obtained under fully relaxed condition
M_{ss}	Steady-state magnetization in saturated spectrum obtained under fully relaxed condition
M_c	Steady-state magnetization in control spectrum obtained under partially relaxed condition
M_s	Steady-state magnetization in saturated spectrum obtained under partially relaxed condition
NEX	Number of excitations for signal averaging
t	Total scan time (equation [4.12])
t_{sat}	The duration of saturation pulse in the MST experiment
T_1^{app}	Apparent longitudinal relaxation time when ATPγ is continuously saturated
T_1^{int}	Intrinsic longitudinal (spin-lattice) relaxation time constant
T_1^{nom}	Nominal T_1, defined as the slope of linear regression of simulated M_c/M_s vs k_f data curves (equation [4.8])
TR	Repetition time of MST experiment.
α	Flip angle of excitation pulse.
β	Intercept of linear regression of simulated M_c/M_s vs k_f data curves (equation [4.8])
σ	Intrinsic MR system noise level (equation [4.12])

The evolution of spin magnetizations in the coupled CK and ATPase reactions can be characterized by the modified Bloch-McConnell equations [209, 210] shown as below:

$$\frac{dM_{\mathrm{PCr}}(t)}{dt} = \frac{M_{0,\mathrm{PCr}} - M_{\mathrm{PCr}}(t)}{T_{1,\mathrm{PCr}}^{\mathrm{int}}} - k_{\mathrm{f,CK}} M_{\mathrm{PCr}}(t) + k_{\mathrm{r,CK}} M_{\mathrm{ATP\gamma}}(t) \qquad [4.1]$$

$$\frac{dM_{\mathrm{Pi}}(t)}{dt} = \frac{M_{0,\mathrm{Pi}} - M_{\mathrm{Pi}}(t)}{T_{1,\mathrm{Pi}}^{\mathrm{int}}} - k_{\mathrm{f,ATPase}} M_{\mathrm{Pi}}(t) + k_{\mathrm{r,ATPase}} M_{\mathrm{ATP\gamma}}(t) \qquad [4.2]$$

$$\frac{dM_{\mathrm{ATP\gamma}}(t)}{dt} = \frac{M_{0,\mathrm{ATP\gamma}} - M_{\mathrm{ATP\gamma}}(t)}{T_{1,\mathrm{ATP\gamma}}^{\mathrm{int}}} + k_{\mathrm{f,CK}} M_{\mathrm{PCr}}(t) + k_{\mathrm{f,ATPase}} M_{\mathrm{Pi}}(t) - (k_{\mathrm{r,CK}} + k_{\mathrm{r,ATPase}}) M_{\mathrm{ATP\gamma}}(t) \qquad [4.3]$$

When ATPγ is selectively saturated as applied in MST experiments, Equations [4.1] to [4.3] change to:

$$\frac{dM_{\mathrm{PCr}}(t)}{dt} = \frac{M_{0,\mathrm{PCr}} - M_{\mathrm{PCr}}(t)}{T_{1,\mathrm{PCr}}^{\mathrm{int}}} - k_{\mathrm{f,CK}} M_{\mathrm{PCr}}(t) \qquad [4.4]$$

$$\frac{dM_{\mathrm{Pi}}(t)}{dt} = \frac{M_{0,\mathrm{Pi}} - M_{\mathrm{Pi}}(t)}{T_{1,\mathrm{Pi}}^{\mathrm{int}}} - k_{\mathrm{f,ATPase}} M_{\mathrm{Pi}}(t) \qquad [4.5]$$

$$M_{\mathrm{ATP\gamma}}(t) = 0 \qquad [4.6]$$

Equation [4.4] and [4.5] are mathematically equivalent, therefore CK and ATPase reactions are treated together using the same equations in the following discussion. The extent of the reduction of PCr and Pi magnetizations in response to ATPγ saturation is proportional to the forward rate constants:

$$k_{\mathrm{f,CK(ATPase)}} = \left(\frac{M_{0,\mathrm{PCr(Pi)}} - M_{\mathrm{ss,PCr(Pi)}}}{M_{\mathrm{ss,PCr(Pi)}}} \right) \Big/ T_{1,\mathrm{PCr(Pi)}}^{\mathrm{int}} \qquad [4.7]$$

where M_{ss} and M_0 represent the fully relaxed magnetizations with and without saturation on ATPγ and T_1^{int} is the intrinsic longitudinal relaxation time constant. k_f

calculation using Equation [4.7] is called conventional steady-state MST experiment, which requires measurement of two fully relaxed spectra (M_0 and [209, 210]. The validity of steady-state MST experiment has been confirmed by the fact that the intrinsic T_1 is constant among subjects with different physiological and pathologic conditions [122, 137, 205, 206, 211-213] and even, in same case, among different species [214]. The reliable intrinsic T_1 can be measured using conventional progressive MST experiment, which employs multiple data acquisitions with progressively prolonged saturation time on ATPγ and thus extremely time consuming.

4.2.2 T_1^{nom} Method for Extremely Rapid k_f Measurement and Quantification

The conventional steady-state MST experiment is inefficient in terms of signal to noise (SNR) per unit acquisition time due to full relaxation prerequisite for both M_0 and M_{ss} measurements. In addition, full relaxation requirement results in very long TR since the ^{31}P metabolites' T_1s are characteristically long [215], which leads to a prohibitively lengthy total acquisition time for studies requiring higher spatial or temporal discrimination.

Preferably such experiments should be performed with a short TR and an appropriate α to maximize the SNR per unit acquisition time. The pulse sequence employed is illustrated in Figure 4.1. For the reason of simplicity, we chose to utilize the same TR and α for both saturated and control spectra.

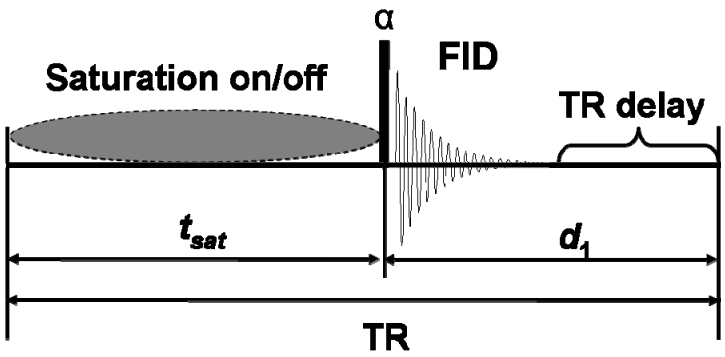

Figure 4.1 Schematic view of pulse sequence used in steady-state magnetization saturation transfer experiment. For control spectrum, the saturation pulse train is replaced by a simple delay (or changed to a symmetrically opposite frequency for correcting spillover effect) such that the repetition time (TR) for both measurements would be same. Arbitrary flip angle (α) for excitation is achieved by BIR4 pulse [216].

Two new steady-state measurements would be obtained from spectra obtained without (M_c) and with (M_s) saturation on ATPγ as compared to M_0 and M_{ss} in conventional steady-state MST experiment (Figure 4.2).

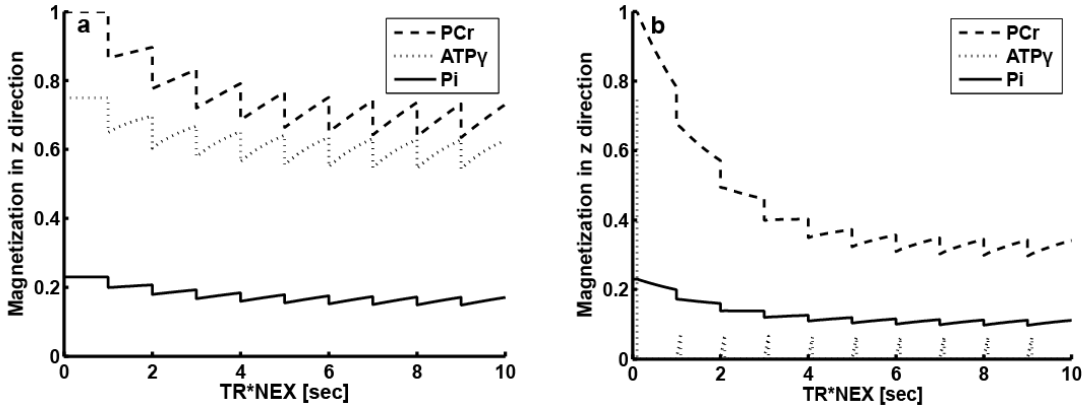

Figure 4.2 Numerical simulation of Equations [4.1] to [4.6] using human brain data at 7 Tesla [211], demonstrating new steady-state magnetizations (M_c (panel a) and M_s (panel b)) under partial relaxation condition. Spin system parameters: pool size ratio of PCr : ATPγ : Pi = 1 : 0.75 : 0.23; intrinsic T_1 for PCr, ATPγ and Pi are 4.86, 1.35 and 3.77 s. Chemical exchange parameters: $k_{f,CK}$ = 0.3 s^{-1}; $k_{f,ATPase}$ = 0.18 s^{-1}. Acquisition parameters: TR= 1 s, α = 30°, d_1 = 0.1 s.

In this case, Equation [4.7] no longer holds for k_f calculation due to extra saturation factor from partial relaxation. The new relationship between k_f value and the extent of magnetization reduction in response to ATPγ saturation can be elucidated by numerical simulation with various k_f values and acquisition parameters (Figure 4.3).

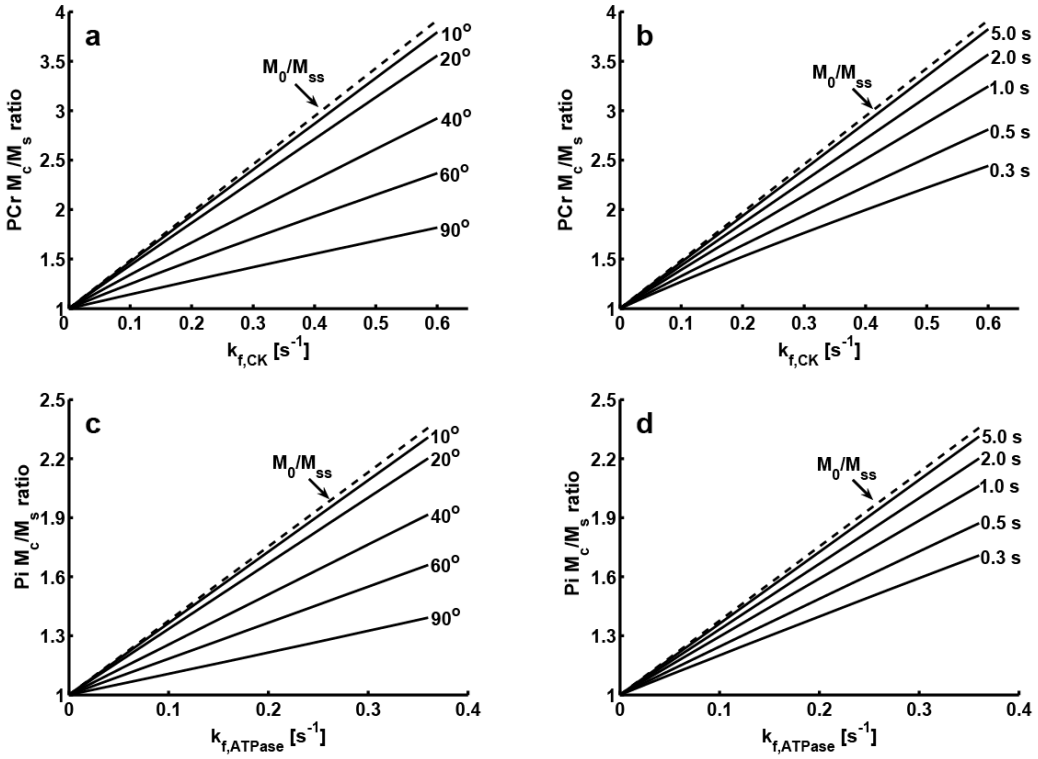

Figure 4.3 Preserved linear relationship between M_c/M_s ratio and k_f in partially relaxed conditions. M_c/M_s ratio vs k_f plots are generated with simulation for CK (a, b) and ATPase (c, d) reactions of human brain at 7 T under various flip angles (a and c, TR = 1 sec) and repetition times (b and d, $\alpha = 30^o$). Spin system parameters: pool size ratio of metabolites (PCr : ATPγ : Pi) = 1 : 0.75 : 0.23; intrinsic T_1 for PCr, ATPγ and Pi are 4.86, 1.35 and 3.77 s. Chemical exchange parameters: $k_{f,CK}$ = 0~0.6 s^{-1}; $k_{f,ATPase}$ = 0~0.36 s^{-1}. Acquisition parameter: d_1 = 0.1 s.

The simulation results suggest an approximately linear relationship between M_c/M_s ratio and k_f values under various acquisition conditions. Therefore, based

on a simple linear regression, Equation [4.7] can be re-formulated into the following equation for k_f quantification under partial relaxation conditions:

$$\frac{M_{\mathrm{c,PCr(Pi)}}}{M_{\mathrm{s,PCr(Pi)}}} \approx \beta + T_{1,\mathrm{PCr(Pi)}}^{\mathrm{nom}} \cdot k_{\mathrm{f,CK(ATPase)}} \quad [4.8]$$

where β is the intercept (usually within ±5% of 1) and T_1^{nom} is the slope of the line obtained by linear regression of the simulated M_c/M_s vs k_f plot. Equation [4.8] is similar to the following equation which is the rearrangement of Equation [4.7] (dashed lines in Figure 4.3):

$$\frac{M_{\mathrm{0,PCr(Pi)}}}{M_{\mathrm{ss,PCr(Pi)}}} = 1 + T_{1,\mathrm{PCr(Pi)}}^{\mathrm{int}} k_{\mathrm{f,CK(ATPase)}} \quad [4.9]$$

Equation [4.8] indicates that, the partial relaxation effects can be largely accounted for by one empirical parameter T_1^{nom} (means nominal T_1 in contrast to intrinsic T_1 as in Equation [4.9]). In general, T_1^{nom} is a function of both spin system parameters (T_1^{int} and pool size ratios of metabolites, such as PCr/ATP or Pi/ATP ratio), and acquisition parameters (TR and α) and it approaches to T_1^{int} as TR increases and/or α decreases:

$$T_1^{\mathrm{nom}} = f\left(T_1^{\mathrm{int}},\ \text{pool size ratio};\ TR,\ \alpha\right) \quad [4.10]$$

There is no general analytical expression for Equation [4.10], however, the value of T_1^{nom} can be obtained with linear regression of simulated M_c/M_s vs k_f plot based on Equation [4.1] to [4.6]. In practice T_1^{nom} and β can be empirically determined for specific experimental setup, and then k_f value can be readily calculated with M_c and M_s measurements according to Equation [4.8].

4.2.3 Optimization Strategy for T_1^{nom} Method

T_1^{nom} method allows k_f calculation with arbitrary repetition time and flip angle. However, the best experimental condition (optimal TR and α) remains unclear. Here we provide an optimization strategy to generate the best TR/α range for T_1^{nom}-based k_f measurement and quantification. The goal of optimization is to have the smallest relative k_f calculation error for a given data acquisition time. Three types of k_f error have been considered in this section. Analytical expression for each type is provided followed by a demonstration of parameter optimization using human brain data at 7 Tesla [211].

Type 1 Error: M_c/M_s vs k_f Nonlinearity

M_c/M_s vs k_f plot in Figure 4.3 are not perfectly straight lines. The relative k_f calculation error due to non-linearity is defined as below:

$$\left(\frac{\delta k_f}{k_f}\right)_{NLIN} = \frac{\left|k_f^{real} - k_f^{cal}\right|}{k_f^{real}} \quad [4.11]$$

where k_f^{real} and k_f^{cal} stand for actual k_f and k_f calculated from Equation [4.8], respectively. The deviation due to nonlinearity is acquisition condition dependent, thus the optimization can be performed such that the type 1 error is minimized.

Type 2 Error: Spectral SNR

k_f calculation is based on two measurements from control (M_c) and saturated (M_s) spectra (Equation [4.8]), each of which is subject to sampling error due to finite spectral SNR. The measurement error of each spectrum would in turn contribute to the final k_f calculation error following error propagation theory.

Assuming a constant total acquisition time (t) and intrinsic scanner noise level

(σ), the final k_f relative error due to spectral SNR can be expressed as:

$$\left(\frac{\delta k_f}{k_f}\right)_{SNR} = \frac{M_c/M_s}{M_c/M_s - \beta}\sqrt{1+\left(\frac{M_c}{M_s}\right)^2}\frac{\sqrt{TR}}{M_c}\frac{\sqrt{t}}{\sigma} \quad [4.12]$$

Equation [4.12] takes into account both the SNR of each spectrum (M_c and M_s) and the sensitivity level of k_f calculation towards spectral errors (T_1^{nom} value). A normalized type 2 error (K_{SNR}) can be introduced from Equation [4.12]:

$$K_{SNR} = \left(\frac{\delta k_f}{k_f}\right)_{SNR}\Big/\frac{\sqrt{t}}{\sigma} = \frac{M_c/M_s}{M_c/M_s - \beta}\sqrt{1+\left(\frac{M_c}{M_s}\right)^2}\frac{\sqrt{TR}}{M_c} \quad [4.13]$$

Due to lack of extra information on MR system performance or total data acquisition time, the optimization strategy is based on minimizing K_{SNR} level.

Type 3 Error: Flip Angle Inaccuracy

Flip angle can vary spatially due to B_1 field inhomogeneity, especially in the case of surface coil and ultra-high magnetic field. Such variation can be greatly minimized by using adiabatic pulses (such as BIR4 pulse as employed in this study [216]). Therefore, the accuracy of k_f calculation based on T_1^{nom} method would be affected by flip angle variation. The relative k_f calculation error due to flip angle inaccuracy can be expressed by the following equation:

$$K_{flip} = -\left(\frac{\delta k_f}{k_f}\right)_{flip}\Big/\frac{\delta\alpha}{\alpha} \approx \frac{\partial T_1^{nom}}{\partial\alpha}\frac{\alpha}{T_1^{nom}} \quad [4.14]$$

K_{flip} is a non-dimensional parameter that characterizes the sensitivity level of k_f error due to flip angle error, i.e., a smaller absolute K_{flip} value means the k_f calculation is more robust against flip angle variation. The negative sign in Equation [4.14] indicates that an underestimation of flip angle would result in

overestimation of k_f and vise versa. The optimization strategy hereby is to find the acquisition conditions that lead to a K_{flip} value below an arbitrary level.

As a demonstration, numerical simulation for each type of k_f error (Equations [4.11], [4.13] and [4.14]) have been carried out based on human brain data at 7 Tesla [211] and the results are shown in Figure 4.4a-f. By setting arbitrary cutoff criteria for each type of k_f error, the overall optimized TR and α range for the T_1^{nom} experiment can be obtained (Figure 4.4g-h, shadowed regions).

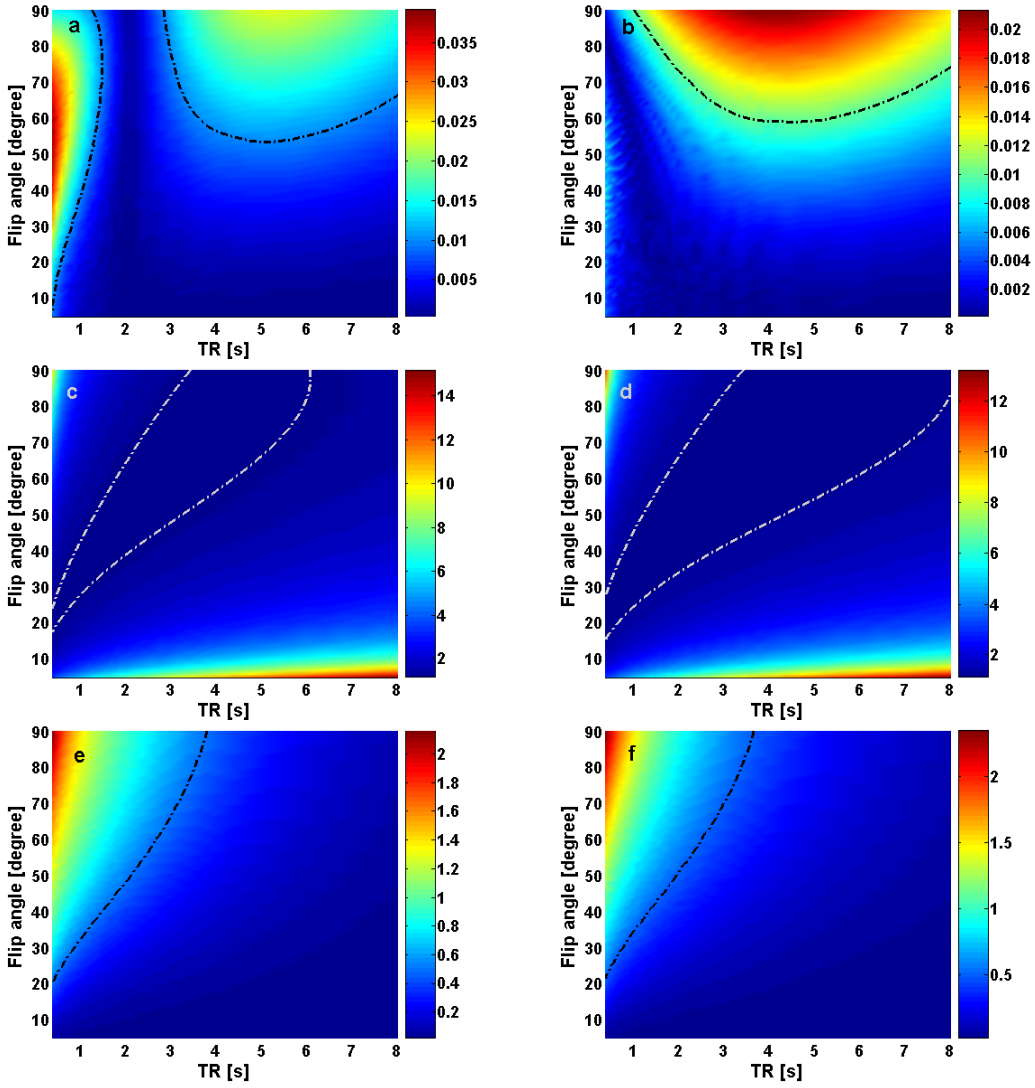

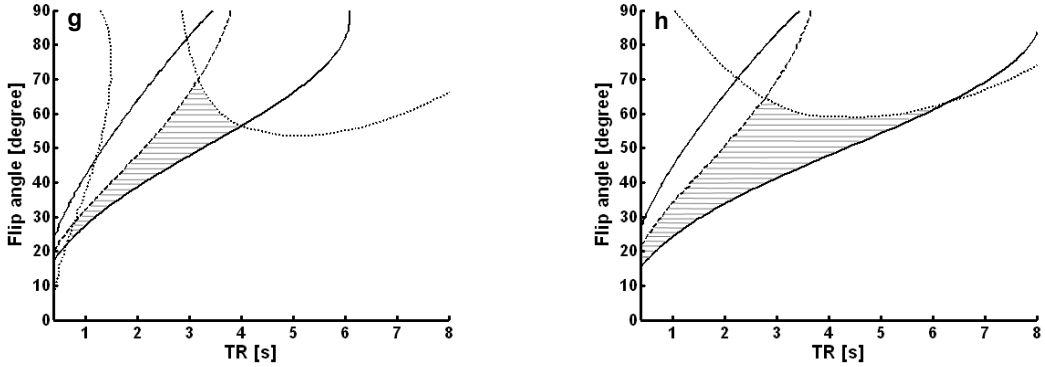

Figure 4.4 Demonstration of optimization strategy. Numerical simulation of three types of k_f error for CK (a, c, e) and ATPase (b, d, f) reactions: T_1^{nom} nonlinearity (a, b), spectral SNR (c, d) and flip angle inaccuracy (e, f). Parameters used for numerical simulation were the same as in Figure 4.3. The dash-dotted lines (0.01 for a and b; 1.2 for c and d, -0.5 for e and f) represent the criteria used in optimization strategy for choosing the best TR and α ranges. The best TR and α range that satisfies all the criteria are shown in panel g (CK) and h (ATPase) as shadowed regions.

4.3 Materials and Methods

All experiments were performed in accordance with the animal use guidelines of the University of Minnesota, and the experimental protocol was approved by the University of Minnesota Research Animal Resources Committee. The investigation conformed to the "Guide for the care and use of laboratory animals" published by the National Institutes of Health (NIH publication No 85-23).

4.3.1 Swine Heart in vivo Studies

Validation of T_1^{nom} method was performed with a creatine kinase (CK) inhibition experiment by iodoacetamide (IAA), an irreversible CK inhibitor [141]. Young female Yorkshire swine (~30 kg, n=8) were employed for the study.

Iodoacetamide solution (450 mM) was administrated (1 mL/kg/hr iv), and a complete CK activity inhibition (as evidenced by $M_{0,PCr} = M_{ss,PCr}$) was usually achieved with a total dose of 0.45 mmol/kg iv. Infusion was paused every 10 min, and steady-state MST experiments were performed in both fully and partially relaxed conditions, with interleaved acquisition. Dummy scans were employed to enforce steady state for MST experiments with partial relaxation. 5 more pigs received an extra catecholamine intervention (Dopamine/Dobutamine, each of 10 μg/kg/min iv) after complete inhibition of CK. Details of the open-chest surgery preparation and ^{31}P MRS have been described previously [205].

Open-chest Surgery Preparation for ^{31}P MR Spectroscopy

Young female Yorkshire swine (~30 kg, n=8) were anesthetized with 2% isoflurane and ventilated with supplemental oxygen on a respirator. Polyvinyl chloride catheters (3 mm OD) were inserted into the ascending aorta (through the left external carotid artery) and left ventricle (through the apical dimple) for hemodynamic monitoring. The heart was exposed via a sternotomy and suspended in a pericardial cradle. The LV catheter was introduced. Ventilation rate, volume, and inspired oxygen content were adjusted to maintain physiological values for arterial PO_2, PCO_2, and pH. Aortic and LV pressures were continuously monitored throughout the study.

In Vivo ^{31}P MR Spectroscopy

Measurements were performed in a 65 cm bore 9.4 T magnet interfaced with a Vnmrj console (Varian, CA). Radiofrequency transmission and MRS signal detection were performed with a 28 mm-diameter double tuned (^{1}H and ^{31}P)

surface coil sutured directly to the epicardium of LV anterior wall. The coil was cemented to a sheet of silicone rubber 0.7 mm in thickness and approximately larger in diameter than the coil itself. The proton signal from water detected with the surface coil was used to homogenize the magnetic field and to adjust the position of the animal in the magnet so that the coil was at or near the magnetic isocenter. ^{31}P MR spectra were acquired with adiabatic BIR4 RF pulses for excitation to minimize flip angle variation due to B_1 inhomogeneity from surface coil. Selective saturation on γ-adenosine triphosphate (ATPγ) was achieved with *B*1-insentitive *tr*ain to *o*bliterate signal (BISTRO) as previously reported [208, 217]. Chemical shifts were measured relative to PCr, which was assigned a chemical shift of 0 ppm. Before and after complete inhibition of creatine kinase reaction, intrinsic T_1 values were measured using progressive MST and inversion recovery methods, respectively.

Transmurally Differentiated Measurement of CK Forward Flux Rate Constant

T_1^{nom} method was further employed to measure the cardiac CK activity with transmural differentiation on female Yorkshire pigs (~40 kg, n=4). Experimental preparations were performed with identical setup as described in the previous section except that a one dimensional chemical shift imaging (1D-CSI) sequence was utilized for transmural differentiation. Parameters for 1D-CSI experiment are: Field of view = 40 mm, phase encoding steps = 17, TE= 620 μs, TR= 3 sec, flip angle =90^o, NEX= 8. Phase encoding direction was chosen to be perpendicular the surface coil plane based on scout cardiac MRI. 1D-CSI data acquisition was gated with both respiratory and cardiac cycle using a model 1025 monitoring and

gating system (SAII instruments, NY) to minimize motion artifacts. A total of two sets of 1D-CSI data were acquired with or without saturation on ATPγ resonance. A Fourier series windowing (FSW) algorithm [218] was employed for post-data reconstruction which can improve the spectral signal to noise ratio. The reconstructed voxel can be arbitrarily shifted. In current study, a 9-term FSW (hann function) reconstruction was performed which yielded three spectra corresponding to the epi-, mid- and endo-layer of the myocardium with minimal overlap between layers. Transmural k_f was calculated from the epi- and the endo-spectra using a T_1^{nom} value of 1.8 sec.

Magnetic Resonance Imaging (MRI) Methods

To examine whether the LV contractile function can be maintained when the CK system is completely inhibited, additional 6 swine were employed for the cardiac MRI study on a clinical 1.5 T scanner. LV chamber function was during the experimental conditions of: a) baseline (BL), b) high cardiac workload (HWL) secondary to catecholamine stimulation (dobutamine and dopamine, each of 10 μg/kg/min, iv), c) re-baseline after iodoacetamide infusion to inhibit CK 0.45 mmol/kg, iv), and d) high cardiac workload after iodoacetamide infusion (IAA+HWL, dobutamine and dopamine, each of 10 μg/kg/min, iv). Data time was 15 minutes for each experimental condition. Detailed MRI methods been published previously [59]. Briefly, MRI was performed on a 1.5 Tesla clinical scanner (Siemens Sontata, Siemens Medical Systems, Islen NJ) using a phased-phased-array 4-channel surface coil and ECG gating. Animals were anesthetized with 2% isoflurane and positioned in a supine position within the scanner. The

MRI protocol consisted of: 1) localizing scouts to identify the long- and short-axis of the heart, 2) short- and long-axis cine for the measurement of global cardiac function. Steady-state free precession “True-FISP” cine imaging used the following MR parameters: TR = 3.1 ms, TE = 1.6 ms, flip angle = 79^{o}, matrix size 256 x 120, field of view = 340 mm x 265 mm, slice thickness = 6 mm (4 mm gap between slices) and 16-20 phases were acquired across the cardiac cycle. function and regional wall thickness data were computed from the short-axis cine images using MASS (Medis Medical Imaging Systems, Leiden, The Netherlands) for the manual segmentation of the endocardial and epicardial surfaces at both end-diastole (ED) and end-systole (ED) from base to apex.

4.3.2 Rat Brain in vivo Studies

Details of rat preparation as well as MRS data acquisition have been published previously [206]. Briefly, five male Sprague-Dawley rats were anesthetized with 2% isoflurane and the femoral arteries of rats were for blood sampling and physiology monitoring. *In vivo* MR experiments were conducted at a 9.4T horizontal animal magnet (Magnex Scientific) interfaced to a Varian INOVA console. A dual RF surface-coil probe consisting of a butterfly-butterfly-shape ^{1}H surface coil and an elliptical-shape ^{31}P surface coil was used for acquiring anatomy images, B_0 shimming and *in vivo* ^{31}P spectra, respectively. A BISTRO saturation pulse train scheme and a BIR4 pulse were used to saturate ATPγ resonance and to read out ^{31}P signal, respectively. Both fully (TR=10 s, α=90^{o}) and partially (TR=3 s, α=45^{o}) relaxed steady-state saturation transfer experiments were performed with 256 signal averages.

4.4 Results

4.4.1 Cardiovascular Physiologic Studies using a Swine Model

^{31}P MR Spectroscopy Data

Intrinsic T_1 measurements before and after complete CK inhibition yielded the same results for PCr (3.2±0.2 vs 3.1±0.2 s, p=NS, see in Figure 4.5), suggesting that T_1^{int} value is independent of CK activity and thus it is feasible to apply T_1^{nom} method to calculate the CK activity based on constant T_1^{int} value.

Figure 4.6 illustrates the representative spectra from steady-state MST experiments with various acquisition conditions throughout the CK inhibition process. ATPγ saturation was achieved by BISTRO saturation pulse train [219], which has been shown to have negligible spillover effects on the neighboring PCr peak [208]. As CK gets completely inhibited (top to bottom), the PCr magnetization in saturated spectra (Sat.) all approaches to that of control spectra (Con.) regardless of acquisition conditions, in agreement with Equation [4.8] that when k_f equals 0, M_c/M_s ratio equals 1. Whereas before CK was completely inhibited, the difference of PCr magnetization between control and saturated spectra is smaller in partially relaxed conditions (b-d) as compared to fully relaxed condition (a), in agreement with the numerical simulation that T_1^{nom} is smaller than T_1^{int}.

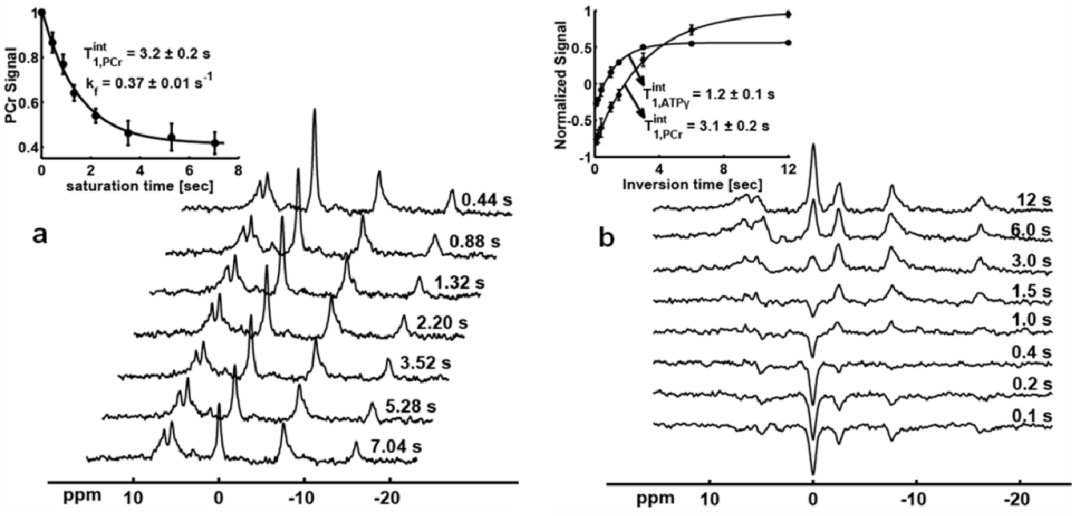

Figure 4.5 Measurement of intrinsic T_1. (a) progressive magnetization saturation transfer before CK inhibition and (b) inversion recovery after CK inhibition. NEX=8 for each spectrum. Calculation of intrinsic T_1 is performed by fitting the PCr or ATPγ signals to an exponential relaxation model (shown in figure insets). Error bar represents the standard error from 4 independent pigs.

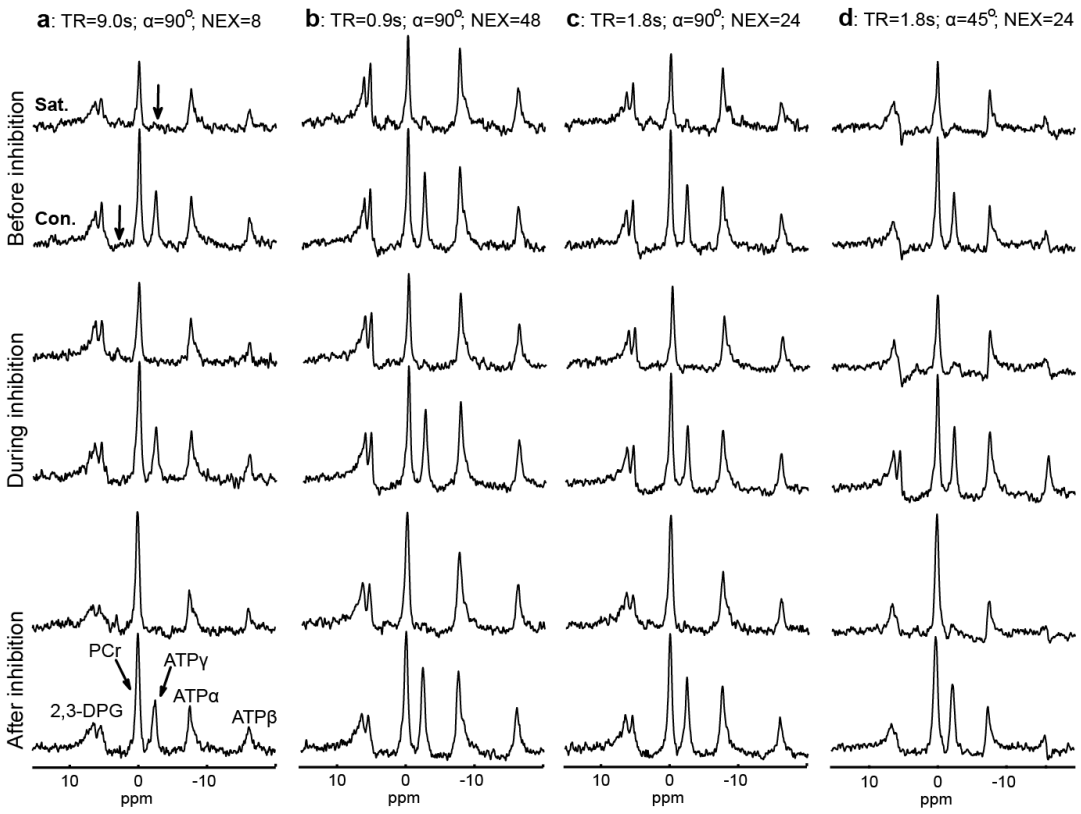

Figure 4.6 Representative spectra from steady-state MST experiments before, during and after CK inhibition. Each steady-state MST experiment consisted of two spectra, with saturation pulse set at ATPγ frequency (Sat.) or symmetrically opposite site (Con.), as indicated by the bold arrows. Spectra from different columns (a-d) were acquired with different acquisition parameters as indicated by the legend on top. Condition a utilized full relaxation, representing the conventional method whereas all the others utilized partial relaxation, representing the T_1^{nom} method. Condition d represents an optimized condition according to the optimization strategy (similar to figure 4.4g and not shown). NEX: number of excitations for signal averaging.

PCr signals measured with partially relaxed conditions (Figure 4.6b-d) throughout the CK inhibition process were quantified, and the ratio of PCr signals in control and saturated spectra was plotted against the CK k_f value as measured by conventional steady-state MST experiments (Figure 4.7). The plot indicates a linear relationship between PCr signal ratios and k_f value, with a slope depending

on the acquisition parameters. Also included in Figure 4.7 (solid lines) are the simulation results with the same parameters as utilized by the experiment. The experimental results matched the simulation well, indicating the validity of T_1^{nom} method. Notably, the steady-state MST experiments in condition d produced the least k_f measurement error as compared to conditions b and c, consistent with prediction based on the simulation results using the optimization strategy.

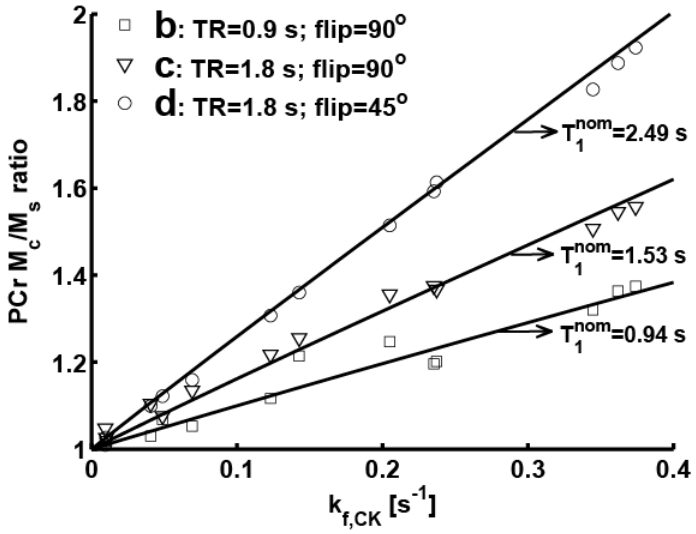

Figure 4.7 Quantification of steady-state MST results from the MRS data used in Figure 4.6. PCr signal ratio from conditions b-d were plotted against k_f value which was calculated according to Equation [4.7] from condition a. The solid lines were generated from simulation with the same parameters as in conditions b-d.

Figure 4.8 illustrates a typical set of transmurally differentiated measurement of creatine kinase forward flux rate constant ($k_{f,CK}$) using T_1^{nom} method in combination of 1D-CSI sequence. The 1D-CSI spectra (Figure 4.8, panel b) displayed a typical “column” along the phase encoding direction perpendicular to the surface coil plan, as demonstrated by the minimal overlap of the resonances representing different depths away from the surface coil. Namely,

signals are from compounds of: localization phantom (Na_3PO_4), coil, myocardium characterized by high levels of PCr and ATP, and erythrocytes from the LV cavity blood characterized by 2,3-DPG peaks. The particular setup generated a T_1^{nom} of 1.8 sec, which was utilized for k_f calculation according to Equation [4.8]. Panel c illustrates the reconstructed spectra demonstrating the spatially localized k_f measurements from the subepi- and the subendo- layers of LV anterior wall. Based on 4 swine studies, the corresponding k_f values are 0.36±0.03 s^{-1} and 0.40±0.03 s^{-1} for subepi- and subendo- myocardial layers , respectively.

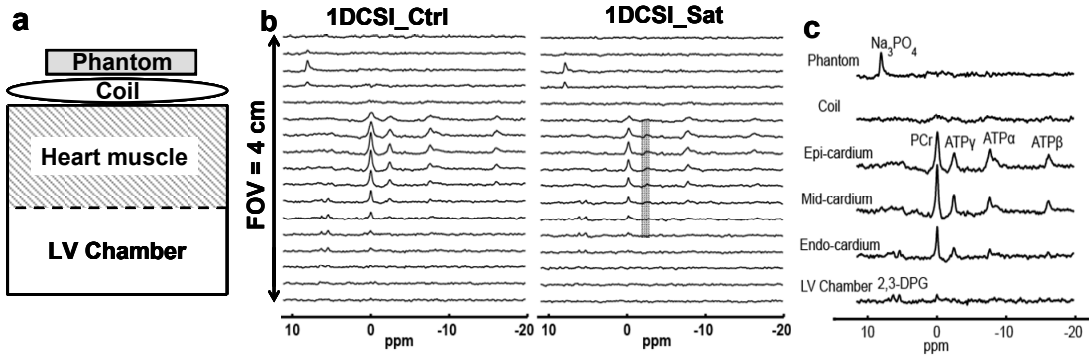

Figure 4.8 Transmural measurement of creatine kinase forward flux rate constant ($k_{f,CK}$) using T_1^{nom} method in combination of 1D-CSI sequence. Panel a, schematic view of the experimental setup. A phantom tube (200 μL 0.5 M Na_3PO_4 in water) was sutured onto the surface coil as a spatial reference. Panel b, representative 1D-CSI spectra with (1DCSI_Sat, saturation pulse indicated by grey band) and without (1DCSI_Ctrl) saturation on ATPγ resonance for transmural measurement of $k_{f,CK}$. Total data acquisition time is 13.6 min with a spatial resolution of 2.4 mm. Acquisition parameters are: field of view (FOV)=40 mm, phase encoding steps=17, TR=3 sec, flip angle=90^o, NEX=8. Panel c, reconstructed transmural spectra from 1D-CSI data for actual k_f calculation. A 9-term Fourier series windowing algorithm [109] was employed for the spectra reconstruction in order to increase the spectral signal-to-noise ratio. The reconstructed voxel can be arbitrarily shifted. T_1^{nom} is calculated to be 1.8 sec based on the acquisition parameters.

Hemodynamic, Myocardial energetics and MRI data in response to CK Inhibition

The hemodynamic and myocardial energetic data in response to CK inhibition via iodoacetamide infusion are summarized in Table 4.2 and 4.3, respectively. Iodoacetamide infusion significantly increased the heart rate ($p<0.05$ vs baseline). However, within an observation window of 30 min, both the LV systolic pressure (LVSP) and the high energy phosphate PCr/ATP ratio are maintained despite of complete inhibition of CK activity. In respond to catecholamine stimulation, both the heart rate and LV systolic pressure increased significantly (Table 4.3, $p<0.05$ vs IAA).

Table 4.2 Hemodynamic data in response to CK inhibition

N=8	HR (bpm)	LVSP (mmHg)	LVEDP (mmHg)
Baseline	104±13	102±6	7±2
CK inhibition (30 min)	124±11*	99±7	7±3
CK inhibition (40 min)	135±12*	90±9	7±4
CK inhibition (60 min)	105±11	70±6*	7±2

Data are mean±SD; *, $p<0.05$ vs Baseline; LVSP, left ventricular systolic pressure; LVEDP, LV end diastolic pressure. CK inhibition was achieved with iodoacetamide infusion (0.45 mmol/kg iv).

Table 4.3 Preservation of high energy phosphates (HEP) ratio despite of CK inhibition at both baseline and high workload (HWL) conditions

N=5	HR	LVSP	PCr/ATP
Baseline	96±10	103±3	2.1±0.2
IAA	120±10*	98±8	2.3±0.3
IAA+HWL	176±12*†	133±7*†	2.4±0.3

Data are mean±SD; *, $p<0.05$ vs Baseline; †, $p<0.05$ vs IAA. IAA, CK inhibition by iodoacetamide infusion (0.45 mmol/kg, iv). IAA+HWL, CK inhibition at high cardiac workload condition (dobutamine and dopamine infusion, each10 μg/kg/min, iv)

The LV contractile functions measured by cardiac MRI during baseline and high cardiac workload states with or without creatine kinase inhibition are summarized in Figure 4.9. The LV contractile functions in terms of ejection fraction and systolic thickening fraction were not impaired during CK inhibition. Moreover, despite of CK inhibition, the heart can respond to catecholamine stimulation with an increased ejection fraction as non-inhibited hearts do ($p<0.05$ vs IAA).

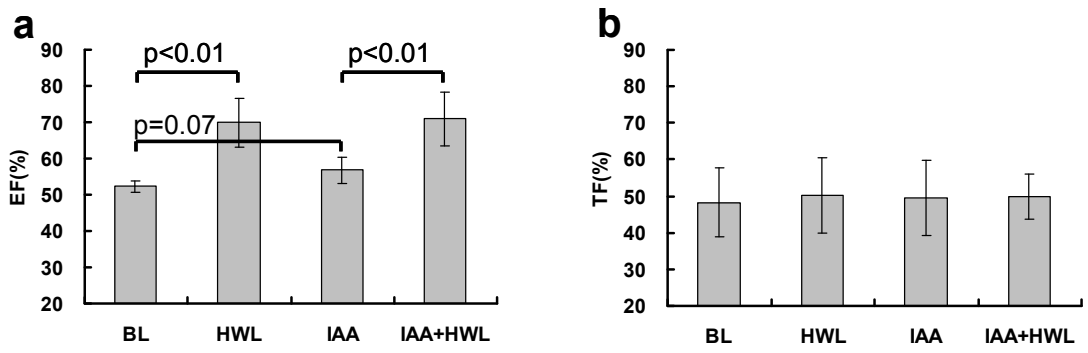

Figure 4.9 Preserved LV contractile function despite of CK inhibition. LV contractile function (a, ejection fraction, and b, systolic thickening fraction) in response to creatine kinase inhibition (IAA) under basal (BL) and high cardiac workload (HWL) conditions. Creatine kinase inhibition was achieved by iv infusion of iodoacetamide (IAA, 0.45 mmol/kg). HWL condition was achieved using catecholamine stimulation (Dopamine/Dobutamine, each of 10 μg/kg/min iv).

Taken together, these data demonstrate that LV contractile performance is maintained when the ATP production rate via CK is inhibited, suggesting existence of multiple and redundant ATP production systems in supporting the contractile apparatus' chemical energy need.

4.4.2 Rat Brain in vivo Studies

The non-invasive T_1^{nom} method is further verified on rat brain at 9.4T with measurements of the CK and ATPase activities at rest condition. As shown in Figure 4.10, there is no statistically significant difference between the k_f values measured by conventional (TR=9s, $\alpha=90^o$) and T_1^{nom} (TR=3s, $\alpha=45^o$) methods ($k_{f,CK}$: 0.26±0.04 vs 0.24±0.03, p=NS; $k_{f,ATPase}$: 0.17±0.06 vs 0.15±0.08, p=NS).

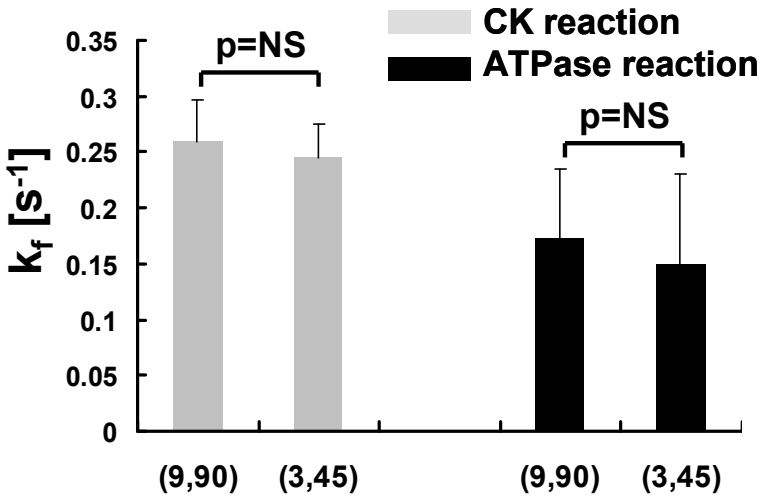

Figure 4.10 Consistent measurements from both conventional and T_1^{nom} methods on rat brain. CK (grey) and ATPase (black) activities were measured on rat brain using both conventional (TR=9s, α=90^o) and T_1^{nom} (TR=3s, α=45^o) steady-state MST methods (NEX=256). There is no statistical difference between the measurements. The T_1^{nom} and β (Equation [4.8]) for CK and ATPase reactions of rat brain at 9.4 T are: $T_{1,CK}^{nom}$ = 3.30 s, β_{CK}=1.00; $T_{1,ATPase}^{nom}$=3.50 s, β_{ATPase}=1.00. The parameters for calculating the T_1^{nom} and β are taken from reference [206]: pool size ratio of PCr : ATPγ : Pi = 1:0.55:0.14, intrinsic T_1 for PCr, ATPγ and Pi are 3.83, 1.24 and

4.5 Discussions

Intrinsically an insensitive MR-based method, MRS/MRI studies performed *in vivo* always struggle with the low SNR issues with respect to limited total scan time. It is especially the case when studying enzyme kinetics using conventional steady-state MST technique since fully relaxed spectra with (M_{ss}) and without saturation on ATPγ are required for k_f calculation. In this work we introduced a novel and simple method (T_1^{nom}) to quantify k_f under partial relaxation conditions, allowing steady-state MST experiments to be performed with arbitrary TR and flip

angle. The T_1^{nom} method features with extremely fast k_f measurement yet simple linear algorithm (Equation [4.8]) for quantification. In addition, the optimization strategy would significantly enhance the performance of T_1^{nom} method by minimizing the final k_f errors secondary to the sensitive to the flip angle accuracy. By necessity, the T_1^{nom} method together with the optimization strategy can greatly facilitate the *in vivo* enzyme kinetic studies that demand high spatial and resolution.

4.5.1 Versatility of T_1^{nom} Method

The linear relationship between M_c/M_s ratio and k_f is well maintained through out a large range of acquisition parameters (Figure 4.3). More extensive simulation suggested that this linear relationship holds in general regardless of pool size ratio or intrinsic T_1 values, suggesting T_1^{nom} method a versatile tool for kinetic studies independent of experimental setup.

In this study, the T_1^{nom} method is theoretically demonstrated based on the human brain study at 7 Tesla (three-site exchange model, PCr↔ATP↔Pi) and further experimentally verified on an *in vivo* swine heart model for measuring myocardial CK forward reaction rate constant at 9.4 Tesla (two-site model, PCr↔ATP). The two-site model is preferably employed for myocardial bioenergetic studies since the Pi resonance is largely overlapped by the 2,3-2,3-diphosphoglycerate peaks from blood and thus difficult to quantify unless spatial localization is employed [220]. When applied to the two-site exchange ATP↔Pi reaction (corresponding to Equations [4.3] and [4.6]) was ignored during the numerical simulation process (M_c/M_s vs k_f, Figure 4.3) for finding the T_1^{nom}

value. Therefore, the T_1^{nom} method-based k_f calculation is readily applicable to both two- and three- site models as supported by the good agreement between experimental and simulation results shown in Figure 4.7 and 4.10.

4.5.2 Validity of the Methodology

The T_1^{nom} method can be considered as an improved version of conventional steady-state MST technique and thus shares the same validity. Both of them rely on prior knowledge of intrinsic T_1 (T_1^{int}) values for k_f calculation. Fortunately, the extensive previous studies on CK and ATPase kinetics have suggested that the intrinsic T_1 is constant among subjects regardless of physiological and pathologic conditions [122, 137, 205, 206, 211-213]. This is consistent with the observation in this study that $T_{1,PCr}^{int}$ is a constant among subjects and independent of reaction rate change throughout CK inhibition process. Nevertheless, for specific studies where reliable T_1^{int} values are not available, direct measurement of T_1^{int} can be performed with other established methods[208], such as progressive MST (see example shown in Figure 4.5). In practice, intrinsic T_1 can be measured with a few healthy subjects (for patients studies), before interventions (for intervention studies), or without spatial discrimination (for spatially resolved studies) followed by k_f measurements using T_1^{nom} method. Notice that the major merit of T_1^{nom} method is that it allows extremely fast k_f measurement (arbitrary TR and α) such that a large number of *in vivo* enzyme kinetics studies with high spatial or temporal resolution would become feasible.

The T_1^{nom} method is highly robust to the variation of pool size ratio of metabolites, such as PCr/ATP ratio for CK reaction and Pi/ATP ratio for ATPase

reaction. For the acquisition parameters within the optimized region as shown in Figure 4.4g-h, the relative k_f measurement error due to a variation of pool size ratios of metabolite is less than 1/8 of the variation level itself, i.e., a change of PCr/ATP ratio of 40% would result only a 5% of k_f measurement error using the T_1^{nom} method. Finally, in case of large change of pool size ratios of metabolites, iteration approach can be employed to correct for the originally assumed pool ratio based on M_c measurement (Figure 4.11). The iteration approach is based the assumption that the pool size ratio change is proportionally reflected in the magnetization (M_c) ratio measured in control spectra as long as the intrinsic T_1s the two statuses are the same:

$$\frac{M_{0,PCr}:M_{0,ATP\gamma}:M_{0,Pi}\big|_{status1}}{M'_{0,PCr}:M'_{0,ATP\gamma}:M'_{0,Pi}\big|_{status2}} \approx \frac{M_{c,PCr}:M_{c,ATP\gamma}:M_{c,Pi}\big|_{status1}}{M'_{c,PCr}:M'_{c,ATP\gamma}:M'_{c,Pi}\big|_{status2}} \quad [4.15]$$

Numerical simulation suggested a correction precision of >95% for Equation [4.15] with wide range of parameters (CK study of human brain at 7 Tesla [211], $k_{f,CK}$= 0.15~0.6 s^{-1}, TR=0.4~8 s, α=5~90^o). Equation [4.15] is useful for obtaining the metabolites' pool size ratio in the absence of fully relaxed measurements, which is highly valuable since the pool size ratio such as PCr/ATP has been widely accepted as a useful index for the bioenergetic status [105, 221]. Therefore, based on Equation [4.8] and [4.15], a complete energetic study of both pool size ratio of metabolites and enzyme activity level can be performed without fully relaxed measurements.

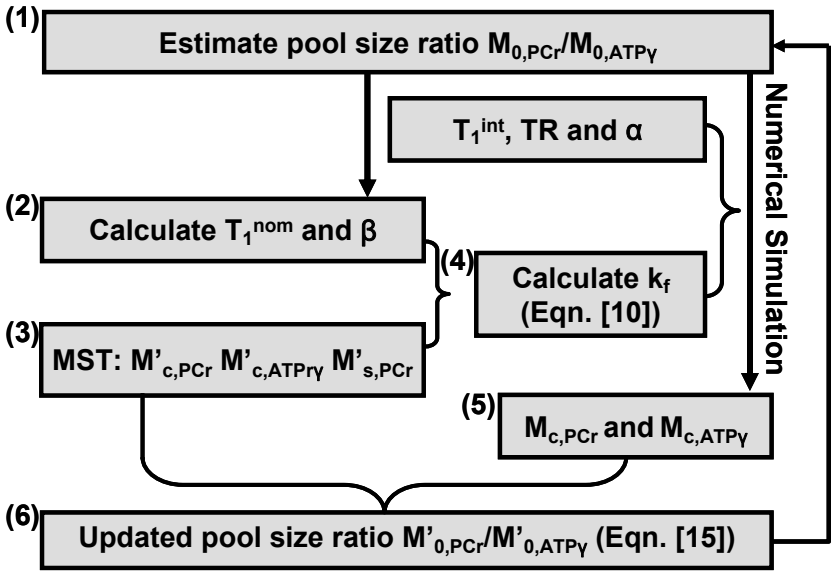

Figure 4.11 Iteration approach for finding the pool size ratio without fully relaxed measurements.

(1) Make an initial estimation of pool size ratio of metabolites ($M_{0,PCr}/M_{0,ATP\gamma}$), can be either based on literature, previous experiences or baseline measurement (for intervention studies).

(2) According to intrinsic T_1 values and the acquisition parameters (TR and α), calculate the T_1^{nom} and β using numerical simulation.

(3) Perform steady-state MST experiment with the select TR and α to get $M'_{c,PCr}$, $M'_{c,ATP\gamma}$ and $M'_{s,PCr}$ measurements.

(4) Calculate k_f based on $M'_{c,PCr}$ and $M'_{s,PCr}$ using T_1^{nom} method (Equation [4.8]).

(5) Feed the k_f value into numerical simulation, and calculate the simulated control spectrum ($M_{c,PCr}$ and $M_{c,ATP\gamma}$).

(6) Update the initial estimation of pool size ratios of metabolites based on Equation [4.15], the new pool size ratio of metabolites is:

$M'_{0,PCr}/M'_{0,ATP\gamma} = (M_{0,PCr}/M_{0,ATP\gamma})*(M'_{c,PCr}/M'_{c,ATP\gamma})/(M_{c,PCr}/M_{c,ATP\gamma})$.

The iteration stops when simulated $M_{c,PCr}/M_{c,ATP\gamma}$ is close enough to $M'_{c,PCr}/M'_{c,ATP\gamma}$.

4.5.3 Enhanced Performance from Optimization Strategy

The performance of k_f measurement using the T_1^{nom} method would be greatly enhanced by the optimization strategy, which is based on the k_f error analysis to generate the best acquisition parameter range (TR and α, that are most relevant to the longitudinal relaxation processing).

Type 1 error as defined by Equation [4.11] represents the accuracy of k_f calculation using the T_1^{nom} method. As shown in Figure 4.4a-b, the type 1 error for human brain studies at 7 Tesla is below 1% for most acquisition conditions. Similar type 1 error levels were observed from numerical simulations with parameters that are characteristic of heart and skeletal muscle. Those simulation results again demonstrated the versatility of T_1^{nom} method for measuring enzyme kinetics on various organs.

The type 2 error specifically addresses the spectral SNR issue. For MR experiment with partial relaxation, the spectral SNR per unit acquisition time would be maximized if the flip angle is chosen at the Ernst angle that is determined by TR and spin's longitudinal relaxation time. When chemical exchange is involved, the Ernst angle also depends on the reaction rate. Therefore, the Ernst angle for control and saturated spectrum would be different. However, applying different flip angles for M_c and M_s measurements would the spectrum comparison less intuitive and the k_f calculation more prone to flip angle inaccuracy. In current approach, instead, both spectra are acquired with a same flip angle that is globally optimized according to error propagation theory (Equation [4.13]), Since the acquisition parameters are identical for both M_c and

M_s spectra, any measurement error due to flip angle variation would be cancelled out in Equation [4.8] for k_f calculation and the only residual effect would be the change of T_1^{nom} value, which is taken into account as the type 3 error. Even though none of the M_c or M_s measurements is acquired exactly at its Ernst angle, the overall performance from this globally optimized flip angle is still substantially better than the conventional steady-state MST. Taking human brain studies at 7 Tesla for instance (same parameter as used in Figure 4.4), the T_1^{nom} method can easily achieve a level of <1% type 1 error. The same type 1 error level would require a TR of 16 sec for the conventional MST methods (99% full relaxation, $\alpha=90^o$). Should such an experiment be performed under an optimized condition using the T_1^{nom} method (e.g. TR=2 sec, $\alpha=45^o$), an 88% reduction of total acquisition time could be achieved assuming a same number of signal averaging (NEX).

Type 3 error deals with the residual effects of flip angle inaccuracy on the final k_f calculation error. As demonstrated in Figure 4.4e-f, the spin system becomes more robust against flip angle variation as flip angle decreases or TR increases. This result is consistent with the previous simulation results showing that T_1^{nom} approaches to T_1^{int} as flip angle decreases or TR increases (Figure 4.3). Therefore, based on the analysis of type 3 error (Figure 4.4e-f) we can compensate the impact of flip angle variation to an arbitrary level at an expense of reduced SNR per unit time. This is advantageous over some other rapid saturation transfer methods which employ multiple flip angles for calculating the k_f and thus more vulnerable to flip angle variation, such as FAST method [203].

In the present discussion, the parameter optimization was performed with arbitrary cutoff levels set to each type of k_f error. Bear in mind that for specific studies, different cutoff values could be used for more appropriate optimization. For example, if the final k_f error is mainly contributed from flip angle variation, whereas SNR is not an issue (such as experiments with surface coil), a smaller K_{flip} cutoff value could be employed accordingly.

The superior performance of the T_1^{nom} method is demonstrated by the transmurally differentiated measurement of $k_{f,CK}$ (Figure 4.8). The total data acquisition time using T_1^{nom} method in combination of 1D-CSI sequence (2 sets of spectra, 17 phase encoding steps, NEX=8, TR=3 sec) is 13.6 minutes. In contrast, a similar transmurally differentiated $k_{f,CK}$ measurement performed by Robitaille *et al.* using a conventional saturation transfer method took 153.6 min (8 sets of spectra, 18 phase encoding steps, NEX=8 and TR=8 sec) to accomplish the data acquisition [184]. Therefore, the present study demonstrates that using T_1^{nom} method results in a reduction of data acquisition time by 91.2% as compared to the conventional saturation transfer method.

4.5.4 LV Contractile Function in Relation to CK Inhibition

Upon inhibition of creatine kinase via iodoacetamide infusion, the systemic hemodynamic did not change within an observation window of 30 min (Table 4.2), the LV ejection fraction and thickening fraction were not impaired (Figure 4.9), the high energy phosphate PCr/ATP ratio was preserved (Table 4.3), and the inorganic phosphate (Pi) level did not increase (Figure 4.6). Collectively, the

present study demonstrate for the first time that a normal LV chamber contractile function can be maintained in the presence of complete inhibition of CK activity in normal *in vivo* heart under basal and high cardiac workstates. This finding is surprising, and raises a significant question of what a significant role CK plays in the cascade of ATP production, transportation and utilization. The severity of CK kinetics change is related to the chronic cardiac pathologic changes such as severity of the LV hypertrophy or LV dysfunction [137, 142, 174, 183, 205]. However, the mechanisms of these relationships are still unknown. The results of the present study demonstrate a different concept. Namely, in normal heart in vivo within a 30 min-observation window, an **acute** severe inhibition of ATP production rate via system does not impair the LV regional or global contractile function. The finding of normal LV chamber function with complete inhibition of CK activity in the present study is in agreement with the previous observation of using engineered mice, which demonstrated a normal growth and LV chamber function in mice with double knockout of the muscle and mitochondrial isoforms (M/MtCK-/- mice) [146]. Taken together, these data suggest that in normal heart under *in vivo* conditions, redundant supporting systems exist to maintain an important organ function. These data also suggest that in the failing hearts that are usually severely hypertrophied, the redundant supporting systems such as CK, mitochondrial electron transport system and ATPase, may all be impaired. Consequently, the severity of the alterations of each of these systems contribute and is related to severity of the LV dysfunction such as being observed earlier [104, 142, 152, 183, 222].

In summary, we have demonstrated a novel steady-state magnetization

saturation transfer method (T_1^{nom}) together with an optimization strategy that allows accurate k_f quantification under partially relaxed acquisition conditions. new method features an extremely fast k_f measurement yet simple linear algorithm for quantification. This method would enable broad applications for *in vivo* enzyme kinetic studies that require high spatial or temporal resolution. Using this novel NMR methods and an established swine model, these data demonstrate that inhibition of CK activity does not limit LV chamber function at basal cardiac workstates in the *in vivo* heart.

Chapter 5

SUMMARY AND FUTURE WORK

5.1 Summary

Intrinsically a lethal and irreversible clinical disease, cardiovascular disease (CVD) accounted for more deaths than any other cause in the United States. Therefore, it is imperative to develop new efficient treatments for ischemic heart disease as well as more powerful tools to understand the mechanism underlying the irreversible negative remodeling upon cardiac damage.

The dissertation is related to heart disease in both basic scientific and pre-clinic respects, which is summarized as follows:

1. Using both large (swine) and small (rodent) animal models with ischemic heart disease, we examined the functional improvement of enhanced delivery of combined human embryonic stem cell-derived endothelial cells and smooth muscle cells with a fibrin 3D porous scaffold biomatrix. The combination of stem

cell biology and tissue engineering has resulted in significant improvement of regional and global left ventricle function as compared to untreated animals, demonstrating a promising therapeutic potential of using this cell type and the novel mode of delivery

2. Using in vivo $^{1}H/^{31}P$ magnetic resonance techniques, cardiac energetics can be studied non-invasively. However, its wide application has been compromised by the long acquisition time (hours). Based on numerical simulation and experimental validation on both pig heart and rat brain, we have proposed novel methods for studying energetics in an unparalleled fast way (> 10 folder faster compared to conventional methods). With the help of these novel strategies, broad applications for in vivo bioenergetics studies requiring high spatial or temporal resolution would become feasible.

5.2 Future Work

Following the project of cardiac repair using human embryonic stem cell transplantation, we are going to examine the therapeutic potential of induced pluripotent stem cells (iPSCs). This cell type is considered as a greatest milestone in cellular biology because it is the only cell source that is both pluripotent and totally avoids ethical issues (i.e. the patients' own cells can be reprogrammed into heart cells for cardiac repair). Shown in Figure 5.1 is the preliminary experiment where iPSC-derived vascular cells are transplanted to infracted pig heart via fibrin patch.

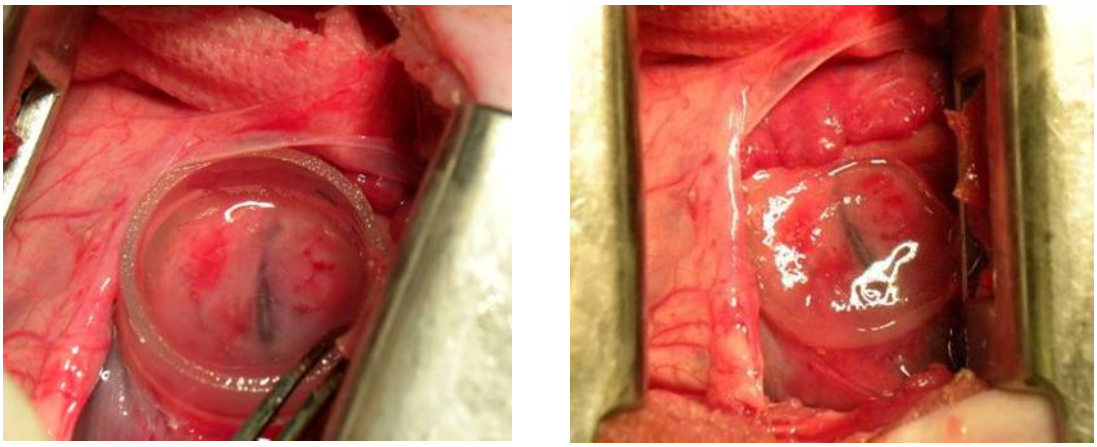

Figure 5.1 Stem cell transplantation using fibrin patch-based delivery. Stem cells and fibrin biomaterials were co-injected onto the ischemic region of a pig heart (left panel) and form a “patch” (right panel).

Another direction related to stem cell therapy is to further modify the fibrin biomaterial system such that it not only provides biocompatible scaffold for transplanted stem cells to seed but also is capable of controlled release of cytokines, thus further enhancing the efficacy of stem cell therapy. Shown in Figure 5.2 is a pilot experiment to compare the cell engraftment rate between fibrin patch-based delivery and direct intramyocardial injection. The stem cell transplantation with fibrin patch-based delivery demonstrated a significantly higher cell retention rate as compared to direct injection. The higher cell engraftment rate from fibrin patch could be detected as early as 1 hour and persisted up to 2 weeks ($p<0.05$). However, even with fibrin patch-based delivery, most transplanted cells died over one month follow-up. The cell loss may be related to extensive inflammation of the host organ secondary to cardiac Therefore, by devising the fibrin patch into a “dual delivery system” which can control release pro-survival growth factors, such as IGF-1, we would further

increase the efficacy of stem cell therapy.

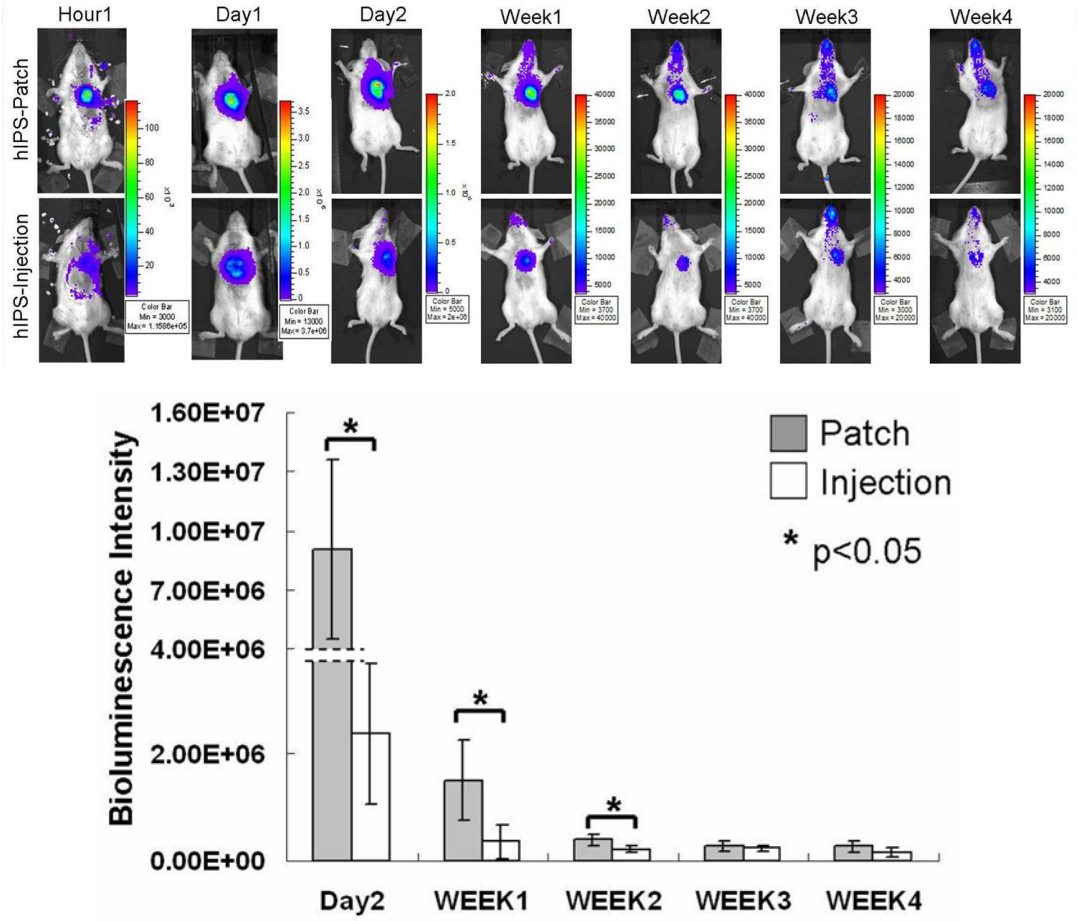

Figure 5.2 Comparison of cell engraftment rate between direct injection and fibrin patch. hiPSCs-derived vascular progenitor cells were transplanted to infracted immuno-dificient mouse hearts and cell engraftment up to 4 weeks was examined via in vivo bioluminescent imaging (upper panel). Integral of photon intensity in the bioluminescent images was utilized to quantify the cell engraftment rate (lower panel).

The new magnetic resonance methods would enable a wide range of in vivo bioenergetic studies with high temporal and spatial resolution. One promising research project is to combine the novel methods with the state-of-the-art cardiac MRI techniques to investigate the relationship between cardiac energetic abnormality and the cardiac contractile dysfunction in a spatially and temporally

resolved fashion. The project would require a totally non-invasive MRI/MRS modality at ultra-high-field, featuring a multi-channel external coil, multi-multi-transmission/receiving techniques, and spatial localization sequences. A prototype of the multi-channel external chest coil for cardiac MRI/MRS study at 9.4 Tesla is shown in Figure 5.3. This study will provide unprecedented insight the mechanism of heart failure development in biochemical level and may even provide valuable energetic markers for early diagnostic of ischemic heart

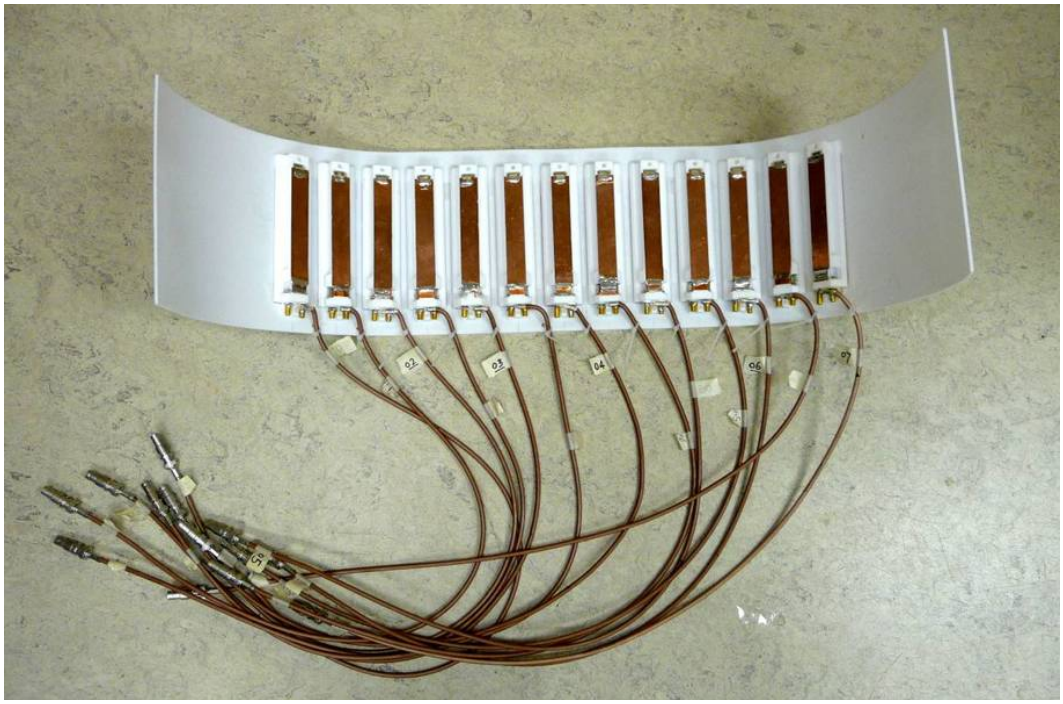

Figure 5.3 A 7-channel ^{31}P/6-channel ^{1}H external chest coil for non-invasive cardiac MRI/MRS study at 9.4 Tesla.

Chapter 6

APPENDIX

This appendix serves to demonstrate that the $d_{1,opt}$ novel magnetization saturation transfer (MST) strategy is compatible with spatial localization of 3D-ISIS pulse sequence for non-invasive measurement of ATP production rate via CK. The total data acquisition time was decreased by 76% compared to conventional MST methods.

6.1 Appendix Methods

The experiments were performed using a rat brain model and details of animal preparation for ^{31}P MR spectroscopy (MRS) have been described previously [202]. Briefly, rats were anaesthetized via inhalation of 2% isoflurane, intubated and ventilated by a mechanical respirator. The femoral artery and vein were catheterized for blood sampling and monitoring of physiological parameters. The rectal temperatures were maintained at 37±1°C throughout the experiment with an external heating patch.

All in vivo ^{31}P MRS experiments were conducted on a 9.4T horizontal animal magnet (Magnex Scientific) interfaced with a Varian INOVA console. A multinuclear radiofrequency (RF) surface-coil probe consisting of a butterfly-butterfly-shaped ^{1}H surface coil and an elliptical-shaped ^{31}P surface coil with of 12 mm and 10 mm was used. The ^{1}H surface coil was used to acquire anatomical images of the brain to guide choosing the regions of interest (ROIs)

and for shimming magnetic field homogeneity. For ^{31}P spectroscopy, a 3D-ISIS pulse sequence was used for spatial localization. BISTRO pulse train was used achieve frequency selective saturation and an adiabatic half passage (AHP) was used for readout. In order to help visualize whether the spatial localization was adequate, two capillaries filled with 10% phosphoric acid were inserted into the skeletal muscle surrounding the skull.

$d_{1,opt}$ strategy was employed for $M_{ss,PCr}$ measurement. The parameters used for calculating $d_{1,opt}$ and $d_{2,opt}$ were from literature [202], and summarized in Table 6.1. Those parameters gave rise to a $d_{1,opt}$ value of 2.1 sec and $d_{2,opt}$ of 3.4 sec. For $T_{1,PCr}^{app}$ measurement, a short-TR (TR=1.4 sec) spectrum with continuous saturation of ATPγ was performed and used in combination with $M_{ss,PCr}$ measurement to calculate the $T_{1,PCr}^{app}$ according to equation [3.10].

Table 6.1 Parameters used for $d_{1,opt}$ and $d_{2,opt}$ calculation

Parameters	$T_{1,PCr}^{int}$, [s]	$T_{1,ATP\gamma}^{int}$, [s]	k_f, [s^{-1}]
Values [202]	4.0	1.33	0.15~0.6

6.2 Appendix Results

6.2.1 Spatial Localization of 3D-ISIS Sequence

A demonstration of spatial localization of 3D-ISIS pulse sequence is shown in Figure 6.1. The spatial localization from 3D-ISIS pulse sequence is demonstrated

by the following observations: (1) no detectable phantom signal in brain region (spectrum a); (2) the obvious low and high PCr-to-ATP ratios (PCr/ATP) in a and b that are characteristic of brain and skeletal muscle, respectively.

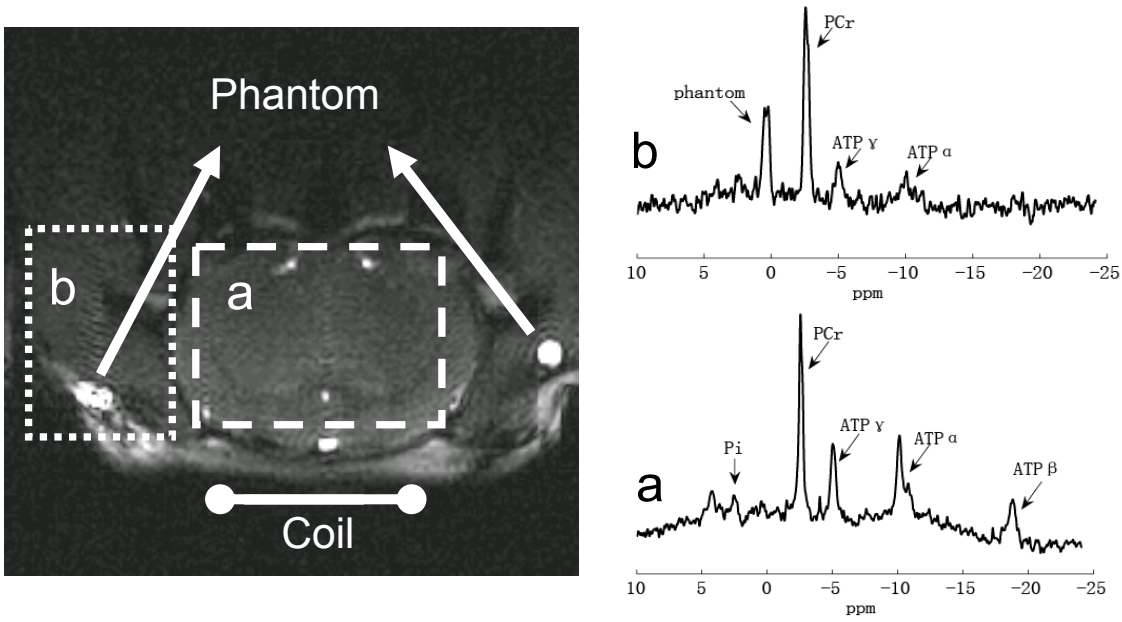

Figure 6.1 Demonstration of spatial localization from 3D-ISIS pulse sequence on rat brain. Localized spectra (TR=9 sec, nt=128) from brain (a) and skeletal muscle (b) were obtained with corresponding ROIs shown on top of the axial image of rat brain (turbo FLASH sequence). Each spectrum was acquired with 19.2 min. The smaller SNR of muscle spectrum is due to farther distance from the surface coil that was positioned next to brain region.

6.2.2 Validation of Novel MST Strategy in Rat Brain Model

Firstly, the $d_{1,opt}$ strategy was validated. The spectra with $d_{1,opt}$ and conventional strategies for $M_{0,PCr}$ and $M_{ss,PCr}$ measurements are shown in Figure 6.2. There was no detectable difference in $M_{ss,PCr}$ measurement between the and the conventional strategies (Figure 6.2 Panel b). An extra spectrum (Figure 6.2, b2) with TR=$d_{1,opt}$ and saturation pulse off was also acquired to further

confirm the $d_{1,opt}$ strategy. Spectrum b2 generated a PCr signal very close to $M_{ss,PCr}$ measured in b1 and b3, which is consistent with our $d_{1,opt}$ hypothesis that $M_{PCr}(d_{1,opt})\approx M_{ss,PCr}$. For $M_{ss,PCr}$ measurement (Figure 6.2, Panel a), the spillover effect of BISTRO saturation pulse train on PCr peak was again negligible.

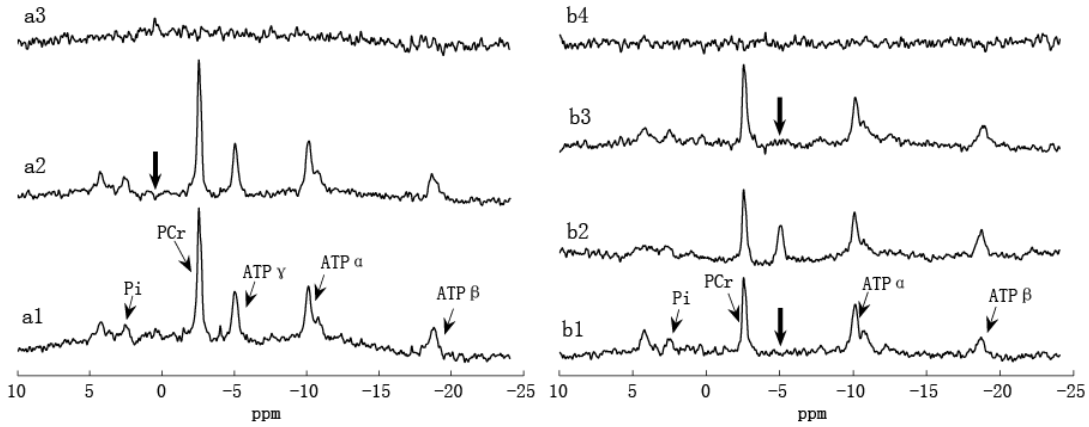

Figure 6.2 Experimental validation of $d_{1,opt}$ strategy on rat brain. All spectra were acquired with 3D-ISIS pulse sequence and 128 averaged FIDs. a1 is $M_{0,PCr}$ measurement (TR=9 sec); a2 is the control spectrum with saturation pulse set downfield from PCr symmetrically opposite from ATPγ; spectrum a3=a1-a2, from which we can see there is no spillover effect of the BISTRO saturation pulse. Spectrum b1 and b3 are $M_{ss,PCr}$ measurements using conventional (d_1=9 sec, d_2= 8 sec) and novel ($d_1=d_{1,opt}$=2.1 sec, $d2=d_{2,opt}$=3.4 sec) strategies, respectively. Spectrum b2 was acquired with TR= $d_{1,opt}$=2.1 sec and saturation pulse off. Spectrum b4 =b2-b1. The bold arrows indicate the frequency of saturation pulses. Total acquisition times for spectra a1, a2, b1, b2 and b3 were 19.2, 36.3, 36.3, 4.5, and 11.7 min, respectively.

The $T_{1,PCr}^{app}$ measurement using the novel strategy is shown in Figure 6.3. Here a two-spectrum method using equation [3.10] was employed for $T_{1,PCr}^{app}$ calculation. All the measurements obtained from the novel strategy are summarized in Table 6.2 along with data obtained from a previous study [202] for comparison. The novel strategy generated a mean k_f value of 0.22±0.02 sec^{-1}

from 6 rats which is similar to the reported value of 0.24±0.02 sec^{-1} under the same condition. Moreover, a 76% reduction in total acquisition time was achieved (43 min for novel strategy vs 180 min for conventional strategy [202]).

In summary, we have successfully demonstrated the compatibility of the novel MST strategy with the 3D-ISIS spatial localization and an external coil for completely non-invasive MST measurement. The strategy was validated using a rat brain model, which generate a k_f measurement similar to the reported value with only 24% of total data acquisition time as compared to conventional approach.

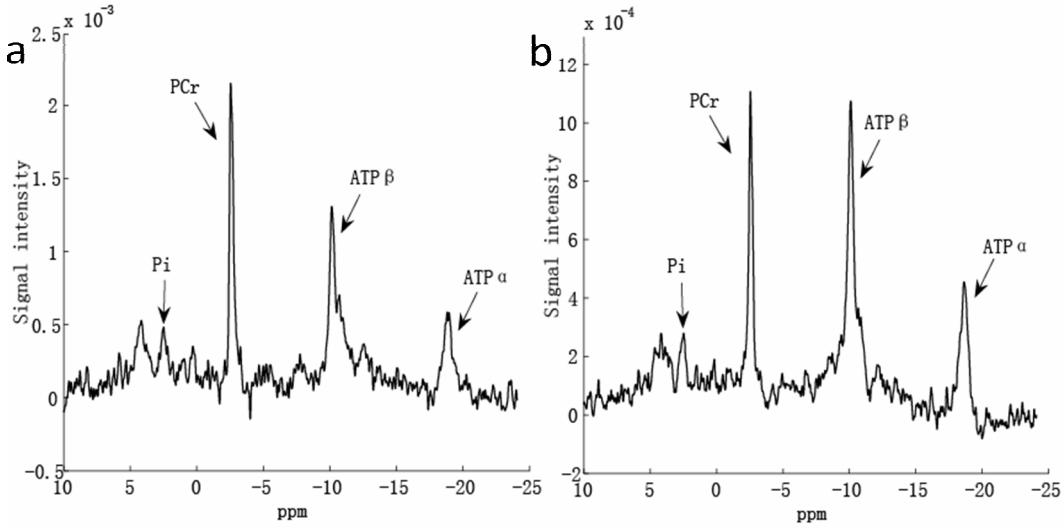

Figure 6.3 $T_{1,PCr}^{app}$ measurement from two spectra. Spectrum a is the $M_{ss,PCr}$ measurement (same as spectrum b3 in Figure 3.9). Spectrum b was acquired with ATPγ continuously saturated and relatively shorter TR (TR=1.4 sec, nt=512). Total acquisition times for spectra a and b were 11.7 and 11.9 min, respectively. $T_{1,PCr}^{app}$ is calculated using equation [3.10].

Table 6.2 Rat brain CK MST measured by *in vivo* ^{31}P MRS

Source	$T_{1,PCr}^{app}$ [sec]	$T_{1,PCr}^{int}$ [sec]	k_f, [sec^{-1}]	time [min]
This work (n=6)	1.90±0.09	3.3±0.3	0.22±0.02	43[a]
Literature [202]	NA	3.68±0.50	0.24±0.02	180[b]

[a]: Acquisition time is based on TR=9 sec for $M_{0,PCr}$ measurement, TR=5.5 for $M_{ss,PCr}$ measurement and TR=1.4 sec for $T_{1,PCr}^{app}$ measurement. Both $M_{0,PCr}$ and $M_{ss,PCr}$ measurements were acquired with 128 averaged FIDs, while short-TR measurement was acquired with 512 averaged FIDs for comparable SNR.

[b]: Acquisition time is based on mean TR of 12 sec, 5-point progressive saturation transfer experiment for $T_{1,PCr}^{app}$ measurement plus TR=9 sec for $M_{0,PCr}$ and TR=15 sec for $M_{ss,PCr}$ measurement. All measurements were obtained with from 128 averaged FIDs.

BIBLIOGRAPHY

1. Rosamond W, Flegal K, Furie K, Go A, Greenlund K, Haase N, Hailpern SM, Ho M, Howard V, Kissela B, Kittner S, Lloyd-Jones D, McDermott M, Meigs J, Moy C, Nichol G, O'Donnell C, Roger V, Sorlie P, Steinberger J, Thom T, Wilson M, Hong Y. Heart disease and stroke statistics--2008 update: a report from the American Heart Association Statistics Committee and Stroke Statistics Subcommittee. *Circulation.* 2008;117(4):e25-146.

2. Miniati DN, Robbins RC. Heart transplantation: a thirty-year perspective. *Annu Rev Med.* 2002;53:189-205.

3. Boersma E, Mercado N, Poldermans D, Gardien M, Vos J, Simoons ML. Acute myocardial infarction. *Lancet.* 2003;361(9360):847-858.

4. Weissman IL. Translating stem and progenitor cell biology to the clinic: barriers and opportunities. *Science.* 2000;287(5457):1442-1446.

5. Sunkomat JN, Gaballa MA. Stem cell therapy in ischemic heart disease. *Cardiovasc Drug Rev.* 2003;21(4):327-342.

6. Bishop AE, Buttery LD, Polak JM. Embryonic stem cells. *J Pathol.* 2002;197(4):424-429.

7. Thomson JA, Itskovitz-Eldor J, Shapiro SS, Waknitz MA, Swiergiel JJ, Marshall VS, Jones JM. Embryonic stem cell lines derived from human blastocysts. *Science.* 1998;282(5391):1145-1147.

8. Shamblott MJ, Axelman J, Littlefield JW, Blumenthal PD, Huggins GR, Cui Y, Cheng L, Gearhart JD. Human embryonic germ cell derivatives express a broad range of developmentally distinct markers and proliferate extensively in vitro. *Proceedings of the National Academy of Sciences of the United States of America.* 2001;98(1):113-118.

9. Evans MJ, Kaufman MH. Establishment in culture of pluripotential cells from mouse embryos. *Nature.* 1981;292(5819):154-156.

10. Martin GR. Isolation of a pluripotent cell line from early mouse embryos cultured in medium conditioned by teratocarcinoma stem cells. *Proceedings of the National Academy of Sciences of the United States of America.* 1981;78(12):7634-7638.

11. Reubinoff BE, Pera MF, Fong CY, Trounson A, Bongso A. Embryonic stem cell lines from human blastocysts: somatic differentiation in vitro. *Nat Biotechnol.* 2000;18(4):399-404.

12. Wobus AM, Holzhausen H, Jakel P, Schoneich J. Characterization of a pluripotent stem cell line derived from a mouse embryo. *Exp Cell Res.* 1984;152(1):212-219.

13. Behfar A, Perez-Terzic C, Faustino RS, Arrell DK, Hodgson DM, Yamada S, Puceat M, Niederlander N, Alekseev AE, Zingman LV, Terzic A. Cardiopoietic programming of embryonic stem cells for tumor-free heart repair. *J Exp Med.* 2007;204(2):405-420.

14. Janssens S. Human embryonic stem cells for cardiac repair: the focus is on refined selection and cardiopoietic programming. *Heart.* 2007;93(10):1173-1174.

15. Klug MG, Soonpaa MH, Koh GY, Field LJ. Genetically selected cardiomyocytes from differentiating embronic stem cells form stable intracardiac grafts. *The Journal of clinical investigation.* 1996;98(1):216-224.

16. Bhatia M, Wang JC, Kapp U, Bonnet D, Dick JE. Purification of primitive human hematopoietic cells capable of repopulating immune-deficient mice. *Proceedings of the National Academy of Sciences of the United States of America.* 1997;94(10):5320-5325.

17. Czyz J, Wobus A. Embryonic stem cell differentiation: the role of extracellular factors. *Differentiation.* 2001;68(4-5):167-174.

18. Kehat I, Kenyagin-Karsenti D, Snir M, Segev H, Amit M, Gepstein A, Livne E, Binah O, Itskovitz-Eldor J, Gepstein L. Human embryonic stem cells can differentiate into myocytes with structural and functional properties of cardiomyocytes. *The Journal of clinical investigation.* 2001;108(3):407-414.

19. Spangrude GJ, Heimfeld S, Weissman IL. Purification and characterization of mouse hematopoietic stem cells. *Science.* 1988;241(4861):58-62.

20. Laflamme MA, Chen KY, Naumova AV, Muskheli V, Fugate JA, Dupras SK, Reinecke H, Xu C, Hassanipour M, Police S, O'Sullivan C, Collins L, Chen Y, Minami E, Gill EA, Ueno S, Yuan C, Gold J, Murry CE. Cardiomyocytes derived from human embryonic stem cells in pro-survival factors enhance function of infarcted rat hearts. *Nat Biotechnol.* 2007;25(9):1015-1024.

21. Bianco P, Gehron Robey P. Marrow stromal stem cells. *The Journal of clinical investigation.* 2000;105(12):1663-1668.

22. Kondo M, Wagers AJ, Manz MG, Prohaska SS, Scherer DC, Beilhack GF, Shizuru JA, Weissman IL. Biology of hematopoietic stem cells and progenitors: implications for clinical application. *Annu Rev Immunol.* 2003;21:759-806.

23. Caplan AI. Mesenchymal stem cells. *J Orthop Res.* 1991;9(5):641-650.

24. Toma C, Pittenger MF, Cahill KS, Byrne BJ, Kessler PD. Human mesenchymal stem cells differentiate to a cardiomyocyte phenotype in the adult murine heart. *Circulation.* 2002;105(1):93-98.

25. Makino S, Fukuda K, Miyoshi S, Konishi F, Kodama H, Pan J, Sano M, Takahashi T, Hori S, Abe H, Hata J, Umezawa A, Ogawa S.

Cardiomyocytes can be generated from marrow stromal cells in vitro. *J. Clin. Invest.* 1999;103:697-705.

26. Tomita S, Li RK, Weisel RD, Mickle DA, Kim EJ, Sakai T, Jia ZQ. Autologous transplantation of bone marrow cells improves damaged heart function. *Circulation.* 1999;100(19 Suppl):II247-256.

27. Orlic D, Kajstura J, Chimenti S, Jakoniuk I, Anderson SM, Li B, Pickel J, McKay R, Nadal-Ginard B, Bodine DM, Leri A, Anversa P. Bone marrow cells regenerate infarcted myocardium. *Nature.* 2001;410(6829):701-705.

28. Min JY, Sullivan MF, Yang Y, Zhang JP, Converso KL, Morgan JP, Xiao YF. Significant improvement of heart function by cotransplantation of human mesenchymal stem cells and fetal cardiomyocytes in postinfarcted pigs. *Ann Thorac Surg.* 2002;74(5):1568-1575.

29. Shake JG, Gruber PJ, Baumgartner WA, Senechal G, Meyers J, Redmond JM, Pittenger MF, Martin BJ. Mesenchymal stem cell implantation in a swine myocardial infarct model: engraftment and functional effects. *Ann Thorac Surg.* 2002;73(6):1919-1925; discussion 1926.

30. Liu J, Hu Q, Wang Z, Xu C, Wang X, Gong G, Mansoor A, Lee J, Hou M, Zeng L, Zhang JR, Jerosch-Herold M, Guo T, Bache RJ, Zhang J. Autologous stem cell transplantation for myocardial repair. *Am J Physiol Heart Circ Physiol.* 2004;287(2):H501-511.

31. Nakamura Y, Wang X, Xu C, Asakura A, Yoshiyama M, From AH, Zhang J. Xenotransplantation of long-term-cultured swine bone marrow-derived mesenchymal stem cells. *Stem Cells.* 2007;25(3):612-620.

32. Anversa P, Nadal-Ginard B. Myocyte renewal and ventricular remodelling. *Nature.* 2002;415(6868):240-243.

33. Beltrami AP, Urbanek K, Kajstura J, Yan SM, Finato N, Bussani R, Nadal-Ginard B, Silvestri F, Leri A, Beltrami CA, Anversa P. Evidence that human cardiac myocytes divide after myocardial infarction. *The New England journal of medicine.* 2001;344(23):1750-1757.

34. Urbanek K, Quaini F, Tasca G, Torella D, Castaldo C, Nadal-Ginard B, Leri A, Kajstura J, Quaini E, Anversa P. Intense myocyte formation from cardiac stem cells in human cardiac hypertrophy. *Proceedings of the National Academy of Sciences of the United States of America.* 2003;100(18):10440-10445.

35. Beltrami AP, Barlucchi L, Torella D, Baker M, Limana F, Chimenti S, Kasahara H, Rota M, Musso E, Urbanek K, Leri A, Kajstura J, Nadal-Ginard B, Anversa P. Adult cardiac stem cells are multipotent and support myocardial regeneration. *Cell.* 2003;114(6):763-776.

36. Oh H, Bradfute SB, Gallardo TD, Nakamura T, Gaussin V, Mishina Y, Pocius J, Michael LH, Behringer RR, Garry DJ, Entman ML, Schneider MD. Cardiac progenitor cells from adult myocardium: homing, differentiation, and fusion after infarction. *Proceedings of the National*

Academy of Sciences of the United States of America. 2003;100(21):12313-12318.

37. Martin CM, Meeson AP, Robertson SM, Hawke TJ, Richardson JA, Bates S, Goetsch SC, Gallardo TD, Garry DJ. Persistent expression of the ATP-binding cassette transporter, Abcg2, identifies cardiac SP cells in the developing and adult heart. *Dev Biol.* 2004;265(1):262-275.

38. Pfister O, Mouquet F, Jain M, Summer R, Helmes M, Fine A, Colucci WS, Liao R. CD31- but Not CD31+ cardiac side population cells exhibit functional cardiomyogenic differentiation. *Circulation research.* 2005;97(1):52-61.

39. Wang X, Hu Q, Nakamura Y, Lee J, Zhang G, From AH, Zhang J. The role of the sca-1+/CD31- cardiac progenitor cell population in postinfarction left ventricular remodeling. *Stem Cells.* 2006;24(7):1779-1788.

40. Hosoda T, Kajstura J, Leri A, Anversa P. Mechanisms of myocardial regeneration. *Circ J.*74(1):13-17.

41. Leri A, Kajstura J, Anversa P. Cardiac stem cells and mechanisms of myocardial regeneration. *Physiological reviews.* 2005;85(4):1373-1416.

42. Takahashi K, Tanabe K, Ohnuki M, Narita M, Ichisaka T, Tomoda K, Yamanaka S. Induction of pluripotent stem cells from adult human fibroblasts by defined factors. *Cell.* 2007;131(5):861-872.

43. Okita K, Ichisaka T, Yamanaka S. Generation of germline-competent induced pluripotent stem cells. *Nature.* 2007;448(7151):313-317.

44. Wernig M, Meissner A, Foreman R, Brambrink T, Ku M, Hochedlinger K, Bernstein BE, Jaenisch R. In vitro reprogramming of fibroblasts into a pluripotent ES-cell-like state. *Nature.* 2007;448(7151):318-324.

45. Maherali N, Sridharan R, Xie W, Utikal J, Eminli S, Arnold K, Stadtfeld M, Yachechko R, Tchieu J, Jaenisch R, Plath K, Hochedlinger K. Directly reprogrammed fibroblasts show global epigenetic remodeling and widespread tissue contribution. *Cell Stem Cell.* 2007;1(1):55-70.

46. Yu J, Vodyanik MA, Smuga-Otto K, Antosiewicz-Bourget J, Frane JL, Tian S, Nie J, Jonsdottir GA, Ruotti V, Stewart R, Slukvin, II, Thomson JA. Induced pluripotent stem cell lines derived from human somatic cells. *Science.* 2007;318(5858):1917-1920.

47. Park IH, Zhao R, West JA, Yabuuchi A, Huo H, Ince TA, Lerou PH, Lensch MW, Daley GQ. Reprogramming of human somatic cells to pluripotency with defined factors. *Nature.* 2008;451(7175):141-146.

48. Shi Y, Desponts C, Do JT, Hahm HS, Scholer HR, Ding S. Induction of pluripotent stem cells from mouse embryonic fibroblasts by Oct4 and Klf4 with small-molecule compounds. *Cell Stem Cell.* 2008;3(5):568-574.

49. Narazaki G, Uosaki H, Teranishi M, Okita K, Kim B, Matsuoka S, Yamanaka S, Yamashita JK. Directed and systematic differentiation of

cardiovascular cells from mouse induced pluripotent stem cells. *Circulation.* 2008;118(5):498-506.

50. Kuzmenkin A, Liang H, Xu G, Pfannkuche K, Eichhorn H, Fatima A, Luo H, Saric T, Wernig M, Jaenisch R, Hescheler J. Functional characterization of cardiomyocytes derived from murine induced pluripotent stem cells in vitro. *FASEB J.* 2009;23(12):4168-4180.

51. Nelson TJ, Martinez-Fernandez A, Yamada S, Perez-Terzic C, Ikeda Y, Terzic A. Repair of acute myocardial infarction by human stemness factors induced pluripotent stem cells. *Circulation.* 2009;120(5):408-416.

52. Okita K, Nakagawa M, Hyenjong H, Ichisaka T, Yamanaka S. Generation of mouse induced pluripotent stem cells without viral vectors. *Science.* 2008;322(5903):949-953.

53. Stadtfeld M, Nagaya M, Utikal J, Weir G, Hochedlinger K. Induced pluripotent stem cells generated without viral integration. *Science.* 2008;322(5903):945-949.

54. Zhou H, Wu S, Joo JY, Zhu S, Han DW, Lin T, Trauger S, Bien G, Yao S, Zhu Y, Siuzdak G, Scholer HR, Duan L, Ding S. Generation of induced pluripotent stem cells using recombinant proteins. *Cell Stem Cell.* 2009;4(5):381-384.

55. Jia F, Wilson KD, Sun N, Gupta DM, Huang M, Li Z, Panetta NJ, Chen ZY, Robbins RC, Kay MA, Longaker MT, Wu JC. A nonviral minicircle vector for deriving human iPS cells. *Nat Methods.* 2010;7(3):197-199.

56. Judson RL, Babiarz JE, Venere M, Blelloch R. Embryonic stem cell-specific microRNAs promote induced pluripotency. *Nat Biotechnol.* 2009;27(5):459-461.

57. Nakamura Y, Wang X, Xu C, Asakura A, Yoshiyama M, From AH, Zhang J. Xenotransplantation of Long Term Cultured Swine Bone Marrow-Derived Mesenchymal Stem Cells. *Stem Cells.* 2006.

58. Wang X, Hu Q, Mansoor A, Lee J, Wang Z, Lee T, From AH, Zhang J. Bioenergetic and functional consequences of stem cell-based VEGF delivery in pressure-overloaded swine hearts. *Am J Physiol Heart Circ Physiol.* 2006;290(4):H1393-1405.

59. Wang X, Jameel MN, Li Q, Mansoor A, Qiang X, Swingen C, Panetta C, Zhang J. Stem cells for myocardial repair with use of a transarterial catheter. *Circulation.* 2009;120(11 Suppl):S238-246.

60. Zeng L, Hu Q, Wang X, Mansoor A, Lee J, Feygin J, Zhang G, Suntharalingam P, Boozer S, Mhashilkar A, Panetta CJ, Swingen C, Deans R, From AH, Bache RJ, Verfaillie CM, Zhang J. Bioenergetic and functional consequences of bone marrow-derived multipotent progenitor cell transplantation in hearts with postinfarction left ventricular remodeling. *Circulation.* 2007;115(14):1866-1875.

61. Dai W, Hale SL, Martin BJ, Kuang JQ, Dow JS, Wold LE, Kloner RA. Allogeneic mesenchymal stem cell transplantation in postinfarcted rat myocardium: short- and long-term effects. *Circulation.* 2005;112(2):214-223.

62. Wang X, Hu Q, Nakamura Y, Lee J, Zhang G, From AH, Zhang J. The Role of Sca-1+/CD31- Cardiac Progenitor Cell Population in Postinfarction LV Remodeling. *Stem Cells.* 2006.

63. Menasche P, Hagege AA, Vilquin JT, Desnos M, Abergel E, Pouzet B, Bel A, Sarateanu S, Scorsin M, Schwartz K, Bruneval P, Benbunan M, Marolleau JP, Duboc D. Autologous skeletal myoblast transplantation for severe postinfarction left ventricular dysfunction. *Journal of the American College of Cardiology.* 2003;41(7):1078-1083.

64. Pagani FD, DerSimonian H, Zawadzka A, Wetzel K, Edge AS, Jacoby DB, Dinsmore JH, Wright S, Aretz TH, Eisen HJ, Aaronson KD. Autologous skeletal myoblasts transplanted to ischemia-damaged myocardium in humans. Histological analysis of cell survival and differentiation. *Journal of the American College of Cardiology.* 2003;41(5):879-888.

65. Smits PC, van Geuns RJ, Poldermans D, Bountioukos M, Onderwater EE, Lee CH, Maat AP, Serruys PW. Catheter-based intramyocardial injection of autologous skeletal myoblasts as a primary treatment of ischemic heart failure: clinical experience with six-month follow-up. *Journal of the American College of Cardiology.* 2003;42(12):2063-2069.

66. Perin EC, Dohmann HF, Borojevic R, Silva SA, Sousa AL, Mesquita CT, Rossi MI, Carvalho AC, Dutra HS, Dohmann HJ, Silva GV, Belem L, Vivacqua R, Rangel FO, Esporcatte R, Geng YJ, Vaughn WK, Assad JA, Mesquita ET, Willerson JT. Transendocardial, autologous bone marrow cell transplantation for severe, chronic ischemic heart failure. *Circulation.* 2003;107(18):2294-2302.

67. Tse HF, Kwong YL, Chan JK, Lo G, Ho CL, Lau CP. Angiogenesis in ischaemic myocardium by intramyocardial autologous bone marrow mononuclear cell implantation. *Lancet.* 2003;361(9351):47-49.

68. Qiao H, Surti S, Choi SR, Raju K, Zhang H, Ponde DE, Kung HF, Karp J, Zhou R. Death and proliferation time course of stem cells transplanted in the myocardium. *Mol Imaging Biol.* 2009;11(6):408-414.

69. Assmus B, Schachinger V, Teupe C, Britten M, Lehmann R, Dobert N, Grunwald F, Aicher A, Urbich C, Martin H, Hoelzer D, Dimmeler S, Zeiher AM. Transplantation of Progenitor Cells and Regeneration Enhancement in Acute Myocardial Infarction (TOPCARE-AMI). *Circulation.* 2002;106(24):3009-3017.

70. Strauer BE, Brehm M, Zeus T, Kostering M, Hernandez A, Sorg RV, Kogler G, Wernet P. Repair of infarcted myocardium by autologous intracoronary mononuclear bone marrow cell transplantation in humans. *Circulation.* 2002;106(15):1913-1918.

71. Wang JS, Shum-Tim D, Chedrawy E, Chiu RC. The coronary delivery of marrow stromal cells for myocardial regeneration: pathophysiologic and therapeutic implications. *J Thorac Cardiovasc Surg.* 2001;122(4):699-705.

72. Wang T, Tang W, Sun S, Ristagno G, Huang Z, Weil MH. Intravenous infusion of bone marrow mesenchymal stem cells improves myocardial function in a rat model of myocardial ischemia. *Crit Care Med.* 2007;35(11):2587-2593.

73. Perin EC, Dohmann HFR, Borojevic R, Silva SA, Sousa ALS, Mesquita CT, Rossi MID, Carvalho AC, Dutra HS, Dohmann HJF, Silva GV, Belem L, Vivacqua R, Rangel FOD, Esporcatte R, Geng YJ, Vaughn WK, Assad JAR, Mesquita ET, Willerson JT. Transendocardial, autologous bone marrow cell transplantation for severe, chronic ischemic heart failure *Circulation.* 2003;107:2294-2302.

74. Strauer BE, Brehm M, Zeus T, Kostering M, Hernandez A, Sorg RV, Kogler G, Wernet P. Repair of infarcted myocardium by autologous intracoronary mononuclear bone marrow cell transplantation in humans. *Circulation.* 2002;106:1913-1918.

75. Gnecchi M, Zhang Z, Ni A, Dzau VJ. Paracrine mechanisms in adult stem cell signaling and therapy. *Circulation research.* 2008;103(11):1204-1219.

76. Zhang M, Methot D, Poppa V, Fujio Y, Walsh K, Murry CE. Cardiomyocyte grafting for cardiac repair: graft cell death and anti-death strategies. *Journal of molecular and cellular cardiology.* 2001;33(5):907-921.

77. Li TS, Hayashi M, Ito H, Furutani A, Murata T, Matsuzaki M, Hamano K. Regeneration of infarcted myocardium by intramyocardial implantation of ex vivo transforming growth factor-beta-preprogrammed bone marrow stem cells. *Circulation.* 2005;111(19):2438-2445.

78. Lim SY, Kim YS, Ahn Y, Jeong MH, Hong MH, Joo SY, Nam KI, Cho JG, Kang PM, Park JC. The effects of mesenchymal stem cells transduced with Akt in a porcine myocardial infarction model. *Cardiovascular research.* 2006;70(3):530-542.

79. Davis ME, Hsieh PC, Takahashi T, Song Q, Zhang S, Kamm RD, Grodzinsky AJ, Anversa P, Lee RT. Local myocardial insulin-like growth factor 1 (IGF-1) delivery with biotinylated peptide nanofibers improves cell therapy for myocardial infarction. *Proceedings of the National Academy of Sciences of the United States of America.* 2006;103(21):8155-8160.

80. Toh R, Kawashima S, Kawai M, Sakoda T, Ueyama T, Satomi-Kobayashi S, Hirayama S, Yokoyama M. Transplantation of cardiotrophin-1-expressing myoblasts to the left ventricular wall alleviates the transition from compensatory hypertrophy to congestive heart failure in Dahl salt-sensitive hypertensive rats. *Journal of the American College of Cardiology.* 2004;43(12):2337-2347.

81. Tang YL, Tang Y, Zhang YC, Qian K, Shen L, Phillips MI. Improved graft

mesenchymal stem cell survival in ischemic heart with a hypoxia-regulated heme oxygenase-1 vector. *Journal of the American College of Cardiology.* 2005;46(7):1339-1350.

82. Muraski JA, Rota M, Misao Y, Fransioli J, Cottage C, Gude N, Esposito G, Delucchi F, Arcarese M, Alvarez R, Siddiqi S, Emmanuel GN, Wu W, Fischer K, Martindale JJ, Glembotski CC, Leri A, Kajstura J, Magnuson N, Berns A, Beretta RM, Houser SR, Schaefer EM, Anversa P, Sussman MA. Pim-1 regulates cardiomyocyte survival downstream of Akt. *Nat Med.* 2007;13(12):1467-1475.

83. Borillo GA, Mason M, Quijada P, Volkers M, Cottage C, McGregor M, Din S, Fischer K, Gude N, Avitabile D, Barlow S, Alvarez R, Truffa S, Whittaker R, Glassy MS, Gustafsson AB, Miyamoto S, Glembotski CC, Gottlieb RA, Brown JH, Sussman MA. Pim-1 kinase protects mitochondrial integrity in cardiomyocytes. *Circulation research.*106(7):1265-1274.

84. Fischer KM, Cottage CT, Wu W, Din S, Gude NA, Avitabile D, Quijada P, Collins BL, Fransioli J, Sussman MA. Enhancement of myocardial regeneration through genetic engineering of cardiac progenitor cells expressing Pim-1 kinase. *Circulation.* 2009;120(21):2077-2087.

85. Askari A, Unzek S, Goldman CK, Ellis SG, Thomas JD, DiCorleto PE, Topol EJ, Penn MS. Cellular, but not direct, adenoviral delivery of vascular endothelial growth factor results in improved left ventricular function and neovascularization in dilated ischemic cardiomyopathy. *Journal of the American College of Cardiology.* 2004;43(10):1908-1914.

86. Yau TM, Kim C, Li G, Zhang Y, Weisel RD, Li RK. Maximizing ventricular function with multimodal cell-based gene therapy. *Circulation.* 2005;112(9 Suppl):I123-128.

87. Tillmanns J, Rota M, Hosoda T, Amano S, Rotatori F, LeCapitaine N, Siggins RW, Hintze T, Esposito G, De Angelis A, Loredo M, Misao Y, Bearzi C, Urbanek K, Leri A, Kajstura J, Sonnenblick EH, Anversa P. IGF-1 and HGF promote the engraftment of cardiac stem cells, which in turn regenerate the entire coronary vasculature and the dead myocardium after infarction in rats. *Circulation.* 2006;114:164-164.

88. Christman KL, Lee RJ. Biomaterials for the treatment of myocardial infarction. *Journal of the American College of Cardiology.* 2006;48(5):907-913.

89. Kass DA, Baughman KL, Pak PH, Cho PW, Levin HR, Gardner TJ, Halperin HR, Tsitlik JE, Acker MA. Reverse remodeling from cardiomyoplasty in human heart failure. External constraint versus active assist. *Circulation.* 1995;91(9):2314-2318.

90. Patel HJ, Polidori DJ, Pilla JJ, Plappert T, Kass D, St John Sutton M, Lankford EB, Acker MA. Stabilization of chronic remodeling by asynchronous cardiomyoplasty in dilated cardiomyopathy: effects of a conditioned muscle wrap. *Circulation.* 1997;96(10):3665-3671.

91. Carrier RL, Papadaki M, Rupnick M, Schoen FJ, Bursac N, Langer R, Freed LE, Vunjak-Novakovic G. Cardiac tissue engineering: cell seeding, cultivation parameters, and tissue construct characterization. *Biotechnol Bioeng.* 1999;64(5):580-589.

92. Carrier RL, Rupnick M, Langer R, Schoen FJ, Freed LE, Vunjak-Novakovic G. Perfusion improves tissue architecture of engineered cardiac muscle. *Tissue Eng.* 2002;8(2):175-188.

93. Radisic M, Euloth M, Yang L, Langer R, Freed LE, Vunjak-Novakovic G. High-density seeding of myocyte cells for cardiac tissue engineering. *Biotechnol Bioeng.* 2003;82(4):403-414.

94. Radisic M, Park H, Shing H, Consi T, Schoen FJ, Langer R, Freed LE, Vunjak-Novakovic G. Functional assembly of engineered myocardium by electrical stimulation of cardiac myocytes cultured on scaffolds. *Proceedings of the National Academy of Sciences of the United States of America.* 2004;101(52):18129-18134.

95. Miyahara Y, Nagaya N, Kataoka M, Yanagawa B, Tanaka K, Hao H, Ishino K, Ishida H, Shimizu T, Kangawa K, Sano S, Okano T, Kitamura S, Mori H. Monolayered mesenchymal stem cells repair scarred myocardium after myocardial infarction. *Nat Med.* 2006;12(4):459-465.

96. Davis ME, Hsieh PC, Grodzinsky AJ, Lee RT. Custom design of the cardiac microenvironment with biomaterials. *Circulation research.* 2005;97(1):8-15.

97. Kellar RS, Landeen LK, Shepherd BR, Naughton GK, Ratcliffe A, Williams SK. Scaffold-based three-dimensional human fibroblast culture provides a structural matrix that supports angiogenesis in infarcted heart tissue. *Circulation.* 2001;104(17):2063-2068.

98. Smythe GM, Grounds MD. Exposure to tissue culture conditions can adversely affect myoblast behavior in vivo in whole muscle grafts: implications for myoblast transfer therapy. *Cell Transplant.* 2000;9(3):379-393.

99. Smythe GM, Hodgetts SI, Grounds MD. Problems and solutions in myoblast transfer therapy. *J Cell Mol Med.* 2001;5(1):33-47.

100. Zhang G, Nakamura Y, Wang X, Hu Q, Suggs LJ, Zhang J. Controlled release of stromal cell-derived factor-1 alpha in situ increases c-kit+ cell homing to the infarcted heart. *Tissue Eng.* 2007;13(8):2063-2071.

101. de Graaf RA. In vivo NMR spectroscopy: principles and techniques (2nd edition). *John Wiley & Sons.* 2007.

102. Keevil SF. Spatial localization in nuclearmagnetic resonance spectroscopy. *Phys. Med. Biol.* 2006;51:R579-R636.

103. Ackerman JJH, Grove TH, Wong GH, Gadian DG, Radda GK. Mapping of metabolites in whole animals by ^{31}P NMR using surface coils. *Nature.*

1980;283:167-170.

104. Zhang J, Merkle H, Hendrich K, Garwood M, From AH, Ugurbil K, Bache RJ. Bioenergetic abnormalities associated with severe left ventricular hypertrophy. *The Journal of clinical investigation.* 1993;92(2):993-1003.

105. Zhang J, Wilke N, Wang Y, Zhang Y, Wang C, Eijgelshoven MH, Cho YK, Murakami Y, Ugurbil K, Bache RJ, From AH. Functional and bioenergetic consequences of postinfarction left ventricular remodeling in a new porcine model. MRI and 31 P-MRS study. *Circulation.* 1996;94(5):1089-1100.

106. Bendall MR, Gordon RE. Depth and refocusing pulses designed for multiphase NMR with surface coils. *J Magn Reson.* 1983;53:365-385.

107. Bendall MR, Pegg DT. Theoretical description of depth pulse sequences, on and off resonance, including improvements and extensions thereof. *Magn Reson Med.* 1985;2(91-113).

108. Hoult DI. Rotating frame zeugmatography. *J Magn Reson* 1979;33:183-187.

109. Garwood M, Schleich T, Ross BD, Matson GB, Winters WD. A modified rotating frame experiment based on a Fourier series window function. Application to in vivo spatially localized NMR spectroscopy. *J Magn Reson.* 1985;65:239-251.

110. Robitaille PM, Merkle H, Sublett E, Hendrich K, Lew B, Path G, From AHL, Bache RJ, Garwood M, Ugurbil K. Spectroscopic imaging and spatial localisation using adiabatic pulses and applications to detect transmural metabolite distributions in the canine heart. *Magn Reson Med.* 1989;10:14-37.

111. Hendrich K, Merkle H, Weisdorf S, Vine W, Garwood M, Ugurbil K. Phase-modulated rotating frame spectroscopic localization using an adiabatic plane-rotation pulse and single surface coil. *J Magn Reson.* 1991;92:258-275.

112. Hendrich K, Liu H, Merkle H, Zhang J, Ugurbil K. B1 voxel shifting of phase-modulated spectroscopic localization techniques. *J Magn Reson.* 1992;97:486-497.

113. Ordidge RJ, Connelly A, Lohman JAB. Image-selected in vivo spectroscopy (ISIS): a new technique for spatially selective NMR spectroscopy. *J Magn Reson.* 1986;66:283-294.

114. Bottomley PA. Spatial localization in NMR spectroscopy in vivo. *Ann N Y Acad Sci.* 1987;508(333-348).

115. Jung WI. Localized double spin echo proton spectroscopy. Part I: basic concepts. *Concepts Magn Reson.* 1996;8:1-17.

116. Frahm J, Merboldt KD, Hanicke W. Localized proton spectroscopy using stimulated echoes. *J Magn Reson.* 1987;72:502-508.

117. Granot J. Selected volume excitation using stimulated echoes (VEST). Application to spatially localized spectroscopy and imaging. *J Magn Reson.* 1986;70:486-492.

118. kimmich R, Hoepfel D. Volume-selective multipulse spin-echo spectroscopy. *J Magn Reson.* 1987;72:379-384.

119. Luyten PR, Marien AJ, Heindel W, van Gerwen PH, Herholz K, den Hollander JA, Friedmann G, Heiss WD. Metabolic imaging of patients with intracranial tumors: H-1 MR spectroscopic imaging and PET. *Radiology.* 1990;176(3):791-799.

120. Bessman SP, Carpenter CL. The creatine-creatine phosphate energy shuttle. *Annual review of biochemistry.* 1985;54:831-862.

121. Degani H, Laughlin M, Campbell S, Shulman RG. Kinetics of creatine kinase in heart: a 31P NMR saturation- and inversion-transfer study. *Biochemistry.* 1985;24(20):5510-5516.

122. Bittl JA, Ingwall JS. Reaction rates of creatine kinase and ATP synthesis in the isolated rat heart. A 31P NMR magnetization transfer study. *The Journal of biological chemistry.* 1985;260(6):3512-3517.

123. Ugurbil K, Petein M, Maidan R, Michurski S, From AH. Measurement of an individual rate constant in the presence of multiple exchanges: application to myocardial creatine kinase reaction. *Biochemistry.* 1986;25(1):100-107.

124. Kingsley-Hickman PB, Sako EY, Mohanakrishnan P, Robitaille PM, From AH, Foker JE, Ugurbil K. 31P NMR studies of ATP synthesis and hydrolysis kinetics in the intact myocardium. *Biochemistry.* 1987;26(23):7501-7510.

125. Wallimann T, Wyss M, Brdiczka D, Nicolay K, Eppenberger HM. Intracellular compartmentation, structure and function of creatine kinase isoenzymes in tissues with high and fluctuating energy demands: the 'phosphocreatine circuit' for cellular energy homeostasis. *Biochem J.* 1992;281 (Pt 1):21-40.

126. Wyss M, Smeitink J, Wevers RA, Wallimann T. Mitochondrial creatine kinase: a key enzyme of aerobic energy metabolism. *Biochimica et biophysica acta.* 1992;1102(2):119-166.

127. Wallimann T. Bioenergetics. Dissecting the role of creatine kinase. *Curr Biol.* 1994;4(1):42-46.

128. Zhang J. Myocardial energetics in cardiac hypertrophy. *Clin Exp Pharmacol Physiol.* 2002;29(4):351-359.

129. Ten Hove M, Neubauer S. MR spectroscopy in heart failure--clinical and experimental findings. *Heart Fail Rev.* 2007;12(1):48-57.

130. Beer M, Sandstede J, Landschutz W, Viehrig M, Harre K, Horn M, Meininger M, Pabst T, Kenn W, Haase A, von Kienlin M, Neubauer S, Hahn D. Altered energy metabolism after myocardial infarction assessed

by 31P-MR-spectroscopy in humans. *Eur Radiol.* 2000;10(8):1323-1328.

131. Beer M, Buchner S, Sandstede J, Viehrig M, Lipke C, Krug A, Kostler H, Pabst T, Kenn W, Landschutz W, von Kienlin M, Harre K, Neubauer S, Hahn D. ^{31}P-MR Spectroscopy for the evaluation of energy metabolism in intact residual myocardium after acute myocardial infarction in humans. *MAGMA.* 2001;13:70-75.

132. Neubauer S, Horn M, Cramer M, Harre K, Newell JB, Peters W, Pabst T, Ertl G, Hahn D, Ingwall JS, Kochsiek K. Myocardial phosphocreatine-to-ATP ratio is a predictor of mortality in patients with dilated cardiomyopathy. *Circulation.* 1997;96(7):2190-2196.

133. Spindler M, Saupe KW, Tian R, Ahmed S, Matlib MA, Ingwall JS. Altered creatine kinase enzyme kinetics in diabetic cardiomyopathy. A(31)P NMR magnetization transfer study of the intact beating rat heart. *Journal of molecular and cellular cardiology.* 1999;31(12):2175-2189.

134. Lamb HJ, Beyerbacht HP, van der Laarse A, Stoel BC, Doornbos J, van der Wall EE, de Roos A. Diastolic dysfunction in hypertensive heart disease is associated with altered myocardial metabolism. *Circulation.* 1999;99(17):2261-2267.

135. Conway MA, Bottomley PA, Ouwerkerk R, Radda GK, Rajagopalan B. Mitral regurgitation: impaired systolic function, eccentric hypertrophy, and increased severity are linked to lower phosphocreatine/ATP ratios in humans. *Circulation.* 1998;97(17):1716-1723.

136. Murakami Y, Zhang Y, Cho YK, Mansoor AM, Chung JK, Chu C, Francis G, Ugurbil K, Bache RJ, From AH, Jerosch-Herold M, Wilke N, Zhang J. Myocardial oxygenation during high work states in hearts with postinfarction remodeling. *Circulation.* 1999;99(7):942-948.

137. Murakami Y, Zhang J, Eijgelshoven MH, Chen W, Carlyle WC, Zhang Y, Gong G, Bache RJ. Myocardial creatine kinase kinetics in hearts with postinfarction left ventricular remodeling. *The American journal of physiology.* 1999;276(3 Pt 2):H892-900.

138. Kroll K, Kinzie DJ, Gustafson LA. Open-system kinetics of myocardial phosphoenergetics during coronary underperfusion. *The American journal of physiology.* 1997;272(6 Pt 2):H2563-2576.

139. Gustafson LA, Kroll K. Downregulation of 5'-nucleotidase in rabbit heart during coronary underperfusion. *The American journal of physiology.* 1998;274(2 Pt 2):H529-538.

140. Imai S, Riley AL, Berne RM. Effect of Ischemia on Adenine Nucleotides in Cardiac and Skeletal Muscle. *Circulation research.* 1964;15:443-450.

141. Tian R, Ingwall JS. Energetic basis for reduced contractile reserve in isolated rat hearts. *The American journal of physiology.* 1996;270(4 Pt 2):H1207-1216.

142. Smith CS, Bottomley PA, Schulman SP, Gerstenblith G, Weiss RG. Altered creatine kinase adenosine triphosphate kinetics in failing hypertrophied human myocardium. *Circulation.* 2006;114(11):1151-1158.

143. Nascimben L, Ingwall JS, Pauletto P, Friedrich J, Gwathmey JK, Saks V, Pessina AC, Allen PD. Creatine kinase system in failing and nonfailing human myocardium. *Circulation.* 1996;94(8):1894-1901.

144. De Sousa E, Veksler V, Minajeva A, Kaasik A, Mateo P, Mayoux E, Hoerter J, Bigard X, Serrurier B, Ventura-Clapier R. Subcellular creatine kinase alterations. Implications in heart failure. *Circulation research.* 1999;85(1):68-76.

145. Van Dorsten FA, Nederhoff MG, Nicolay K, Van Echteld CJ. 31P NMR studies of creatine kinase flux in M-creatine kinase-deficient mouse heart. *The American journal of physiology.* 1998;275(4 Pt 2):H1191-1199.

146. Saupe KW, Spindler M, Tian R, Ingwall JS. Impaired cardiac energetics in mice lacking muscle-specific isoenzymes of creatine kinase. *Circulation research.* 1998;82(8):898-907.

147. Spindler M, Meyer K, Stromer H, Leupold A, Boehm E, Wagner H, Neubauer S. Creatine kinase-deficient hearts exhibit increased susceptibility to ischemia-reperfusion injury and impaired calcium homeostasis. *Am J Physiol Heart Circ Physiol.* 2004;287(3):H1039-1045.

148. Nahrendorf M, Spindler M, Hu K, Bauer L, Ritter O, Nordbeck P, Quaschning T, Hiller KH, Wallis J, Ertl G, Bauer WR, Neubauer S. Creatine kinase knockout mice show left ventricular hypertrophy and dilatation, but unaltered remodeling post-myocardial infarction. *Cardiovascular research.* 2005;65(2):419-427.

149. Neubauer S, Hu K, Horn M, Remkes H, Hoffmann KD, Schmidt C, Schmidt TJ, Schnackerz K, Ertl G. Functional and energetic consequences of chronic myocardial creatine depletion by beta-guanidinopropionate in perfused hearts and in intact rats. *Journal of molecular and cellular cardiology.* 1999;31(10):1845-1855.

150. Horn M, Remkes H, Stromer H, Dienesch C, Neubauer S. Chronic phosphocreatine depletion by the creatine analogue beta-guanidinopropionate is associated with increased mortality and loss of ATP in rats after myocardial infarction. *Circulation.* 2001;104(15):1844-1849.

151. van Deursen J, Heerschap A, Oerlemans F, Ruitenbeek W, Jap P, ter Laak H, Wieringa B. Skeletal muscles of mice deficient in muscle creatine kinase lack burst activity. *Cell.* 1993;74(4):621-631.

152. Liu J, Wang C, Murakami Y, Gong G, Ishibashi Y, Prody C, Ochiai K, Bache RJ, Godinot C, Zhang J. Mitochondrial ATPase and high-energy phosphates in failing hearts. *Am J Physiol Heart Circ Physiol.* 2001;281(3):H1319-1326.

153. Bolognese L, Neskovic AN, Parodi G, Cerisano G, Buonamici P, Santoro GM, Antoniucci D. Left ventricular remodeling after primary coronary angioplasty: patterns of left ventricular dilation and long-term prognostic implications. *Circulation.* 2002;106(18):2351-2357.

154. Hu Q, Wang X, Lee J, Mansoor A, Liu J, Zeng L, Swingen C, Zhang G, Feygin J, Ochiai K, Bransford TL, From AH, Bache RJ, Zhang J. Profound bioenergetic abnormalities in peri-infarct myocardial regions. *Am J Physiol Heart Circ Physiol.* 2006;291(2):H648-657.

155. Assmus B, Honold J, Schachinger V, Britten MB, Fischer-Rasokat U, Lehmann R, Teupe C, Pistorius K, Martin H, Abolmaali ND, Tonn T, Dimmeler S, Zeiher AM. Transcoronary transplantation of progenitor cells after myocardial infarction. *N Engl J Med.* 2006;355(12):1222-1232.

156. Zhang G, Hu Q, Braunlin EA, Suggs LJ, Zhang J. Enhancing efficacy of stem cell transplantation to the heart with a PEGylated fibrin biomatrix. *Tissue Eng Part A.* 2008;14(6):1025-1036.

157. Zhang G, Wang X, Wang Z, Zhang J, Suggs L. A PEGylated fibrin patch for mesenchymal stem cell delivery. *Tissue Eng.* 2006;12(1):9-19.

158. Hill KL, Obrtlikova P, Alvarez DF, King JA, Keirstead SA, Allred JR, Kaufman DS. Human embryonic stem cell-derived vascular progenitor cells capable of endothelial and smooth muscle cell function. *Exp Hematol.* 2010;38(3):246-257 e241.

159. Wilber A, Linehan JL, Tian X, Woll PS, Morris JK, Belur LR, McIvor RS, Kaufman DS. Efficient and stable transgene expression in human embryonic stem cells using transposon-mediated gene transfer. *Stem Cells.* 2007;25(11):2919-2927.

160. Tolar J, Wang X, Braunlin E, McElmurry RT, Nakamura Y, Bell S, Xia L, Zhang J, Hu Q, Panoskaltsis-Mortari A, Blazar BR. The host immune response is essential for the beneficial effect of adult stem cells after myocardial ischemia. *Exp Hematol.* 2007;35(4):682-690.

161. Tolar J, Wang X, Braunlin E, McElmurry RT, Nakamura Y, Bell S, Xia L, Zhang J, Hu Q, Panoskaltsis-Mortari A, Zhang J, Blazar BR. The host immune response is essential for the beneficial effect of adult stem cells after myocardial ischemia. *Exp Hematol.* 2007;35(4):682-690.

162. Dubey N, Letourneau PC, Tranquillo RT. Neuronal contact guidance in magnetically aligned fibrin gels: effect of variation in gel mechano-structural properties. *Biomaterials.* 2001;22(10):1065-1075.

163. Grassl ED, Oegema TR, Tranquillo RT. Fibrin as an alternative biopolymer to type-I collagen for the fabrication of a media equivalent. *J Biomed Mater Res.* 2002;60(4):607-612.

164. Rosner B, Willett WC, Spiegelman D. Correction of logistic regression relative risk estimates and confidence intervals for systematic within-person measurement error. *Stat Med.* 1989;8(9):1051-1069; discussion

1071-1053.

165. Woll PS, Morris JK, Painschab MS, Marcus RK, Kohn AD, Biechele TL, Moon RT, Kaufman DS. Wnt signaling promotes hematoendothelial cell development from human embryonic stem cells. *Blood.* 2008;111(1):122-131.

166. Kehat I, Khimovich L, Caspi O, Gepstein A, Shofti R, Arbel G, Huber I, Satin J, Itskovitz-Eldor J, Gepstein L. Electromechanical integration of cardiomyocytes derived from human embryonic stem cells. *Nat Biotechnol.* 2004;22(10):1282-1289.

167. Feygin J, Hu Q, Swingen C, Zhang J. Relationships between regional myocardial wall stress and bioenergetics in hearts with left ventricular hypertrophy. *Am J Physiol Heart Circ Physiol.* 2008;294(5):H2313-2321.

168. Trachtenberg BH, Hare JM. Biomarkers of oxidative stress in heart failure. *Heart Fail Clin.* 2009;5(4):561-577.

169. Amado LC, Saliaris AP, Schuleri KH, St John M, Xie JS, Cattaneo S, Durand DJ, Fitton T, Kuang JQ, Stewart G, Lehrke S, Baumgartner WW, Martin BJ, Heldman AW, Hare JM. Cardiac repair with intramyocardial injection of allogeneic mesenchymal stem cells after myocardial infarction. *Proceedings of the National Academy of Sciences of the United States of America.* 2005;102(32):11474-11479.

170. Gnecchi M, He H, Noiseux N, Liang OD, Zhang L, Morello F, Mu H, Melo LG, Pratt RE, Ingwall JS, Dzau VJ. Evidence supporting paracrine hypothesis for Akt-modified mesenchymal stem cell-mediated cardiac protection and functional improvement. *FASEB J.* 2006;20(6):661-669.

171. Jameel MN, Li Q, Mansoor A, Qiang X, Sarver A, Wang X, Swingen C, Zhang J. Long term functional improvement and gene expression changes after bone marrow derived multipotent progenitor cell transplantation in myocardial infarction. *Am J Physiol Heart Circ Physiol.* 2010.

172. Black BL, Olson EN. Transcriptional control of muscle development by myocyte enhancer factor-2 (MEF2) proteins. *Annu Rev Cell Dev Biol.* 1998;14:167-196.

173. Tang XL, Rokosh G, Sanganalmath SK, Yuan F, Sato H, Mu J, Dai S, Li C, Chen N, Peng Y, Dawn B, Hunt G, Leri A, Kajstura J, Tiwari S, Shirk G, Anversa P, Bolli R. Intracoronary administration of cardiac progenitor cells alleviates left ventricular dysfunction in rats with a 30-day-old infarction. *Circulation.*121(2):293-305.

174. Ingwall JS, Weiss RG. Is the failing heart energy starved? On using chemical energy to support cardiac function. *Circulation research.* 2004;95(2):135-145.

175. Katz AM. Is the failing heart energy depleted? *Cardiology clinics.* 1998;16(4):633-644, viii.

176. Ingwall JS, Kramer MF, Fifer MA, Lorell BH, Shemin R, Grossman W, Allen PD. The creatine kinase system in normal and diseased human myocardium. *The New England journal of medicine.* 1985;313(17):1050-1054.

177. Ventura-Clapier R, Saks VA, Vassort G, Lauer C, Elizarova GV. Reversible MM-creatine kinase binding to cardiac myofibrils. *The American journal of physiology.* 1987;253(3 Pt 1):C444-455.

178. Murakami Y, Zhang JY, Eijgelshoven MHJ, Chen W, Carlyle WC, Zhang Y, Gong GR, Bache RJ. Myocardial creatine kinase kinetics in hearts with postinfarction left ventricular remodeling. *Am. J. Physiol. Heart Circ. Physiol.* 1999;276:H892-H900.

179. Ye Y, Gong GR, Ochiai K, Liu JB, Zhang JY. High-energy phosphate metabolism and creatine kinase in failing hearts : a new porcine model. *Circulation.* 2001;103:1570-1576.

180. Ye Y, Wang CS, Zhang JY, Cho YK, Gong GR, Murakami M, Bache RJ. Myocardial creatine kinase kinetics and isoform expression in hearts with severe LV hypertrophy. *Am. J. Physiol. Heart Circ. Physiol.* 2001;281:H376-H386.

181. Zhang JY. Myocardial energetics in cardiac hypertrophy. *Clin. Exp. Pharmacol. Physiol.* 2002;29:351-359.

182. Smith CS, Bottomley PA, Schulman SP, Gerstenblith G, Weiss RG. Altered creatine kinase adenosine triphosphate kinetics in failing hypertrophied human myocardium. *Circulation.* 2006;114:1151-1158.

183. Weiss RG, Gerstenblith G, Bottomley PA. ATP flux through creatine kinase in the normal, stressed, and failing human heart. *Proceedings of the National Academy of Sciences of the United States of America.* 2005;102(3):808-813.

184. Robitaille PM, Abduljalil A, Rath D, Zhang H, Hamlin RL. Transmural saturation transfer analysis of the creatine kinase system in the mammalian heart. *Magn Reson Med.* 1993;30(1):4-10.

185. Zhang JY, Merkle H, Hendrich K, Garwood M, From AHL, Ugurbil K, RJ. B. Bioenergetic abnormalities associated with severe left-ventricular hypertrophy. *J. Clin. Invest.* 1993;92:993-1003.

186. Liu H, Zhang J. An efficient MR phosphorous spectroscopic localization technique for studying ischemic heart. *J Magn Reson Imaging.* 1999;10(5):892-898.

187. Lei H, Ugurbil K, Chen W. Measurement of unidirectional Pi to ATP flux in human visual cortex at 7 T by using in vivo ^{31}P magnetic resonance spectroscopy. *Proc. Natl. Acad. Sci. USA.* 2003;100:14409-14414.

188. Bittl JA, Ingwall JS. Reaction rates of creatine kinase and ATP synthesis in the isolated rat heart. *J. Biol. Chem.* 1985;260:3512-3517.

189. Saupe KW, Spindler M, Hopkins JCA, Shen WQ, Ingwall JS. Kinetic, thermodynamic, and developmental consequences of deleting creatine kinase isoenzymes from the heart. *J. Biol. Chem.* 2000;275:19742-19746.

190. Bittl JA, Balschi JA, Ingwall JS. Effects of norepinephrine infusion on myocardial high-energy phosphate content and turnover in the living rat. *J. Clin. Invest.* 1987;79:1852-1859.

191. Friedrich J, Nascimben L, Liao R, Ingwall JS. Phosphocreatine TI measurements with and without exchange in the heart. *Magn. Reson. Med.* 1993;30:45-50.

192. Horska A, Horsky Jiri, Spencer RGS. Measurement of spin-lattice relaxation times in systems undergoing chemical exchange. *J. Magn. Reson.* 1994;110:82-89.

193. Spencer RGS, Fishbein KW. Measurement of spin-lattice relaxation times and concentrations in systems with chemical exchange using the one-pulse sequence: Breakdown of the Ernst model for partial saturation in nuclear magnetic resonance spectroscopy. *J. Magn. Reson.* 2000;142:120-135.

194. Bloch F. Nuclear Induction. *Phys. Rev.* 1946;70:460-474.

195. McConnell HM. Reaction Rates by Nuclear Magnetic Resonance. *J. Chem. Phys.* 1958;28:430-431.

196. Degani H, Laughlin M, Campbell S, Shulman R. Kinetics of creatine kinase in heart: a 31P NMR saturation- and inversion- transfer study. *Biochemistry.* 1985;24:5510-5516.

197. Ugurbil K, Petein M, Maidan R, Mishurshi S, From AHL. Measurement of an individual rate constant in the presence of multiple exchanges: application to myocardial creatine kinase reaction. *Biochemistry.* 1986;25:100-107.

198. Zhang JY, Wilke N, Wang Y, Zhang Y, Wang CS, Eijgelshoven MHJ, Cho YK, Murakami Y, Ugurbil K, Bache RJ, AHL F. Functional and bioenergetic consequences of postinfarction left ventricular remodeling in a new porcine model - MRI and P-31-MRS study. *Circulation.* 1996;94:1089-1100.

199. Dobson GP, Veech RL, Passonneau JV, Kobayashi K, Inubushi T, Wehrli S, Nioka S, Chance B. 31P NMR and enzymatic analysis of cytosolic phosphocreatine, ATP, Pi and intracellular pH in the isolated working perfused rat heart. *NMR Biomed.* 1992;5(1):20-28.

200. Goudemant JF, vander Elst L, Dupont B, Van Haverbeke Y, Muller RN. pH and temperature effects on kinetics of creatine kinase in aqueous solution and in isovolumic perfused heart. A 31P nuclear magnetization transfer study. *NMR Biomed.* 1994;7(3):101-110.

201. Horska A, Horsky J, Spencer RG. Measurement of spin-lattice relaxation

times in systems undergoing chemical exchange. *J Magn Reson.* 1994;110:82-89.

202. Du F, Zhu XH, Zhang Y, Friedman M, Zhang NY, Ugurbil K, Chen W. Tightly coupled brain activity and cerebral ATP metabolic rate. *Proc. Natl. Acad. Sci. USA.* 2007;105:6409-6414.

203. Bottomley PA, Ouwerkerk R, Lee RF, Weiss RG. Four-angle saturation transfer (FAST) method for measuring creatine kinase reaction rates in vivo. *Magn Reson Med.* 2002;47(5):850-863.

204. Ugurbil K. Magnetization-transfer measurements of individual rate constants in the presence of multiple reactions. *J Magn Reson.* 1985;64:207-219.

205. Ye Y, Wang C, Zhang J, Cho YK, Gong G, Murakami Y, Bache RJ. Myocardial creatine kinase kinetics and isoform expression in hearts with severe LV hypertrophy. *Am J Physiol Heart Circ Physiol.* 2001;281(1):H376-386.

206. Du F, Zhu XH, Zhang Y, Friedman M, Zhang N, Ugurbil K, Chen W. Tightly coupled brain activity and cerebral ATP metabolic rate. *Proceedings of the National Academy of Sciences of the United States of America.* 2008;105(17):6409-6414.

207. Chen W, Zhu XH, Adriany G, Ugurbil K. Increase of creatine kinase activity in the visual cortex of human brain during visual stimulation: a 31P magnetization transfer study. *Magn Reson Med.* 1997;38(4):551-557.

208. Xiong Q, Li Q, Mansoor A, Jameel MN, Du F, Chen W, Zhang J. Novel strategy for measuring creatine kinase reaction rate in the in vivo heart. *Am J Physiol Heart Circ Physiol.* 2009;297(3):H1010-1019.

209. Bloch F. Nuclear Induction. *Phys Rev.* 1946;70:460-474.

210. McConnell HM. Reaction rates by nuclear magnetic resonance. *J Chem Phys.* 1958;28(3):430-431.

211. Du F, Zhu XH, Qiao H, Zhang X, Chen W. Efficient in vivo 31P magnetization transfer approach for noninvasively determining multiple kinetic parameters and metabolic fluxes of ATP metabolism in the human brain. *Magn Reson Med.* 2007;57(1):103-114.

212. Bittl JA, Balschi JA, Ingwall JS. Effects of norepinephrine infusion on myocardial high-energy phosphate content and turnover in the living rat. *The Journal of clinical investigation.* 1987;79(6):1852-1859.

213. Lei H, Ugurbil K, Chen W. Measurement of unidirectional Pi to ATP flux in human visual cortex at 7 T by using in vivo 31P magnetic resonance spectroscopy. *Proceedings of the National Academy of Sciences of the United States of America.* 2003;100(24):14409-14414.

214. Friedrich J, Nascimben L, Liao R, Ingwall JS. Phosphocreatine T1 measurements with and without exchange in the heart. *Magn Reson Med.*

1993;30:45-50.

215. Bottomley PA, Ouwerkerk R. Optimum flip-angles for exciting NMR with uncertain T1 values. *Magn Reson Med.* 1994;32(1):137-141.

216. Garwood M, Ke Y. Symmetric pulses to induce arbitrary flip angles with compensation for RF inhomogeneity and resonance offsets. *J Magn Reson.* 1991;94:511-525.

217. de Graaf RA, Luo Y, Garwood M, Nicolay K. B1-insensitive, single-shot localization and water suppression. *J Magn Reson B.* 1996;113(1):35-45.

218. Garwood M, Schleich T, Ross BD, Matson GB, WintersWD. A modified rotating frame experiment based on a Fourier series window function: application to in vivo spatially localised NMR spectroscopy. *J. Magn. Reson.* 1985;65:239-251.

219. de Graaf RA, Luo Y, Garwood M, Nicolay K. B1-insensitive, single -shot localization and water suppression. *J. Magn. Reson.* 1996;113:35-45.

220. Zhang J, Duncker DJ, Xu Y, Zhang Y, Path G, Merkle H, Hendrich K, From AH, Bache RJ, Ugurbil K. Transmural bioenergetic responses of normal myocardium to high workstates. *The American journal of physiology.* 1995;268(5 Pt 2):H1891-1905.

221. Zhang J, Toher C, Erhard M, Zhang Y, Ugurbil K, Bache RJ, Lange T, Homans DC. Relationships between myocardial bioenergetic and left ventricular function in hearts with volume-overload hypertrophy. *Circulation.* 1997;96(1):334-343.

222. Ye Y, Gong G, Ochiai K, Liu J, Zhang J. High-energy phosphate metabolism and creatine kinase in failing hearts: a new porcine model. *Circulation.* 2001;103(11):1570-1576.